CO_2 conditioning: process optimisation, thermodynamic modelling, and measurement of impurities

Dlamini, Gcinisizwe Msimisi

Publication date:
2024

Document Version
Publisher's PDF, also known as Version of record

CO_2 conditioning: process optimisation, thermodynamic modelling, and measurement of impurities

Gcinisizwe Msimisi Dlamini

PhD Thesis

Center for Energy Resources Engineering

Department of Chemical & Biochemical Engineering

Technical University of Denmark

April, 2024

Preface

This PhD thesis, entitled "CO_2 conditioning: process optimisation, thermodynamic modelling, and measurement of impurities", is prepared in partial fulfilment of the requirements for the PhD degree at the Technical University of Denmark, DTU. The work was conducted at the Center for Energy Resources Engineering, CERE at the Department of Chemical and Biochemical Engineering under the supervision of Prof. Nicolas von Solms and Assoc. Prof. Philip Loldrup Fosbøl. Part of the work was conducted in the Thermophysics Laboratory in the Department of Chemical Engineering, Imperial College London. The PhD commenced in May 2021 and ended in April 2024.

This work received financial support from the European Union's Horizon 2020 research and innovation programme (Grant Agreement No 838031) as part of the 3D Project (DMX™ Demonstration in Dunkirk) and DTU Chemical Engineering. The Otto Mønsteds Fond has financially supported this work by providing a travel grant for an external research stay.

Acknowledgements

My journey began at my alma mater when I met Nicolas von Solms. At that time I was perhaps set with frustration from challenging lab experiments, but upon meeting Nicolas a sense of calm engulfed me. I am grateful to Nicolas for nurturing my curiosity and for granting me space to think my ideas through. I also extend my thanks to Philip Loldrup Fosbøl for the support, and for the wonderful work you do to ensure our success.

I extend my many thanks to Martin Trusler, who has guided me through my research stay at Imperial College. From Martin, I have learnt the art of scaling fundamental science to a functional apparatus. In this journey, I have been honoured to be also guided by Carsten Wedler, who has been an incredible sounding board. In my many attempts to find the right spanner for my experimental setup, I made lifelong friends in London, for whom I am grateful for: thanks David, Iusiph, Riley, Qiaoyun, Yasser, Keming, and Hossam for helping me find the right Sitec fittings.

My colleagues at CERE have been foundational in making this journey one filled with fond memories and amazing thermodynamic discussions. Thank you to my former office mate, Saman, my colleagues Julia, James, Hillary, Randi, Olivia, Andre, Javad, Wentao, Mary, Lucas, and Sai. I also extend my thanks to Louise, Christian, and Patricia who have brought so much cheer to the group, and have truly cared about our experience in the department.

In the African culture, there is a saying that it 'takes a village to raise a child'. That is indeed true for me. Aunty Nokuthula, you were the catalyst that made my dreams a reality, where I could most likely be rearing cattle. My father, Bernard Dlamini, you have sown a seed in me to pursue education and always stay curious, thank you. To my mother, Nonhlanhla, thank you for being a constant in my life, and for always showing up in incredible ways. I appreciate my siblings, Tenkhosi and Lungelo who have always encouraged and emotionally supported me throughout this journey. Numerous individuals have been part of my village to mention here, I thank you.

To my wife, Lindelwa Sambo, you committed to 'counting stones' with me, even when it did not make sense. You have been my rock, my fellow debater. You have listened to my unorthodox ideas, hugged me, and helped me make sense of my work (you could probably write a thesis on this subject, as well). Thank you sithandwa sami.

To God, it is for your Glory!

Abstract

The carbon capture utilisation and storage (CCUS) value chain has been identified as a key pathway for mitigating anthropogenic CO_2 emissions, especially for hard-to-abate sectors. This thesis focuses on a key segment of the CCUS value chain - CO_2 conditioning - which is the interface between CO_2 capture and transport. The conditioning process ensures that compositional and pressure specifications of transportation, utilisation and storage facilities are met. The objectives of this study are to optimise the conditioning process, improve the thermodynamic modelling of common impurities in the CCUS value chain, and finally develop techniques towards the real-time monitoring of impurities in CO_2-rich streams.

To maximise economies of scale, the CCUS value chain requires the sharing of infrastructure, such as a network of transportation pipelines linking multiple CO_2 point sources and sinks. However, the development of this infrastructure faces multiple uncertainties, due to the nascency of the large-scale deployment of CCUS. These uncertainties include the number of future pipeline users, the amount of CO_2 to be transported and the capacity of CO_2 storage sinks. Therefore, in optimising the CO_2 conditioning process to minimise energy consumption and capital requirement, process flexibility was also evaluated, considering the uncertainty in pipeline flowrate. Different permutations of conventional multistage compression, and subcritical liquefaction and pumping of CO_2 process schemes were considered. The outcome of this investigation provides a basis for the integrated design of CO_2 conditioning processes and the sizing of shared CO_2 pipelines. Upon considering various process parameters, this work reveals that using low-temperature cooling water is the most critical variable to enable the least energy-intensive and flexible CO_2 conditioning processes.

Impurities pose significant challenges to the CCUS value chain. They can influence the phase equilibria and thermophysical properties of CO_2. Therefore, accurate thermodynamic models are required to model and design various elements of the CCUS value chain. This thesis further presents an improvement in the thermodynamic modelling of a key class of common impurities in the CCUS value chain – sulphur-containing compounds (SO_2, H_2S, COS). This class of impurities often has a strict specification at CO_2 storage facilities. By considering these compounds as self-associating, this work provides a successful predictive approach using the Cubic Plus Association equation of state, to model the phase equilibria of sulphur

compounds in mixtures relevant to CCUS. The predictive approach is validated against experimental data for mixtures of these sulphur-containing compounds with CO_2, and with other common impurities such as CH_4, and glycols.

Furthermore, this thesis sheds light on how impurities can be monitored in the CCUS value chain. An experimental investigation is conducted involving the use of in-situ Raman spectroscopy to measure the water content of CO_2, and those of N_2 and H_2, which are common CCUS impurities. The experimental investigation is performed at pressures ranging from 5 to 15 MPa. This work highlights and demonstrates the inherent constraints of conventional quantitative methods of Raman spectroscopy for the determination of gas water content. Thus, in this thesis, a novel approach which uses water-only Raman spectra features for gas water content determination is proposed. This proposed method is validated at a wide range of pressure and temperature conditions, water content levels, and different binary systems. The developed approach allows for the generation of a new set of experimental data describing the phase equilibria of the investigated gases with water. Immediate applications of the proposed quantitative approach would be in the monitoring of gas dehydration processes.

Resumé på Dansk

Værdikæden for udnyttelse og lagring af kulstoffangst (CCUS) er blevet identificeret som en hoved falefor forlevej at mindske menneskeskabte CO_2-udledninger, især for sektorer, der er svære at reducere. Denne PhD afhandling fokuserer på et nøglesegment af CCUS værdikæden - CO_2-konditionering - som er grænsefladen mellem CO_2-opsamling og transport. Konditioneringsprocessen sikrer, at sammensætning og trykspecifikationer for transport, udnyttelse og lagerfaciliteter overholdes. Formålet med denne undersøgelse er at optimere konditioneringsprocessen, forbedre den termodynamiske modellering af almindelige urenheder i CCUS-værdikæden og endelig udvikle teknikker til realtidsovervågning af urenheder i CO_2-rige strømme.

For at maksimere stordriftsfordele kræver CCUS-værdikæden deling af infrastruktur, såsom et netværk af transportrørledninger, der forbinder flere CO_2-punktkilder og dræn. Udviklingen af denne infrastruktur står imidlertid over for flere usikkerhedsmomenter på grund af den tidligere udbredelse af CCUS i stor skala. Disse usikkerheder omfatter antallet af fremtidige rørledningsbrugere, mængden af CO_2, der skal transporteres, og kapaciteten af CO_2-lagerdræn. Ved optimering af CO_2-konditioneringsprocessen for at minimere energiforbruget og kapitalbehovet blev procesfleksibiliteten derfor også evalueret under hensyntagen til usikkerheden i rørledningens flowhastighed. Forskellige permutationer af konventionel kompression og subkritisk fortætning og pumpning af CO_2-processkemaer blev overvejet. Resultatet af denne undersøgelse danner grundlag for det integrerede design af CO_2-konditioneringsprocesser og dimensionering af fælles CO_2-rørledninger. Efter at have overvejet forskellige procesparametre afslører dette arbejde, at brug af lavtemperaturkølevand er den mest kritiske variabel for at muliggøre de mindst energikrævende og fleksible CO_2-konditioneringsprocesser.

Urenheder udgør betydelige udfordringer for CCUS værdikæden. De kan påvirke CO_2's faseligevægte og termofysiske egenskaber. Derfor kræves der nøjagtige termodynamiske modeller for at beregne og designe forskellige elementer i CCUS værdikæden. Denne afhandling præsenterer yderligere en forbedring i den termodynamiske modellering af en nøgleklasse af almindelige urenheder i CCUS værdikæden - svovlholdige forbindelser (SO_2, H_2S, COS). Denne klasse af urenheder har ofte en streng specifikation på CO_2-lagerfaciliteter. Ved at betragte disse forbindelser som selvassocierende, giver dette arbejde en succesfuld forudsigelig

tilgang ved hjælp af Cubic Plus Association-tilstandsligningen til at modellere faseligevægtene for svovlforbindelser i blandinger, der er relevante for CCUS. Den prædiktive tilgang er valideret mod eksperimentelle data for blandinger af disse svovlholdige forbindelser med CO_2 og med andre almindelige urenheder såsom CH_4 og glykoler.

Endvidere belyser denne afhandling, hvordan urenheder kan overvåges i CCUS værdikæden. Der udføres en eksperimentel undersøgelse, der involverer brugen af in-situ Raman-spektroskopi til at måle vandindholdet af CO_2 og indholdet af N2 og H_2, som er almindelige CCUS-urenheder. Den eksperimentelle undersøgelse udføres ved tryk i området fra 5 til 15 MPa. Dette arbejde fremhæver og demonstrerer de iboende begrænsninger af konventionelle kvantitative metoder til Raman-spektroskopi til bestemmelse af gasvandindhold. Derfor foreslås i denne afhandling en ny tilgang, som anvender kun vand-raman-spektrefunktioner til bestemmelse af gasvandindhold. Denne foreslåede metode er valideret ved en lang række tryk- og temperaturforhold, vandindholdsniveauer og forskellige binære systemer. Den udviklede tilgang giver mulighed for generering af et nyt sæt eksperimentelle data, der beskriver faseligevægtene for de undersøgte gasser med vand. Umiddelbare anvendelser af den foreslåede kvantitative tilgang vil være i overvågningen af gasdehydreringsprocesser.

List of publications and conference contributions

List of peer-reviewed articles that form part of the thesis:

Gcinisizwe Msimisi Dlamini, Eryk Remiezowicz, Kenneth Ness, Erik-Losnergård, Philip Loldrup Fosbøl, Nicolas von Solms, Optimisation of carbon dioxide pressurisation pathways for pipeline offshore delivery. International Journal of Greenhouse Gas Control, 128, 2023, doi.org/10.1016/j.ijggc.2023.103943.

Gcinisizwe Msimisi Dlamini, Philip Loldrup Fosbøl, Nicolas von Solms, Modelling phase equilibria of sulphur compounds in mixtures relevant to carbon capture and storage with new association schemes, Fluid Phase Equilibria, 568, 2023, doi.org/10.1016/j.fluid.2023.113738.

Gcinisizwe Msimisi Dlamini, Carsten Wedler, Philip Loldrup Fosbøl, Nicolas von Solms, Martin Trusler, Water Content measurements in compressed fluids (CO_2, N_2, H_2) using in-situ Raman spectroscopy. Submitted to Journal of Raman Spectroscopy.

Peer-review article that does not form part of the thesis:

Ebbe Hauge Jensen, Rikke Cillius Pedersen, Isaac Appelquist Løge, Søren Jensen, **Gcinisizwe Msimisi Dlamini**, Randi Neerup, Christian Riber, Brian Elmegaard, Jonas Kjær Jensen, Philip Loldrup Fosbøl, The cost of impurities: A techno-economic assessment of conditioning in captured CO_2 to commercial specifications. Submitted to Journal of Greenhouse Gas Control.

Conference contributions:

Gcinisizwe Msimisi Dlamini, Eryk Remiezowicz, Kenneth Ness, Erik-Losnergård, Philip Loldrup Fosbøl, Wentao Gong, Nicolas von Solms, Carbon dioxide conditioning pathways for pipeline transport, Proceedings of the 16th Greenhouse Gas Control Technologies Conference (GHGT-16), 2022.

Gcinisizwe Msimisi Dlamini, Philip Loldrup Fosbøl, Nicolas von Solms, Modelling phase equilibria of sulphur compounds with the Cubic Plus Association equation of state, PPEPPD, 2023.

Gcinisizwe Msimisi Dlamini, Eryk Remiezowicz, Kenneth Ness, Erik-Losnergård, Philip Loldrup Fosbøl, Nicolas von Solms, Comprehensive optimisation and sensitivity analysis of carbon dioxide conditioning pathways for offshore pipeline delivery, TCCS, 2023.

Wentao Gong, Philip Loldrup Fosbøl, Nicolas von Solms**, Gcinisizwe Msimisi Dlamini**, Techno-economic analysis of novel CO_2 liquefaction processes, Proceedings of the 16th Greenhouse Gas Control Technologies Conference (GHGT-16), 2022.

Table of Contents

List of Figures

List of Tables

1 Introduction

1.1 Motivation

There is unequivocal evidence that the rise of greenhouse gas (GHG) emissions that has progressed from the industrial age has led to a direct shift in the earth's climate [1]. In particular, anthropogenic CO_2 emissions have been identified as the main driver of climate change [1,2]. CO_2 emissions have grown rapidly since the turn of the industrial revolution and have recently reached 36.95 Gt in 2019, a 36% rise since 1990 [3].

The direct sources of CO_2 emissions are mainly from the combustion of fossil fuels to obtain energy primarily for use in residential and commercial heating, and the production of electricity, as presented in Figure 1.1. CO_2 emissions from industries, which account for 27.2% of all anthropogenic emissions, are primarily from the production of metals (such as iron & steel), cement, and the chemicals industry.

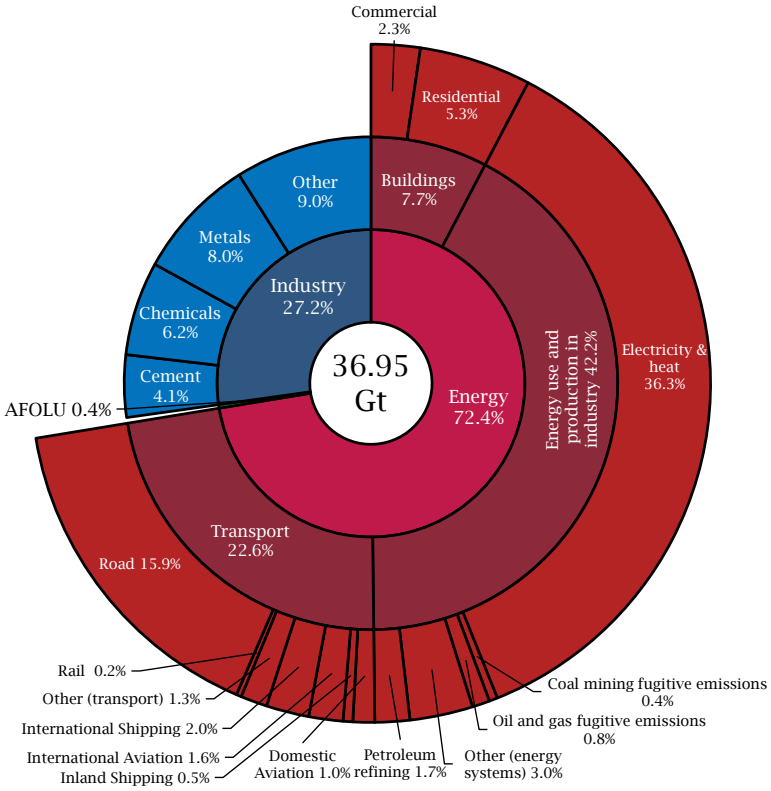

Figure 1.1: Sector break-down of global CO_2 emissions in 2019. AFOLU - Agriculture, Forestry, and Other Land Use. Data sourced from [3].

In response to the rising GHG emissions, many nations have aligned their emissions targets to the 2016 Paris Agreement, which aims to limit the change in average climate temperatures to 1.5 ˚C, compared to pre-industrial levels [4]. The IPCC has proposed four levers to reduce CO_2 emissions, which include reducing energy consumption through improving energy efficiency, switching to less carbon-intensive fuels, increasing the proportion of renewable energy in the global energy mix, and the capturing and storing of CO_2 [5].

For sectors, such as the electricity production sector, the switch to renewable energy sources and low-carbon-intensive fuels is technologically viable. However, some sectors, referred to as hard-to-abate sectors, have limited technological options to eliminate carbon-intensive fuels from their processes. For hard-to-abate industries, carbon capture utilisation and storage (CCUS) is relevant or remains the only least cost option to reduce CO_2 emissions [5].

1.2 CO_2 conditioning

CCUS is a long value chain, with four main components, presented in Figure 1.2. The first involves the capture of CO_2 from point sources, which is followed by its transportation to utilisation or storage sites. The CO_2 conditioning process ensures that (1) impurities after capture or from CO_2-rich streams are removed, and (2) prepares CO_2 for transportation at specific temperature and pressure conditions. Therefore, the conditioning process must produce a CO_2-rich stream that adheres to the specifications of CO_2 transportation, utilisation, and storage nodes.

Due to the significant scale of emissions from hard-to-abate sectors, presented in Figure 1.1, large-scale deployment of CCUS infrastructure is necessary to avoid CO_2 emissions. Though CO_2 capture and storage has been employed in multiple industries, such as Snøvhit LNG facility, Sleipner, and In Salah [6], the large-scale deployment is in its nascent stages with only the individual segments of the value chain demonstrated at an industrial scale [6]. The nascency of the CCUS value chain introduces certain risks. Some of these risks include uncertainty in carbon pricing, the number of pipeline users, and uncertainties related to the storage capacity of CO_2 sinks [7,8]. These uncertainties dictate that first-movers in the CO_2 CCUS chain need to design facilities that can withstand these uncertainties.

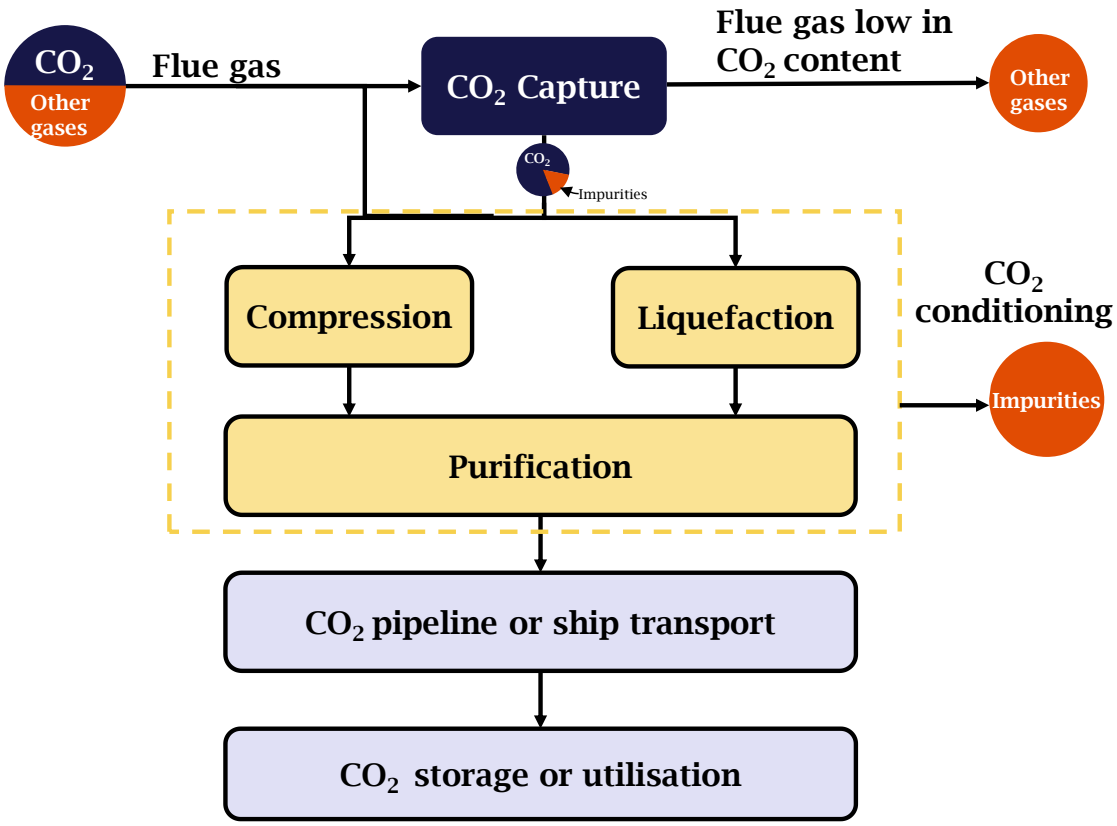

Figure 1.2: Block diagram summarising the CCUS value chain.

The scale of implementation of CCUS projects may require a great network of infrastructure connecting CO_2 point sources and sinks. The implications of this require an understanding of how impurities affect the properties of CO_2-rich streams and requires technology which will enable the real-time monitoring of these impurities across the CCUS value chain.

1.3 Objectives

The primary goal of this work is to improve the performance of the CO_2 conditioning process. This entails optimising the CO_2 conditioning process, improving the thermodynamic modelling and measurement of impurities relevant to CCUS. Therefore, the specific objectives of this thesis are:

1. To perform the optimisation of the CO_2 conditioning process, and assess the impact of CCUS uncertainties on conditioning facilities for pipeline CO_2 transport.
2. To improve the thermodynamic modelling of common impurities in the CCUS value chain.

3. To develop methodologies for the real-time measurement of impurity compositions in CO_2-rich streams, and streams relevant to CCUS.

1.4 Thesis structure

In alignment with the declared objectives, this thesis is further organised into six chapters as illustrated in Figure 1.3, and it is written as a paper-based thesis.

Chapter 2 sets the context of the study. It introduces the CCUS value chain, highlighting the differentiated role of the CO_2 conditioning process based on the various capture processes and flue gas compositions. A literature survey is also presented of the current work performed in the modelling of impurities in the CO_2 conditioning process while highlighting the gaps of current approaches. The chapter concludes with the analytical approaches used in high-pressure phase equilibria measurements.

Chapter 3 examines the pressurisation pathways employed for CO_2 rich transport via pipeline. Utilising a real-world case study of the 3D Dunkirk Carbon Capture Demonstration project, it examines the impact of pipeline sharing on CO_2 conditioning facilities. A comprehensive and fair comparison and optimisation of the conventional compression, and subcritical liquefaction and pumping processes are presented.

Chapter 4 considers another aspect of the conditioning process, which is ensuring that impurity specifications are met. This chapter provides an approach towards a predictive modelling of the phase equilibria of sulphur compounds in mixtures relevant to CCUS.

Chapter 5 presents the experimental work done in high-pressure water content measurements of CO_2, N_2, and H_2 using in-situ Raman spectroscopy. Here, the developed apparatus of these experiments is presented. Finally, this chapter focuses on improving the quantitative analysis methodologies of Raman spectroscopy, which has the potential for the real-time monitoring of CO_2-rich streams in the CCUS value chain.

Chapter 6 provides a final summary of the work undertaken in this thesis and highlights its specific contributions to the scientific and academic community. Additionally, this chapter outlines recommendations for future studies and investigations.

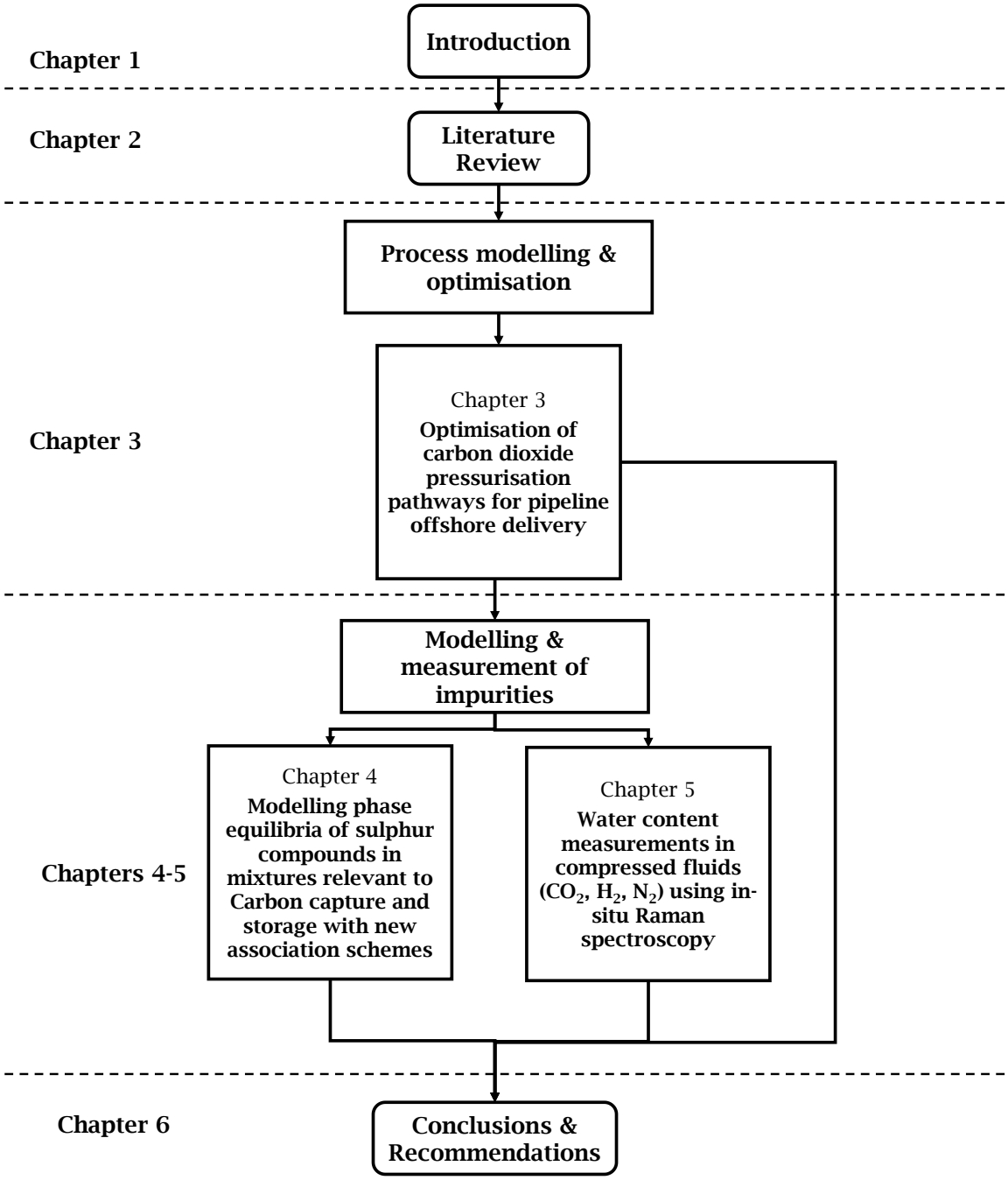

Figure 1.3: Thesis structure.

References

[1] IPCC, Climate Change 2007: Synthesis Report. Contribution of Working Groups I, II and III to the Fourth Assessment Report of the Intergovernmental Panel on Climate Change, Geneva, 2007.

[2] K. Calvin, D. Dasgupta, G. Krinner, A. Mukherji, P.W. Thorne, C. Trisos, J. Romero, P. Aldunce, K. Barrett, G. Blanco, W.W.L. Cheung, S. Connors, F. Denton, A. Diongue-Niang, D. Dodman, M. Garschagen, O. Geden, B. Hayward, C. Jones, F. Jotzo, T. Krug, R. Lasco, Y.-Y. Lee, V. Masson-Delmotte, M. Meinshausen, K. Mintenbeck, A. Mokssit, F.E.L. Otto, M. Pathak, A. Pirani, E. Poloczanska, H.-O. Pörtner, A. Revi, D.C. Roberts, J. Roy, A.C. Ruane, J. Skea, P.R. Shukla, R. Slade, A. Slangen, Y. Sokona, A.A. Sörensson, M. Tignor, D. van Vuuren, Y.-M. Wei, H. Winkler, P. Zhai, Z. Zommers, J.-C. Hourcade, F.X. Johnson, S. Pachauri, N.P. Simpson, C. Singh, A. Thomas, E. Totin, A. Alegría, K. Armour, B. Bednar-Friedl, K. Blok, G. Cissé, F. Dentener, S. Eriksen, E. Fischer, G. Garner, C. Guivarch, M. Haasnoot, G. Hansen, M. Hauser, E. Hawkins, T. Hermans, R. Kopp, N. Leprince-Ringuet, J. Lewis, D. Ley, C. Ludden, L. Niamir, Z. Nicholls, S. Some, S. Szopa, B. Trewin, K.-I. van der Wijst, G. Winter, M. Witting, A. Birt, M. Ha, IPCC, 2023: Climate Change 2023: Synthesis Report. Contribution of Working Groups I, II and III to the Sixth Assessment Report of the Intergovernmental Panel on Climate Change [Core Writing Team, H. Lee and J. Romero (eds.)]. IPCC, Geneva, Switzerland., 2023. https://doi.org/10.59327/IPCC/AR6-9789291691647.

[3] F. Monforti Ferrario, M. Crippa, D. Guizzardi, M. Muntean, E. Schaaf, E. Lo Vullo, E. Solazzo, J. Olivier, E. Vignati, EDGAR v6.0 Greenhouse Gas Emissions, 2021.

[4] UNFCC, Adoption of the Paris agreement, 2015.

[5] IPCC, IPCC Special Report on Carbon Dioxide Capture and Storage. Prepared by Working Group III of the Intergovernmental Panel on Climate Change, 2005.

[6] M.E. Boot-Handford, J.C. Abanades, E.J. Anthony, M.J. Blunt, S. Brandani, N. Mac Dowell, J.R. Fernández, M.-C. Ferrari, R. Gross, J.P. Hallett, R.S. Haszeldine, P. Heptonstall, A. Lyngfelt, Z. Makuch, E. Mangano, R.T.J. Porter, M. Pourkashanian, G.T. Rochelle, N. Shah, J.G. Yao, P.S. Fennell, Carbon capture and storage update, Energy Environ. Sci. 7 (2014). https://doi.org/10.1039/C3EE42350F.

[7] S.-Y. Lee, I.-B. Lee, J. Han, Design under uncertainty of carbon capture, utilization and storage infrastructure considering profit, environmental impact, and risk preference, Appl Energy 238 (2019) 34–44. https://doi.org/10.1016/j.apenergy.2019.01.058.

[8] M.M.J. Knoope, A. Ramírez, A.P.C. Faaij, Investing in CO2 transport infrastructure under uncertainty: A comparison between ships and pipelines, International Journal of Greenhouse Gas Control 41 (2015). https://doi.org/10.1016/j.ijggc.2015.07.013.

2 Literature Review

This section examines the literature of previous work performed in optimising the carbon dioxide conditioning process. It also evaluates the thermodynamic modelling approaches utilised to model mixtures relevant to CCCUS, and finally it explores impurity measurement techniques.

2.1 Carbon capture processes

Carbon capture utilisation and storage (CCUS) involves the capture of CO_2 from point sources, where CO_2 is isolated from other flue gas components. This is then followed by the transportation of the CO_2-rich stream to utilisation or storage nodes. The CO_2 conditioning process ensures that the CO_2-rich stream is in the required conditions (i.e. pressure and temperature), and it meets impurity specifications for transport, utilisation or storage.

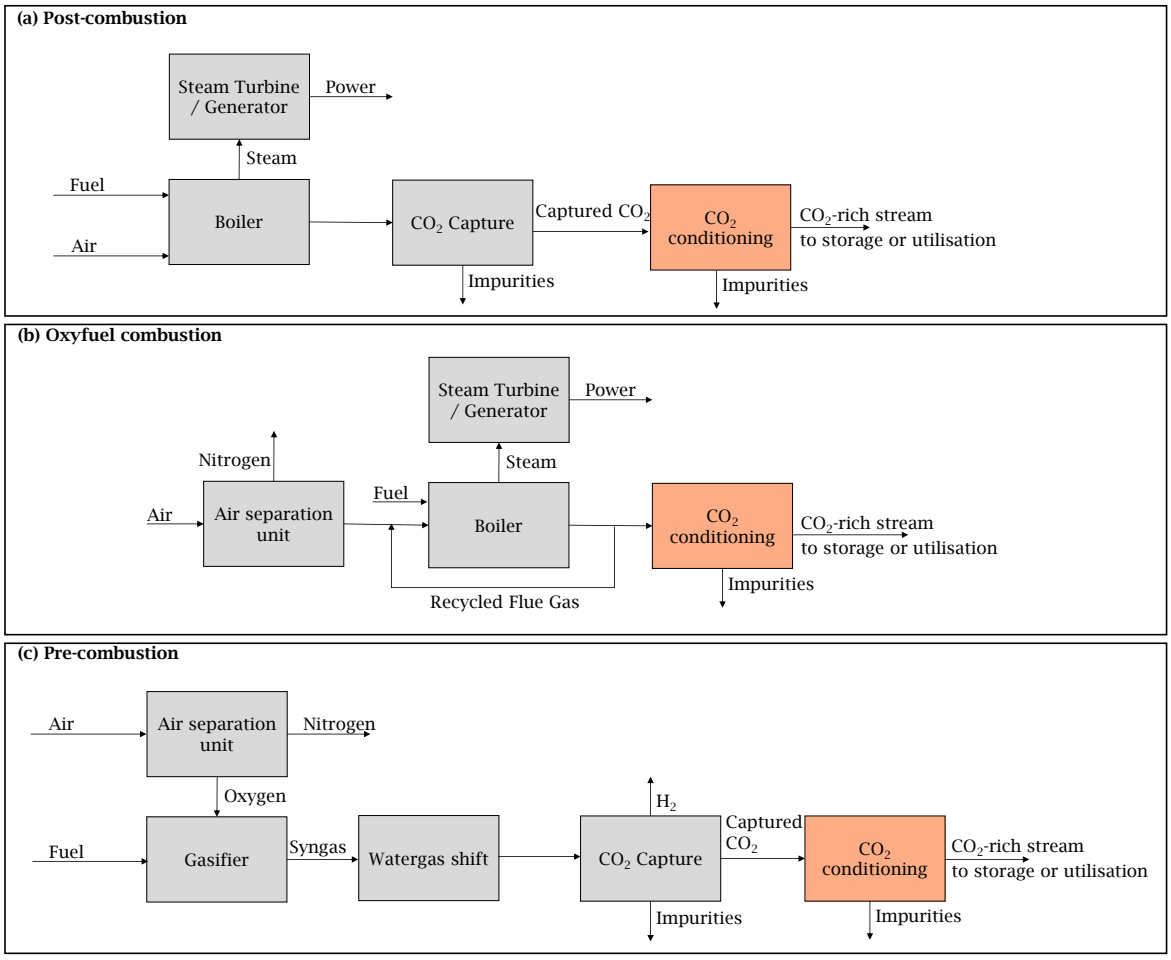

Figure 2.1: Block flow diagram of the different carbon capture pathways, highlighting the CO_2 conditioning process.

There are multiple pathways for the capture of CO_2 based on the flue gas composition. These pathways place a differentiated strain on the succeeding CO_2 conditioning process. The mature pathways for the power and industrial sectors are post-combustion, pre-combustion capture and oxy-combustion capture [1], illustrated inFigure 2.1. The typical compositions of the stream entering the CO_2 conditioning process are presented in Table 2.1, with these being compared to specifications of typical final CO_2 storage in a saline aquifer.

Table 2.1: Typical impurities from oxyfuel combustion, pre-combustion, and post-combustion prior to conditioning from Porter et al. [2] compared to storage specification in saline aquifer [3].

Compound	Oxyfuel	Pre-combustion	Post-combustion	Storage in saline aquifer
CO_2, mol%	71.5	> 98	> 99.7	>99.81
N_2, mol%	14.3	195 – 10000	0.045 – 0.18	<0.00005
H_2, mol%		20 – 10000		<50
O_2, ppmv	59000		61 – 150	<10
CO, ppmv		1 – 1667	10	<100
CH_4, ppmv		100 – 112		<100
Ar, ppmv	23000	1 – 1000	22 – 210	<100
SO_2, ppmv	4000	25	1 – 67.1	<10
NO, ppmv	400	400	1.5 – 38.8	
H_2O, ppmv	56000	5 – 600	100 – 640	<30
H_2S, ppmv		0.2 – 5968		<9
COS, ppmv		0.2 – 5968		
CH_3OH, ppmv		20 – 200		<30
Cl, ppmv		17.5	0.85	

The post-combustion process involves the capture of CO_2 from flue gas produced from the combustion of fossil fuels or carbonaceous material in an air atmosphere. This is commonly for the generation of power and/or process steam utilised in industrial processes. Due to the CO_2 composition in the flue gas being below 15%, an amine-based absorption process is commonly used in the capture process [4]. As this

process is highly selective to CO_2, it produces a captured stream with a CO_2 composition greater than 99.7 vol% [2].

The flue gas from the post-combustion process contains a significant amount of inert N_2 which places a significant load, such as higher energy requirements and capital investment, on the capture process. The oxy-combustion process aims to reduce this load, by performing the combustion in an oxygen-rich environment. This culminates in a flue gas stream enriched with CO_2 with a composition of between 70 and 96% [5]. To regulate temperatures in the boiler, a portion of the flue gas is recycled. Depending on the required final CO_2 composition, the stream is further enriched through a double flash or distillation process [2,5,6].

In comparison, the pre-combustion process involves the isolation of CO_2 prior to full combustion. This is achieved by introducing oxygen in a gasifier below the stoichiometric level for full combustion of the fuel. This process forms syngas (a mixture of CO_2, CO and H_2). Depending on the application, more H_2 can be formed through the watergas shift reaction. At this stage, the composition of CO_2 is typically between 15 to 60%. The capture process commonly utilises the Rectisol and Selexol processes to absorb CO_2 from the syngas stream producing a CO_2 composition above 98% [2].

The major CO_2 impurities entering the conditioning unit across all the processes are N_2, O_2, Ar, and H_2O, as presented in Table 2.1. Other common impurities are sulphur-containing compounds (SO_2, H_2S, COS) which may be formed in-process or enter the process alongside the combusted fuel [2,7]. Though the pre-combustion processes and post-combustion processes produce a stream rich in CO_2 (>98 mol%), transportation, utilisation or storage processes may require further removal of impurities (see saline aquifer CO_2 storage specification in Table 2.1). It must also be noted that there are other industrial processes than those presented in Figure 2.1, which introduce different classes and ranges of impurities into the CO_2 conditioning process. Some of these processes are biogas upgrading, cement manufacturing, and iron and steel industries. For the development of CO_2 conditioning processes, this underscores the need for the development of thermodynamic models that can accurately describe the phase behaviour of CO_2 and impurities found in the CCUS value chain.

2.2 Dynamics of CO_2 transport

Two major pathways are conceptualised for the transportation of CO_2 from point sources to storage or utilisation nodes, which are a network of pipelines and ship transport. The choice of transportation mode is largely driven by the distance between the point sources and storage or utilisation nodes, and the amount of CO_2 to be transported, although it is estimated that at distances greater than 1,000 km, ship transportation has a lower levelised cost [8].

In comparison to pipeline transport, ship transportation is favoured because of its flexibility. Ships can be designed to collect CO_2 from multiple point sources, and the delivery point can be altered to favour the lowest-cost CO_2 sinks.

Conversely, CO_2 pipeline capital investment is significant, accounting for about 85 to 90% of the levelised cost of pipelines [8]. Therefore, to justify investment of pipeline infrastructure requires large volumes of CO_2 to be transported. To maximise pipeline capacity, CO_2 is transported above 100 bar in the dense or supercritical phase where it has a high density [9,10]. Transportation in these phases reduces the risk of multiphase flow in the pipelines, which could occur through the transition of CO_2 from the gas to the liquid phase, and vice versa.

To reduce the levelised cost of pipelines, it is recognised that pipelines should be designed to be shared by various point sources. For this purpose, Chandel et al. [10] propose two pipeline designs: (1) a single-diameter trunkline, or (2) a multiple-diameter trunkline, which are shown in Figure 2.2. Chandel et al. [10] show that for the same mass flowrate of CO_2 from multiple point sources, single-diameter trunklines require significantly higher capital costs, however, a lower pressure drop can be achieved, therefore reducing the requirement for booster compressors along the pipeline's path. Moreover, whereas a multi-diameter trunkline necessitates precise knowledge of the location of point sources and their required transportation volumes, a single trunkline accommodates the inherent uncertainty in future CO_2 transportation demand. It is proposed that single-diameter should be oversized to accommodate future transportation demand, aligning with the dynamic nature of the current state of the CCUS value chain.

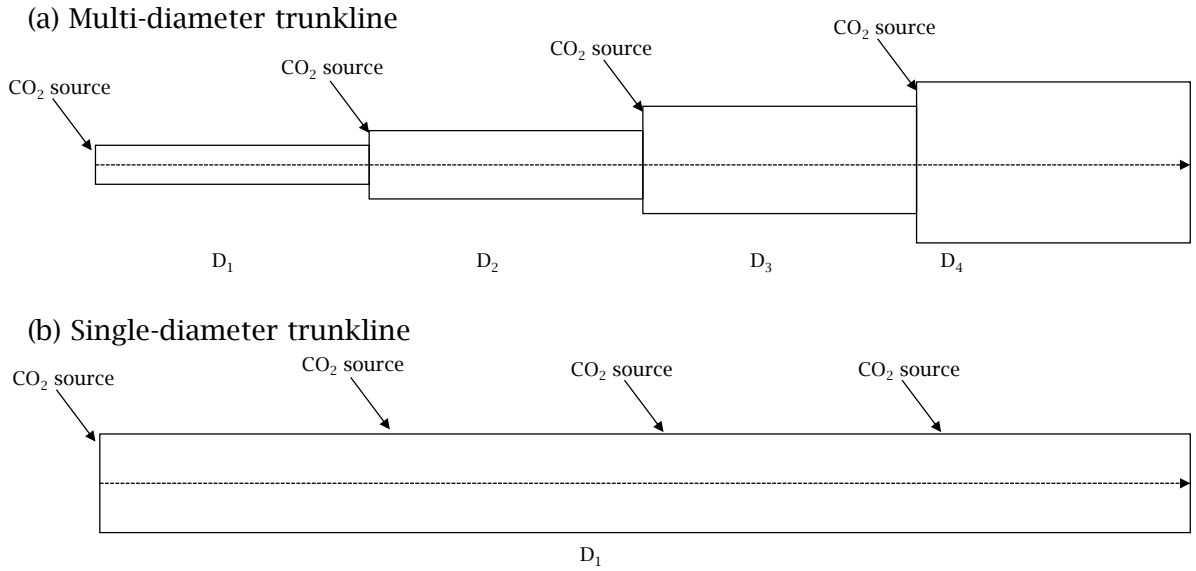

Figure 2.2: Pipeline designs to cater for CO_2 transportation from various sources, as proposed by Chandel et al. [10].

The sharing of pipelines introduces complexity in the CCUS value chain, due to differences in the CO_2-rich stream compositions from point sources. Impurities can alter the phase behaviour and the thermophysical properties of the captured CO_2 stream [11]. Furthermore, for pipelines, water is a concern as it could lead to corrosion, and at certain temperature and pressure conditions could trigger the formation of hydrates leading to pipeline plugging [12–14]. Other impurities of concern are non-condensable gases, such as N_2, O_2, and Ar, which affect the bubble and dew point of CO_2-rich streams. This shift in phase behaviour affects the conditioning process, as the CO_2-rich stream will need to be transported at a high pressure to avoid the transition to multiphase flow during transportation.

2.3 CO_2 conditioning process

The conditioning process is the interface between capture and transportation. The objectives of the CO_2 conditioning process are to meet the impurity and pressure specifications of transport, storage or utilisation nodes. Typically, the conditioning process will have multiple purification units to ensure adherence to compositional specifications. To meet the pressure requirements of the transportation, storage or utilisation sites, multistage CO_2 compression has emerged as the two viable pathways for pipeline transport [15].

To minimise energy consumption in the conditioning process, several studies have explored various strategies. In the context of power plants, Romeo et al. [16] and

Harken et al. [17] focused on the optimisation of the CO_2 intercooling compression process. They found that significant energy savings could be achieved through the integration of the compression circuit intercooling heat exchangers with the low-pressure steam cycle. Romeo et al. [16] proposed splitting the compression intercooling process into two stages, with the first stage being concerned with producing low-pressure steam from the condensate of the power generation steam cycle, and the second stage involved in cooling the CO_2 stream, ensuring a low temperature at the inlet of successive compressors. The drawbacks of this approach are that to achieve high temperatures in the CO_2 compression units for steam production, requires high compression ratios, which reduces the number of compressors but also increases power demand. Jackson and Brodal [15], optimised the compression process from CO_2-rich streams from pre-combustion, post-combustion, and oxyfuel combustion processes. They found that across all the processes, the compression ratio per stage had the most substantial impact in reducing energy consumption.

Though uncertainties in the downstream processes following CO_2 capture are well documented [18], they are not accounted for in the optimisation and design of CO_2 conditioning processes. Furthermore, across current studies, CO_2 liquefaction has been considered and optimised largely for ship transport, with limited assessment for pipeline transport. Therefore, the comprehensive optimisation of the conditioning process, considering the possible process schemes, and uncertainties in the CCUS value chain is required.

2.4 Thermodynamic modelling of impurities

The modelling of the phase equilibrium of mixtures common in the CCUS value chain has involved the use of classic cubic and association-based equations of state (EoS). Li and Yan [19] modelled various mixtures of CO_2 using Peng-Robinson, Redlich-Kwong (RK), Soave-Redlich-Kwong (SRK), Patela-Teja, and the three parameters with one parameter temperature dependent EoS (3P1T). However, these models had limited predictive capabilities and rely largely on fitting binary interaction parameters to binary data.

Furthermore, the classical cubic equations of state are unsuitable for mixtures with water, alcohols, glycols, and other polar or hydrogen bonding compounds [20]. To address this shortfall, the SAFT-based EoS such as PC-SAFT and CPA explicitly account for association by introducing a term from Wertheim's first-order

perturbation theory [21–23]. These equations of state have been successfully applied to predict the vapour liquid and liquid-liquid equilibrium of binary and multicomponent mixtures of polar or hydrogen bonding compounds [20].

Various studies by Tsivintzelis et al. [24–26] explored the utilisation of the CPA model in modelling mixtures relevant to the CCUS value chain. Here, a key approach was the allocation of different association sites to molecular CO_2, where it was considered to follow the 2B, 3B, and 4C association schemes. This improved the vapour liquid equilibrium predictions of CPA. A similar approach was used for H_2S where a limited number of association schemes were considered [27], and also led to improved modelling of the phase equilibria of binary mixtures containing H_2S.

2.5 Impurity measurements with Raman spectroscopy

Two main approaches are utilised in high-pressure phase equilibria experiments, with these being analytical and synthetic methods [28]. The differences in the methods depend on whether the sample has been prepared analytically or synthetically.

Analytical methods involve the compositional determination of the resulting phases at certain pressure and temperature conditions. Typically, a sample of each phase is extracted from an equilibrium cell and analysed ex-situ [28]. The samples are analysed utilising various chromatographic techniques to determine their composition. This approach has been utilised in multiple approaches to determine the phase equilibrium of CO_2 with other compounds [29–31]. However, the challenge of this approach, is that there is a risk of condensation in sampling capillaries, compromising the accurate evaluation of phase compositions [28]. Additionally, the ex-situ analysis is time-consuming, therefore limiting its application in online measurement, such as in CO_2 pipelines.

Raman spectroscopy offers an alternative as a non-invasive analytical approach, which would allow for the real-time monitoring of impurity compositions in CO_2-rich streams. The Raman scattering process shown in Figure 2.3, involves the interaction of a sample with light of a fixed wavelength. Upon interacting with the light, molecules in the sample shift to an excited energy state and can undergo one of three transitions. The most likely transition is an elastic process, where the molecule returns to its initial energy state, referred to as Rayleigh scattering. This culminates in a scattered light with the same wavelength as the incident light. The Raman effect is an inelastic process with a lower intensity by a factor of 10^3 relative to Rayleigh scattering [32]. Here, the molecule will be at a lower or higher energy level relative to

its initial state. Experiments are largely concerned with Stokes Raman scattering as it has a higher probability of occurrence than Anti-stokes Raman scattering. Due to the differences in the wavelength of the incident and scattered light, Raman scattering reveals the unique roto-vibrational modes of each compound in a sample. The distribution of resulting photons is commonly presented in Figure 2.3 (b). The wavenumber indicates the difference between the inverse wavelength of the incident light and the light from the Raman response.

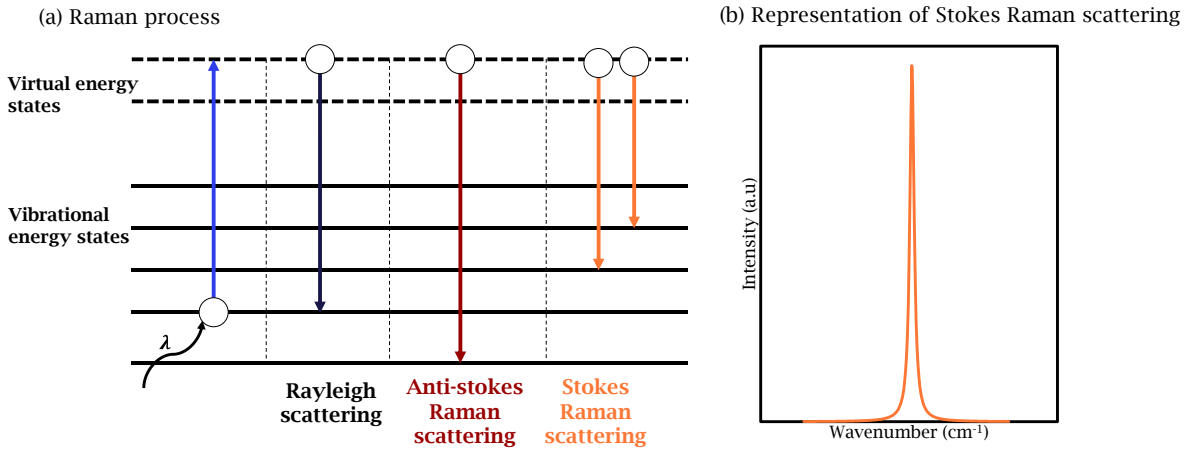

Figure 2.3: Representation of the Raman scattering process.

To perform compositional quantitative analysis, many studies have related changes in an analyte's relative Raman peak area relative to changes in content in a sample [33–35]. Caumon et al. [33] performed Raman measurements of the gas and liquid phase of the CO_2-water system. For the liquid phase, the relative peak area of CO_2 against that of water had a linear response to the amount of CO_2 dissolved in water, which could be utilised as a calibration. However, for the gas phase, changes in water peak areas against CO_2 did not reflect a linear response with changes in water content, culminating in a difficulty in developing a calibration. The current quantitative approaches have thus limited the application of Raman spectroscopy in industrial processes, such as on-line compositional monitoring.

References

[1] M. Bui, C.S. Adjiman, A. Bardow, E.J. Anthony, A. Boston, S. Brown, P.S. Fennell, S. Fuss, A. Galindo, L.A. Hackett, J.P. Hallett, H.J. Herzog, G. Jackson, J. Kemper, S. Krevor, G.C. Maitland, M. Matuszewski, I.S. Metcalfe, C. Petit, G. Puxty, J. Reimer, D.M. Reiner, E.S. Rubin, S.A. Scott, N. Shah, B. Smit, J.P.M. Trusler, P. Webley, J. Wilcox, N. Mac Dowell, Carbon capture and storage (CCS): the way forward, Energy Environ Sci 11 (2018) 1062–1176. https://doi.org/10.1039/C7EE02342A.

[2] R.T.J. Porter, M. Fairweather, M. Pourkashanian, R.M. Woolley, The range and level of impurities in CO2 streams from different carbon capture sources, International Journal of Greenhouse Gas Control 36 (2015) 161–174. https://doi.org/10.1016/j.ijggc.2015.02.016.

[3] Northern Lights JV DA, Liquid CO2 Quality Specifications, 2024.

[4] F.O. Ochedi, J. Yu, H. Yu, Y. Liu, A. Hussain, Carbon dioxide capture using liquid absorption methods: a review, Environ Chem Lett 19 (2021) 77–109. https://doi.org/10.1007/s10311-020-01093-8.

[5] V. White, R.J. Allam, Purification of Oxyfuel-Derived CO2 for Sequestration or EOR, 8th International Conference on Greenhouse Gas Control Technologies (2006).

[6] R.T.J. Porter, M. Fairweather, C. Kolster, N. Mac Dowell, N. Shah, R.M. Woolley, Cost and performance of some carbon capture technology options for producing different quality CO 2 product streams, International Journal of Greenhouse Gas Control 57 (2017) 185–195. https://doi.org/10.1016/j.ijggc.2016.11.020.

[7] P.D.N. Svoronos, T.J. Bruno, Carbonyl Sulfide: A Review of Its Chemistry and Properties, Ind Eng Chem Res 41 (2002) 5321–5336. https://doi.org/10.1021/ie020365n.

[8] M.M.J. Knoope, A. Ramírez, A.P.C. Faaij, Investing in CO2 transport infrastructure under uncertainty: A comparison between ships and pipelines, International Journal of Greenhouse Gas Control 41 (2015). https://doi.org/10.1016/j.ijggc.2015.07.013.

[9] Z.X. Zhang, G.X. Wang, P. Massarotto, V. Rudolph, Optimization of pipeline transport for CO2 sequestration, Energy Convers Manag 47 (2006). https://doi.org/10.1016/j.enconman.2005.06.001.

[10] M.K. Chandel, L.F. Pratson, E. Williams, Potential economies of scale in CO2 transport through use of a trunk pipeline, Energy Convers Manag 51 (2010). https://doi.org/10.1016/j.enconman.2010.06.020.

[11] A. Chapoy, M. Nazeri, M. Kapateh, R. Burgass, C. Coquelet, B. Tohidi, Effect of impurities on thermophysical properties and phase behaviour of a CO2-rich system in CCS, International Journal of Greenhouse Gas Control 19 (2013) 92–100. https://doi.org/10.1016/j.ijggc.2013.08.019.

[12] I.S. Cole, P. Corrigan, S. Sim, N. Birbilis, Corrosion of pipelines used for CO2 transport in CCS: Is it a real problem?, International Journal of Greenhouse Gas Control 5 (2011) 749–756. https://doi.org/10.1016/j.ijggc.2011.05.010.

[13] S. Adisasmito, R.J. Frank, E.D. Sloan, Hydrates of carbon dioxide and methane mixtures, J Chem Eng Data 36 (1991) 68–71. https://doi.org/10.1021/je00001a020.

[14] X. Lv, W. Li, B. Shi, S. Zhou, Study on the blockage mechanism of carbon dioxide hydrate slurry and its microscopic particle characteristics, RSC Adv 8 (2018) 36959–36969. https://doi.org/10.1039/C8RA07259K.

[15] S. Jackson, E. Brodal, Optimization of the Energy Consumption of a Carbon Capture and Sequestration Related Carbon Dioxide Compression Processes, Energies (Basel) 12 (2019). https://doi.org/10.3390/en12091603.

[16] L.M. Romeo, I. Bolea, Y. Lara, J.M. Escosa, Optimization of intercooling compression in CO2 capture systems, Appl Therm Eng 29 (2009). https://doi.org/10.1016/j.applthermaleng.2008.08.010.

[17] T. Harkin, A. Hoadley, B. Hooper, Reducing the energy penalty of CO2 capture and compression using pinch analysis, J Clean Prod 18 (2010) 857–866. https://doi.org/10.1016/j.jclepro.2010.02.011.

[18] S.-Y. Lee, I.-B. Lee, J. Han, Design under uncertainty of carbon capture, utilization and storage infrastructure considering profit, environmental impact, and risk preference, Appl Energy 238 (2019) 34–44. https://doi.org/10.1016/j.apenergy.2019.01.058.

[19] H. Li, J. Yan, Evaluating cubic equations of state for calculation of vapor–liquid equilibrium of CO2 and CO2-mixtures for CO2 capture and storage processes, Appl Energy 86 (2009) 826–836. https://doi.org/10.1016/j.apenergy.2008.05.018.

[20] G.M. Kontogeorgis, M.L. Michelsen, G.K. Folas, S. Derawi, N. von Solms, E.H. Stenby, Ten Years with the CPA (Cubic-Plus-Association) Equation of State. Part 1. Pure Compounds and Self-Associating Systems, Ind Eng Chem Res 45 (2006) 4855–4868. https://doi.org/10.1021/ie051305v.

[21] M.S. Wertheim, Fluids with Highly Directional Attractive Forces. III. Multiple Attraction Sites, 1986.

[22] M.S. Wertheim, Fluids with Highly Directional Attractive Forces. I. Statistical Thermodynamics, 1984.

[23] M.S. Wertheim, Fluids with Highly Directional Attractive Forces. II. Thermodynamic Perturbation Theory and Integral Equations, 1984.

[24] I. Tsivintzelis, G.M. Kontogeorgis, M.L. Michelsen, E.H. Stenby, Modeling phase equilibria for acid gas mixtures using the CPA equation of state. Part II: Binary mixtures with CO2, Fluid Phase Equilib 306 (2011) 38–56. https://doi.org/10.1016/j.fluid.2011.02.006.

[25] I. Tsivintzelis, S. Ali, G.M. Kontogeorgis, Modeling Phase Equilibria for Acid Gas Mixtures using the Cubic-Plus-Association Equation of State. 3. Applications Relevant to Liquid or Supercritical CO_2 Transport, J Chem Eng Data 59 (2014) 2955–2972. https://doi.org/10.1021/je500090q.

[26] I. Tsivintzelis, G.M. Kontogeorgis, Modelling phase equilibria for acid gas mixtures using the CPA equation of state. Part VI. Multicomponent mixtures with glycols relevant to oil and gas and to liquid or supercritical CO 2 transport applications, J Chem Thermodyn 93 (2016) 305–319. https://doi.org/10.1016/j.jct.2015.07.003.

[27] I. Tsivintzelis, G.M. Kontogeorgis, M.L. Michelsen, E.H. Stenby, Modeling phase equilibria for acid gas mixtures using the CPA equation of state. I. Mixtures with H2S, AIChE Journal 56 (2010) 2965–2982. https://doi.org/10.1002/aic.12207.

[28] R. Dohrn, J.M.S. Fonseca, S. Peper, Experimental Methods for Phase Equilibria at High Pressures, Annu Rev Chem Biomol Eng 3 (2012) 343–367. https://doi.org/10.1146/annurev-chembioeng-062011-081008.

[29] Y. Sanchez-Vicente, J.P.M. Trusler, Measurements and Modelling of Vapour–Liquid Equilibrium for (H2O + N2) and (CO2 + H2O + N2) Systems at Temperatures between 323 and 473 K and Pressures up to 20 MPa, Energies (Basel) 15 (2022) 3936. https://doi.org/10.3390/en15113936.

[30] A. Chapoy, C. Coquelet, H. Liu, A. Valtz, B. Tohidi, Vapour–liquid equilibrium data for the hydrogen sulphide (H2S)+carbon dioxide (CO2) system at temperatures from 258 to 313K, Fluid Phase Equilib 356 (2013) 223–228. https://doi.org/10.1016/j.fluid.2013.07.050.

[31] V. Savary, G. Berger, M. Dubois, J.-C. Lacharpagne, A. Pages, S. Thibeau, M. Lescanne, The solubility of CO2+H2S mixtures in water and 2M NaCl at 120°C and pressures up to 35MPa, International Journal of Greenhouse Gas Control 10 (2012) 123–133. https://doi.org/10.1016/j.ijggc.2012.05.021.

[32] M.J. Pelletier, Quantitative Analysis Using Raman Spectrometry, Appl Spectrosc 57 (2003) 20A-42A.

[33] M.-C. Caumon, J. Sterpenich, A. Randi, J. Pironon, Measuring mutual solubility in the H 2 O–CO 2 system up to 200 bar and 100 °C by in situ Raman spectroscopy, International Journal of Greenhouse Gas Control 47 (2016) 63–70. https://doi.org/10.1016/j.ijggc.2016.01.034.

[34] A.J. Parrott, P. Dallin, J. Andrews, P.M. Richardson, O. Semenova, M.E. Halse, S.B. Duckett, A. Nordon, Quantitative In Situ Monitoring of Parahydrogen Fraction Using Raman Spectroscopy, Appl Spectrosc (2018) 000370281879864. https://doi.org/10.1177/0003702818798644.

[35] R. Adami, J. Schuster, S. Liparoti, E. Reverchon, A. Leipertz, A. Braeuer, A Raman spectroscopic method for the determination of high pressure vapour liquid equilibria, Fluid Phase Equilib 360 (2013) 265–273. https://doi.org/10.1016/j.fluid.2013.09.046.

3 Optimisation of carbon dioxide pressurisation pathways for pipeline offshore delivery

Abstract

To maximise economies of scale of future CO_2 transport infrastructure, new CO_2 pipelines within the carbon capture utilisation and storage (CCUS) value chain, should ideally have excess capacity to satisfy future transportation demand. However, in scenarios where booster compressors cannot be employed along the pipeline, the rise in pipeline mass flow rate over time culminates in higher energy consumption of upstream compression/liquefaction. This work explores the optimisation of various CO_2 pressurisation pathways and assesses their flexibility in handling a variability in pipeline mass flow rates whilst delivering a captured CO_2 stream at a fixed final pressure of 100 barg. The study is based on the Dunkirk 3D Project, which has a planned nameplate capture capacity of 1 $MtCO_2/y$, with other CO_2 point sources taking up additional pipeline utilisation capacity. Two categories of CO_2 pressurisation pathways are considered, gas compression and subcritical liquefaction and pumping. These pathways are optimised to enable a fair comparison, considering the number of compression stages, compression ratio, and cooling/liquefaction system. Modelling results indicate that the temperature of the cooling utility has the greatest influence in reducing the overall work duty and sensitivity to a variability in pipeline mass flow rate. Furthermore, the utilisation of 5°C seawater as a cooling and liquefaction utility reduces the work duty of the conditioning process by 25.4% and requires fewer compression stages relative to conventional gas compression utilising cooling water at 30°C.

3.1 Introduction

Carbon Capture Utilisation and Storage (CCUS) is a key strategy towards the minimisation of anthropogenic CO_2 emissions and mitigation of climate change [1]. CCUS constitutes four value chain components: the capture of CO_2 from point sources, CO_2 conditioning, its transport via pipeline or ship, and finally its isolation from the atmosphere or its utilisation in other industrial processes. The conditioning process is an integral element of the value chain, as it ensures that CO_2 transport, storage and utilisation specifications are met. This process step involves the removal of minor impurities from the captured CO_2 stream and the pressurisation of this stream to the required pipeline inlet pressure or its liquefaction for ship transport.

The uptake of CO_2 capture technology will require the extensive development of new pipelines linking CO_2 point sources to sinks. Development of CO_2 pipelines could potentially occur through individual point sources building pipelines to their nearest sink, or it could occur through the development of a trunkline that transports captured CO_2 from multiple point sources [2]. The development of a shared trunkline provides economies of scale as it maximises returns from highly capital-intensive pipeline development. Furthermore, these economies of scale also ensure that distant and low-cost storage sites are accessible to point sources [2–4]. A study comparing the use of a single-diameter trunkline and three individual pipelines highlighted that these economies of scale rise sharply, the greater the distance from source to sink [4].

However, considering the significant capital required, the development of trunk pipelines has several uncertainties, such as the number of point sources utilising the pipeline, the CO_2 price, and uncertainties related to the storage capacity of CO_2 sinks [1,4]. Therefore, the design of CO_2 conditioning processes will need to account for these uncertainties, and in particular the variabilities in the pipeline mass flow rate. This requires an integrated approach to the design of conditioning processes and CO_2 pipelines.

The main drivers of pipeline costs are their inner diameter, wall thickness, length, and material of construction [5]. In long-distance transportation, the pipeline diameter can be minimised through the transportation of CO_2 in the supercritical or dense phase, as these phases have a significantly higher density relative to the vapour phase. This high density ensures that a large amount of fluid can be transported for a fixed pipeline diameter, lowers the pressure drop over the pipeline, and maximises capacity utilisation at storage sites [6].

The capture and conditioning process introduces a significant energy penalty in the CCUS value chain [7]. To minimise the energy consumption of the CO_2 conditioning process, diverse strategies have been explored. One study investigated the recovery of heat from steam generated in compressor interstage heat exchangers, through integrating cooling water with the low-pressure steam cycle [6]. This generated steam could then be utilised in the steam-intensive capture process or supplement power generation in a power plant. Another strategy for minimising conditioning work duty is through the insulation of pipelines when subcooled liquid CO_2 is transported in warm climates. This is because pipeline insulation would limit the heat transfer between a pipeline and its surrounding environment which reduces the pressure drop

across the pipeline. By insulating a pipeline, it was modelled that the transportation distance could be increased by 33% before vapourisation, therefore limiting the number of booster pumps along the pipeline [8]. However, insulated pipelines are not cost-effective for long-distance transportation.

Impurities have also been illustrated to impact the energy requirements along the CCUS value chain. The presence of impurities influences the thermophysical properties of the captured CO_2 stream, which may lead to a rise in pipeline pressure drop during transport relative to the transportation of pure CO_2 [9]. Moreover, the process streams with impurities have been shown to always have a greater compression work duty requirement relative to pure CO_2 [10].

The objectives of this study are to investigate the optimisation of two categories of pressurisation pathways for the pipeline delivery of CO_2, and to evaluate their work duty sensitivities to variations in the pipeline mass flow rate. These pressurisation pathways are gas compression, and subcritical liquefaction and pumping. This study is based on the 3D project, which aims at demonstrating the DMX™ process to capture CO_2 at a steel mill in Dunkirk, France.

3.2 Background to the 3D Project

The 3D project plans to validate the industrial deployment of CCUS in Dunkirk, France. Initially, the project will capture 1 $MtCO_2/y$ from a steel mill, and over time the Dunkirk site will develop as a cluster, enabling other point sources to utilise the developed CCUS infrastructure.

The 3D project has three concepts for the delivery of CO_2 to multiple storage sites across the North Sea, shown in Figure 3.1. Ship transport is considered for delivery across all concepts, while only Concept 1 and Concept 3, are considered for pipeline transport. The pipeline case for Concept 1 involves the delivery of captured CO_2 to a depleted oil or gas reservoir via a 300 km pipeline. For this concept, the delivery pressure would be ramped from 50 barg at the beginning of life of the process, to 120 barg as the reservoir fills. Alternately, a 200 km pipeline is considered for Concept 3, which would deliver captured CO_2 at a fixed pressure of 100 barg.

The current study exclusively focuses on the pipeline delivery of captured CO_2 stream via Concept 3.

Figure 3.1: 3D project CO_2 storage concepts across the North Sea. Concepts 1 and 3 are considered for pipeline transport, while Concept 2 is evaluated for ship transport. This study exclusively focuses on the pipeline delivery of CO_2 via Concept 3.

3.3 Process simulation and optimisation approach

3.3.1 Overall study approach

The Dunkirk 3D project is employed as a case study, with the following systematic simulation approaches being employed:

- The modelling approach is developed and validated,
- The required pipeline inlet pressure is modelled for various mass flow rates at a selection of pipeline diameters, and fluid inlet temperatures,
- The drivers of electricity consumption within the CO_2 conditioning process are identified for the process schemes at a nameplate conditioning capacity of 1 $MtCO_2/y$,
- Process schemes are optimised based on identified drivers of electricity consumption culminating in process scheme alternatives,
- The effect of pipeline mass flow rate variability (due to additional transportation requirements from other CO_2 point sources) on the work duty

requirements for the optimised process schemes is assessed up to a pipeline flow rate of 5 $MtCO_2/y$.

3.3.2 Theory and assumptions

ASPEN HYSYS® is used to conduct the pipeline thermohydraulic analysis and computation of energy requirements for the various pressurisation routes. Here, the Peng-Robinson Equation of State [11] is used to evaluate phase properties, such as density, enthalpy and heat capacity throughout the simulation. Previous studies have shown that the Peng-Robinson equation of state grants reasonable accuracy within the evaluated regions of this study [12,13].

The captured CO_2 enters the conditioning process at a pressure of 5.6 barg and a temperature of 44˚C. As the majority lies offshore, the captured CO_2 stream is expected to approach North Sea temperatures of 5 ˚C for transportation via an uninsulated pipeline. Therefore, a thermohydraulic approach is adopted for the computation of pressure drop along the pipeline. This approach accounts for heat exchange between the surrounding pipeline environment and the transported fluid. Pressure drop across the pipeline is determined from the Darcy-Weisbach equation [14], shown in equation (3.1), in its differential form. The pipeline is simulated as horizontal, single-diameter, and its elevation is not considered as a variable, as it is assumed to be constant along the pipeline's pathway.

$$dP = f\frac{\rho u^2}{2D}dL \tag{3.1}$$

Equation (3.1) shows the dependency of the differential pressure drop on both fluid and pipeline properties. It relates the pressure drop to the differential length of the pipeline, dL, pipeline inner diameter, D, pipeline frictional factor, f, fluid mass density, ρ, and fluid velocity along the pipeline, u. For all simulation cases, the pressure at the outlet of the pipeline, p_{out} is kept at a constant value and set to the required final concept delivery pressure of 100 barg.

The volumetric flow rate across the pipeline, can be represented by the term on the left in equation (3.2), which can be further simplified to the right-hand side, with the second term on the right representing the cross-sectional area of the pipeline.

$$\frac{\dot{m}}{\rho} = u\left(\frac{\pi D^2}{4}\right) \tag{3.2}$$

Combining equations (3.1) and (3.2) for single-phase transport, through the substitution of the fluid velocity, generates the final pressure drop equation (3.3).

This simplified equation results in a direct relationship between the pressure drop and the mass flow rate, $\dot{m}$. In addition to the mass flow rate, equation (3.3) shows that the fluid density and pipeline inner diameter have a significant influence on the pressure drop.

$$dP = \frac{8f\dot{m}^2}{\rho\pi^2 D^5} dL \tag{3.3}$$

During transport, heat transfer between the fluid and the surrounding environment occurs, driven by their difference in temperature $(T_f - T_s)$. This heat transfer influences the fluid density, in equation (3.3), and hence the differential pressure drop, along the pipeline. The entire pipeline is simulated to be horizontal and lying offshore surrounded by water which is at a constant temperature T_s of 5 ˚C. In this study, convection heat transfer within the pipeline, convection heat transfer between the fluid and pipeline wall, heat conduction through the pipeline wall, and convection heat transfer between the outer wall of the pipeline and surrounding fluid were all accounted for. The overall heat transfer is therefore determined from the following:

$$Q_w = UA(T_f - T_s) \tag{3.4}$$

Where,

$$U = \frac{1}{\frac{1}{h_i} + \frac{r_o}{k}\ln\left(\frac{r_0}{r_i}\right) + \frac{1}{h_o}}$$

Where U, A, h_i and h_o are, respectively, the heat transfer coefficient, differential area of the pipeline, internal and external convection coefficient. Then r_i and r_o are, respectively the internal and external radius, while k is the pipeline material thermal conductivity.

The total power required for an n number of compression or pumping stages is computed as:

$$W_{comp} = \dot{m}\sum_{i=1}^{n}\frac{1}{\eta_i}\int_{P_{in}}^{P_{out}}\left(\frac{dp}{\rho}\right)_s \tag{3.5}$$

Where P_{out} and P_{in} are, respectively, the outlet and inlet pressure of compressor i. $\dot{m}$ is the mass flow rate, and ρ being the mass density, η_i is the adiabatic efficiency of the pressurisation step i, which is kept constant at 75% for all cases. In equation (3.5), s represents an isentropic pressure change.

In simulating the energy consumption for the various pressurisation routes, interstage cooling is simulated to keep the inlet of each compressor at a specified temperature. The total cooling and refrigeration duty, Q, is computed through:

$$Q = \dot{m} \sum_{i=i}^{n} \left(\hat{H}_{i-1}^{out} - \hat{H}_{i-1}^{in} \right) \tag{3.6}$$

where $\hat{H}_{i-1}^{out}$ and $\hat{H}_{i-1}^{in}$ are, respectively, the specific mass enthalpy of the outlet and inlet heat exchanger stream.

3.3.3 Validation of process modelling

To validate the process modelling approach performed in ASPEN HYSYS, the process configuration presented by Martynov and co-workers [15] for two different stream compositions were recreated. In their work, Martynov and co-workers investigate the effect of impurities on work duty requirements, where the Peng-Robinson equation of state is also utilised. The key modelling parameters used by Martynov and co-workers is shown in Table 3.1, where conventional multistage compression was utilised.

Table 3.1: Process configuration parameters presented by Martynov and co-workers [15].

Conditioning Process	
Captured CO_2 temperature	38 ˚C
Captured CO_2 stream	15 bar
Captured CO_2 final pressure at pipeline inlet	151 bar
Interstage cooling temperature	38 ˚C
Number of compressor stages	4
Compressor efficiency ($\eta_{compressor}$)	75%

The results of the remodelling is shown in Table 3.2 and performed for two stream compositions. Table 3.2 indicates that the deviation from the reported work and the remodelling performed in this study is minimal across the two feed compositions.

Table 3.2: Comparison of reported [15] and modelled work duty, based on compression circuit described in Table 3.1 at two stream compositions.

	Composition 1 (Pure CO_2)	Composition 2*
Reported Work Duty	39 kWh/tonCO_2	41 kWh/tonCO_2
Modelled Work Duty	39.38 kWh/tonCO_2	41.27 kWh/tonCO_2
Deviation in Work Duty	1.0%	0.66%

* Composition 2 – CO_2 98.07 vol%, N_2 0.02 vol%, Ar 0.018 vol%, SO_2 700 ppmv, H_2O 150 ppmv, CO 1300 ppmv, H_2S 1700 ppmv, H_2 15000 ppmv, CH_4 100 ppmv.

3.3.4 Process optimisation methodology and constraints

The objective function of the process optimisation is to determine the set of operating conditions to minimise the total conditioning process work duty, which is the sum of the work duty from process compressors, pumps, and refrigeration compressors, as follows:

$$\min E(n_c, CR, P_l, T_i) = \sum_{n_c} W_{process\ comp} + \sum_{n} W_{refrigeration\ comp} + W_{pump} \tag{3.7}$$

An end-to-end optimisation algorithm was followed for the optimisation of the CO_2 pressurisation pathways shown in Figure 3.2. Three core sections were considered for optimisation: (i) the compression of captured CO_2, (ii) Liquefaction of CO_2, and (iii) CO_2 pipeline transport. In this study, two process pathways are considered for the pressurisation of CO_2, namely gas compression and the subcritical liquefaction and pumping. The gas compression route bypasses the liquefaction section and delivers CO_2 at the required pipeline inlet pressure. The pipeline pressure drop was modelled for different pipeline diameters and for scenarios where the pipeline transported CO_2 from other CO_2 point sources. The pipeline dynamics determined the required pipeline inlet pressure ($P_{pipeline}$) to ensure a final CO_2 delivery at 100 barg.

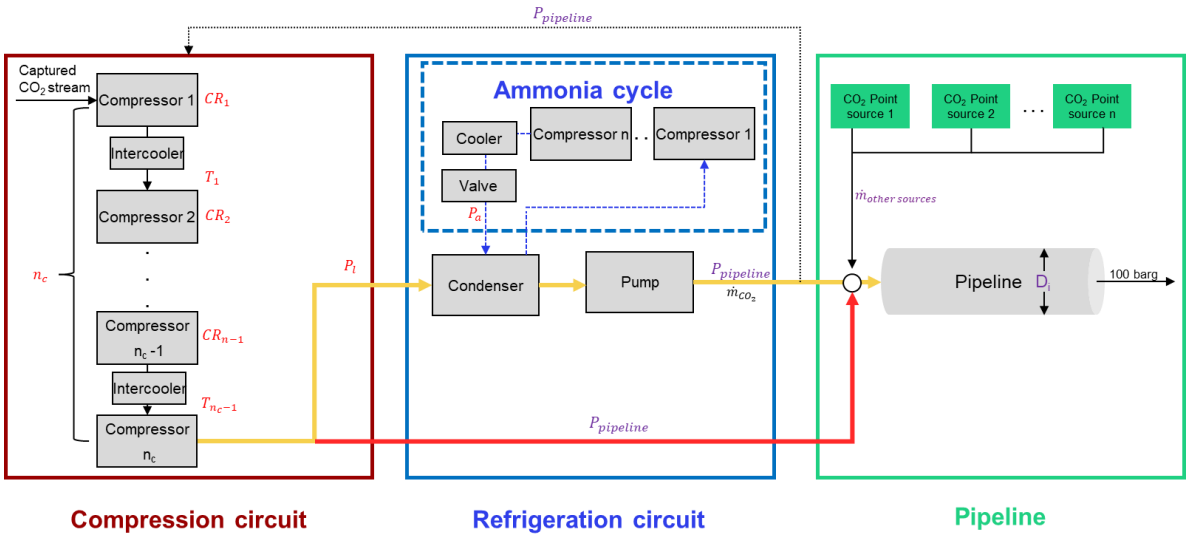

Figure 3.2: Optimisation algorithm for the CO_2 pressurisation pathways. The variables in red indicate optimisation variables, while those in purple show variables adjusted based on considered scenarios. The lines in red indicate the gas compression pathway, with the subcritical compression and pumping pathway shown in yellow.

The optimisation variables include the number of compression stages (n), intercooling temperature (T_i), and the compression ratio (CR) at each stage. The liquefaction pressure (P_l) is also optimised for the subcritical liquefaction and pumping conditioning pathway. The final number of compression stages is determined when an addition of a compression stage to the process does not achieve more than 2% in work duty savings, which has also been identified as the breakpoint in other studies [16]. The constraints of the process simulation and modelling are presented in Table 3.3, with these being fixed for all process schemes.

Table 3.3: Summary of constraints throughout simulation and optimisation.

Captured CO_2 stream composition (mol. Fractions)	
CO_2	0.9823
CO	0.0003
H_2O	0.0174
Conditioning Process	
Heat exchanger minimum approach temperature	≥5 ˚C
Cooling water temperature	30 ˚C
Seawater temperatures	5˚C/20˚C
Heat exchanger pressure drop	0.1 bar
Mass flow rate processed in conditioning plant	1 $MtCO_2$/y
Pump efficiency (η_{pump})	75%
Compressor efficiency ($\eta_{compressor}$)	75%
Captured CO_2 temperature	44.9 ˚C
Captured CO_2 pressure	4.6 barg
Pipeline	
Pipeline length (L)	200 km
Final pipeline delivery pressure	100 barg
Pipeline ambient temperature (T_{amb})	5 ˚C
Pipe wall conductivity (k)	45 W/m.K
Pipe roughness	45.72 μm
Internal heat transfer coefficient (h_i)	4492 kJ/m^2. ˚C
External heat transfer coefficient (h_o)	7693 kJ/m^2. ˚C

3.4 Results and discussion

3.4.1 Influence of the pipeline inner diameter and mass flow rate on required pipeline inlet pressure

Figure 3.3 presents the required CO_2 inlet pipeline pressure for various pipeline mass flow rates as a function of pipeline inner diameters, for final CO_2 delivery at 100 barg. The pressure drop across the pipeline which is driven by the pipeline mass flow rate and the fluid inlet temperature were all accounted for.

The required fluid pipeline inlet pressure rises nonlinearly with a reduction in the pipeline diameter. This is since for a certain CO_2 mass flow rate, smaller pipeline inner diameters lead to high fluid velocities which culminate in significant frictional losses. Though pipelines with a small pipeline diameter have a lower capital requirement, the higher pressure operations increases the required pipeline wall thickness, and also culminates to higher conditioning operating costs and energy requirements. In contrast, pipelines with a large inner diameter can transport more fluid and only require a slight rise in the fluid inlet pressure with a shift in pipeline operating capacity. In particular, a pipeline with a 22-inch inner diameter would require a 9.4% rise in the fluid pipeline inlet pressure to meet a shift in pipeline mass flow rate from 1 Mt/y to 5 Mt/y. Though pipelines with a larger inner diameter accommodate mass flow variability, this benefit must be weighed against the higher pipeline capital costs.

The influence of the fluid pipeline inlet temperature on the pressure drop relies on the pipeline diameter and pipeline mass flow rate. Fluid at a lower temperature, enters the pipeline at a higher density, resulting in lower frictional losses across the pipeline, as per equation (3.3). The fluid inlet temperature plays a critical role for smaller pipeline diameters and higher mass flow rates, where pressure drop savings of up to 10.5% can be realised by supplying a fluid at the inlet of the pipeline at 5˚C rather than 44˚C.

Additionally, Figure 3.3 illustrates the need for the conditioning process to be responsive to a variability in the pipeline mass flow rate as this significantly impacts the required inlet pressure. In onshore pipelines, this can be resolved through the introduction of booster compressors to maintain a pressure above the CO_2 critical point, which prevents undesirable multiphase pipeline transport [2]. In contrast, booster compressors lead to significant additional capital requirements and their implementation is unfeasible for an offshore pipeline [1].

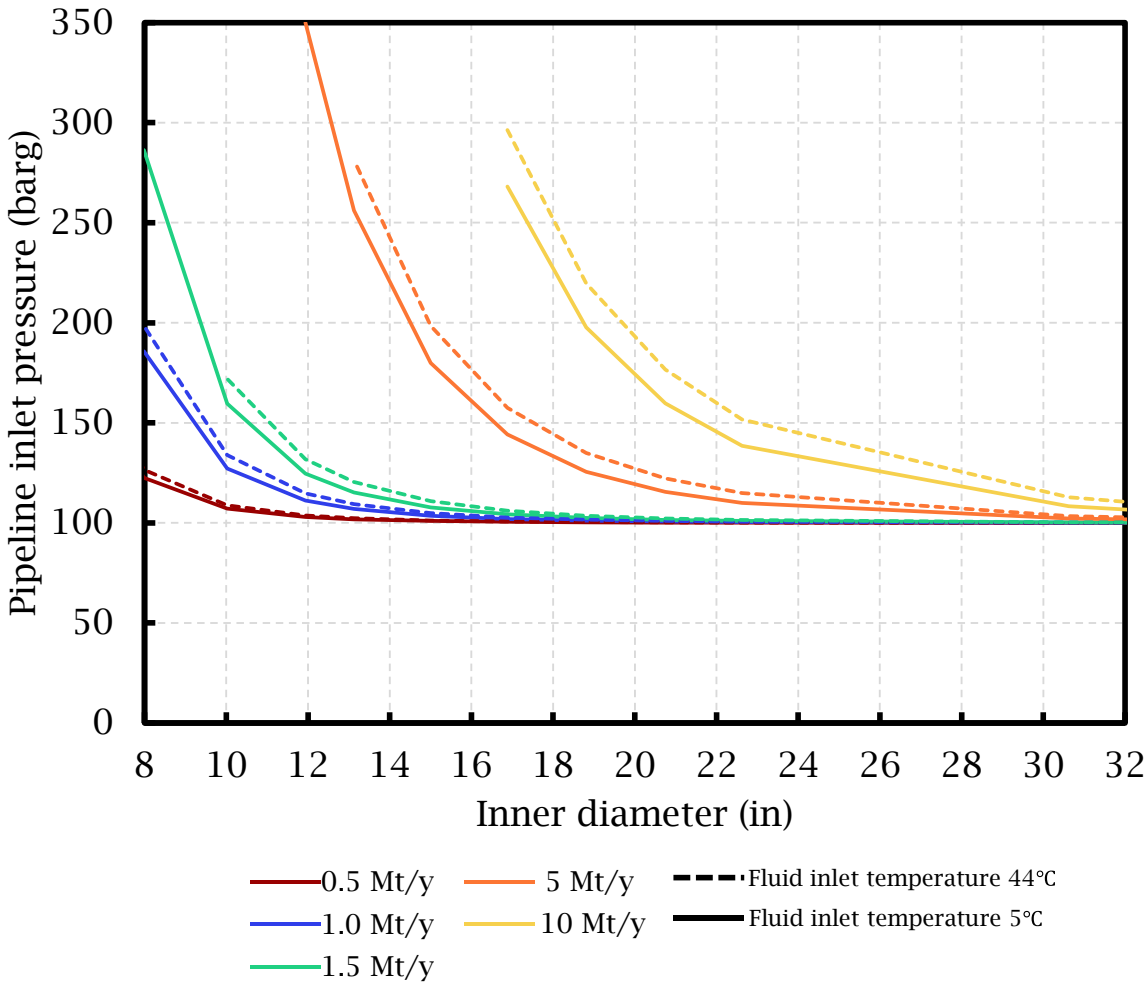

Figure 3.3: Pipeline inlet pressure at various mass flow rates and pipeline inner diameters, for the final delivery of captured CO_2 at 100 barg.

3.4.2 Base case process schemes

Two categories of conditioning pressurisation pathways are considered for the delivery of CO_2 to a Concept 3 pipeline, with these being gas compression (Case 1a), and the subcritical liquefaction and pumping (Case 2a and 2b), shown in Figure 3.4. Across these process schemes, several process variables, which are highlighted, are optimised.

(a) Case 1a: Gas compression with cooling water

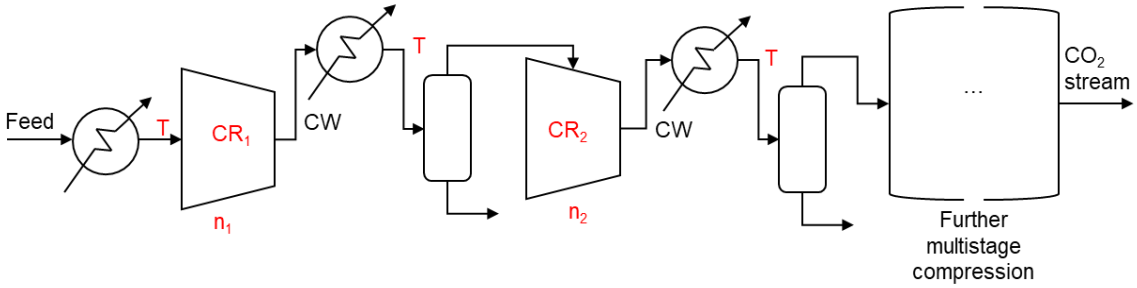

(b) Case 2a: Closed cycle liquefaction with ammonia and pumping

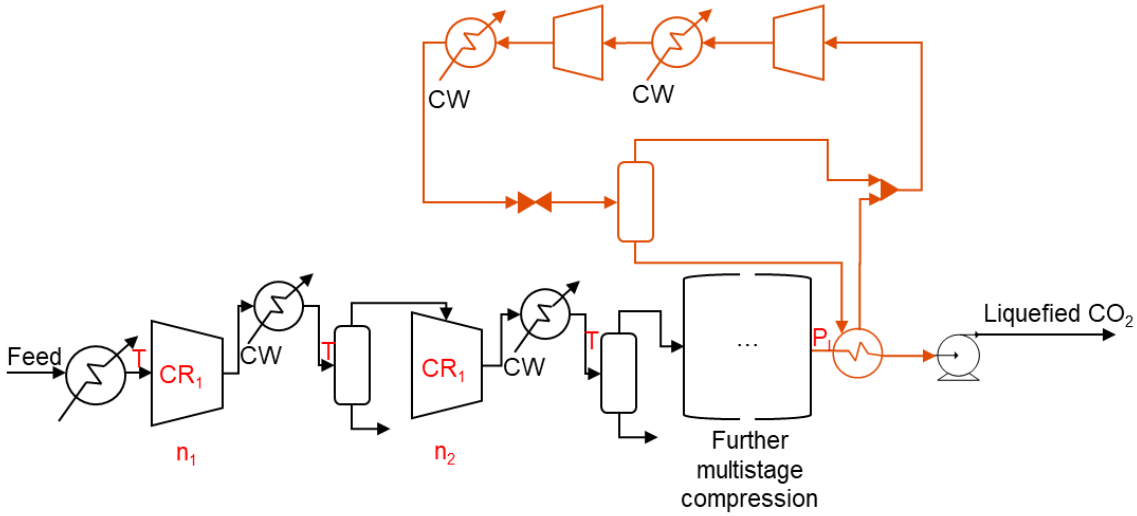

(c) Case 2b: closed cycle liquefaction with heat integration and pumping

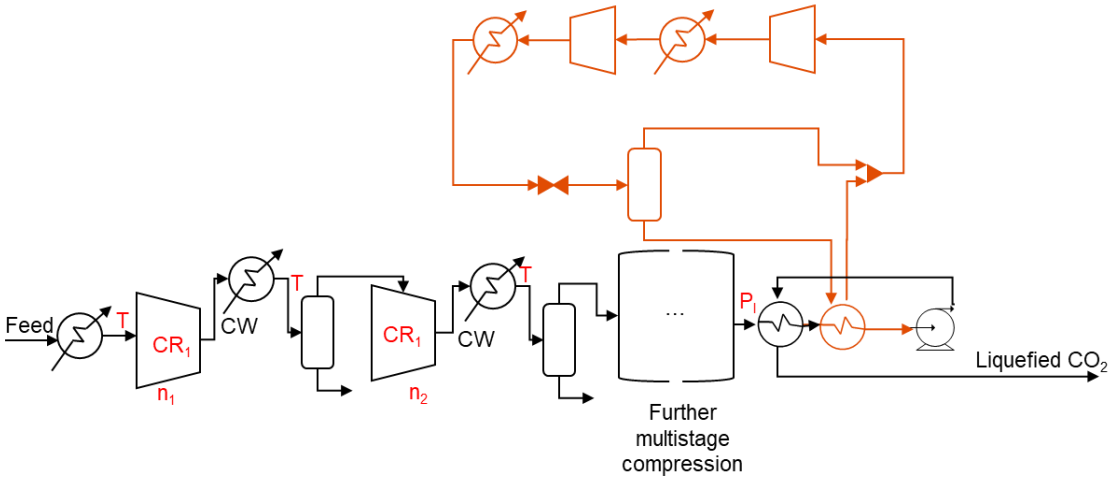

Figure 3.4: Base case process schemes for the conditioning of captured CO_2 stream, utilising cooling water (CW). The process units related to the refrigeration process are indicated in orange, while the optimised process variables are represented in red.

3.4.2.1 Gas compression process scheme (Case 1a)

The gas compression scheme, shown in Figure 3.4(a), initially cools the captured CO_2 stream from the DMX™ facility. This pathway involves the exclusive use of multistage compressors with interstage cooling, to deliver the captured CO_2 in the supercritical phase at the inlet of the pipeline. Following each interstage cooler, the stream is flashed to remove condensates before it undergoes further compression. As North Sea temperatures fall far below the critical temperature of CO_2 throughout the year, the transported fluid would transition from the supercritical phase to the dense phase during pipeline transport.

3.4.2.2 Subcritical liquefaction and pumping process schemes (Case 2a, 2b)

The subcritical liquefaction and pumping pathway shown in Figure 3.4 (b) (c), takes advantage of the lower capital costs of pumps relative to compressors (Duan et al., 2013). This pathway has two key steps, the initial compression of CO_2, followed by its liquefaction and pumping to pipeline conditions. In this pathway, the captured CO_2 is initially cooled and compressed in a similar compression circuit as Case 1a. Here, the captured stream is then delivered at the liquefaction pressure at which the captured CO_2 is condensed.

The ammonia refrigeration cycle is utilised to liquefy the compressed CO_2 stream. This cycle involves the multistage compression of ammonia to 12 bar, which enables the utilisation of cooling water to cool the ammonia stream. Following this, the ammonia stream is depressurised, with the vapour phase being separated from the liquid phase through a flash process unit. The ammonia depressurisation pressure is simulated to depend on the delivered CO_2 liquefaction pressure such that a minimum temperature approach of 5˚C is attained in the captured CO_2 condenser.

Following this, the liquefied CO_2 stream is then pumped to the required pipeline inlet pressure. For this pathway, two process schemes are considered, with each employing the ammonia refrigeration cycle to liquefy the captured CO_2 stream (Case 2a and Case 2b). The distinction between Case 2a and Case 2b is that Case 2b includes potential heat integration, through the pre-cooling of the compressed gas before further liquefaction with ammonia (see Figure 3.4 (c)).

It is important to note, that in both cases, the role of the compression circuit is to deliver the CO_2 stream at a specific pressure, at which the stream is liquefied.

3.4.3 Base case process scheme optimisation

The optimisation of the base case gas compression and subcritical liquefaction and pumping pathways are presented.

3.4.3.1 Gas compression optimisation (Case 1)

Energy consumption over the compression circuit is driven by four variables: the number of compression stages, compression ratio at each stage, compressor efficiency, and the fluid temperature at the inlet of the compressor. In all cases, the compressor efficiency was fixed at 75%. Figure 3.5 illustrates the effect of these variables on the gas compression process scheme work duty for equal compression ratios and optimised compression ratios at various interstage cooling temperatures.

The reduction of the compressor CO_2 inlet temperature has a positive effect on the compression duty requirement, with a reduction of up to 7.9% in overall energy consumption achievable when compressor inlet temperatures are reduced from 44°C to 30°C. This is since at lower temperatures, a high volumetric compressor intake is reached (due to higher fluid density) relative to higher temperatures. Additionally, compression at lower temperatures reduces compressor sizes, which in turn reduces the capital requirement of the compression circuit. However, this reduction in compressor duty at lower temperatures requires the rejection of more heat in interstage heat exchangers (see Figure 3.5 (b)).

Increasing the number of compression stages further positively affects the overall energy consumption of the compression circuit, as an increase in the number of compression stages from 4 to 8, culminates in a total energy reduction of about 10.9%. However, it should be noted that the installation of more compression stages increases capital requirements. To limit the rise in capital requirements, the compression ratio for a fixed number of compressors can be optimised. Through this optimisation, work duty savings of up to 4.2% can be achieved. However, this energy-saving benefit declines at higher interstage cooling temperatures and with the rise in the number of compression stages.

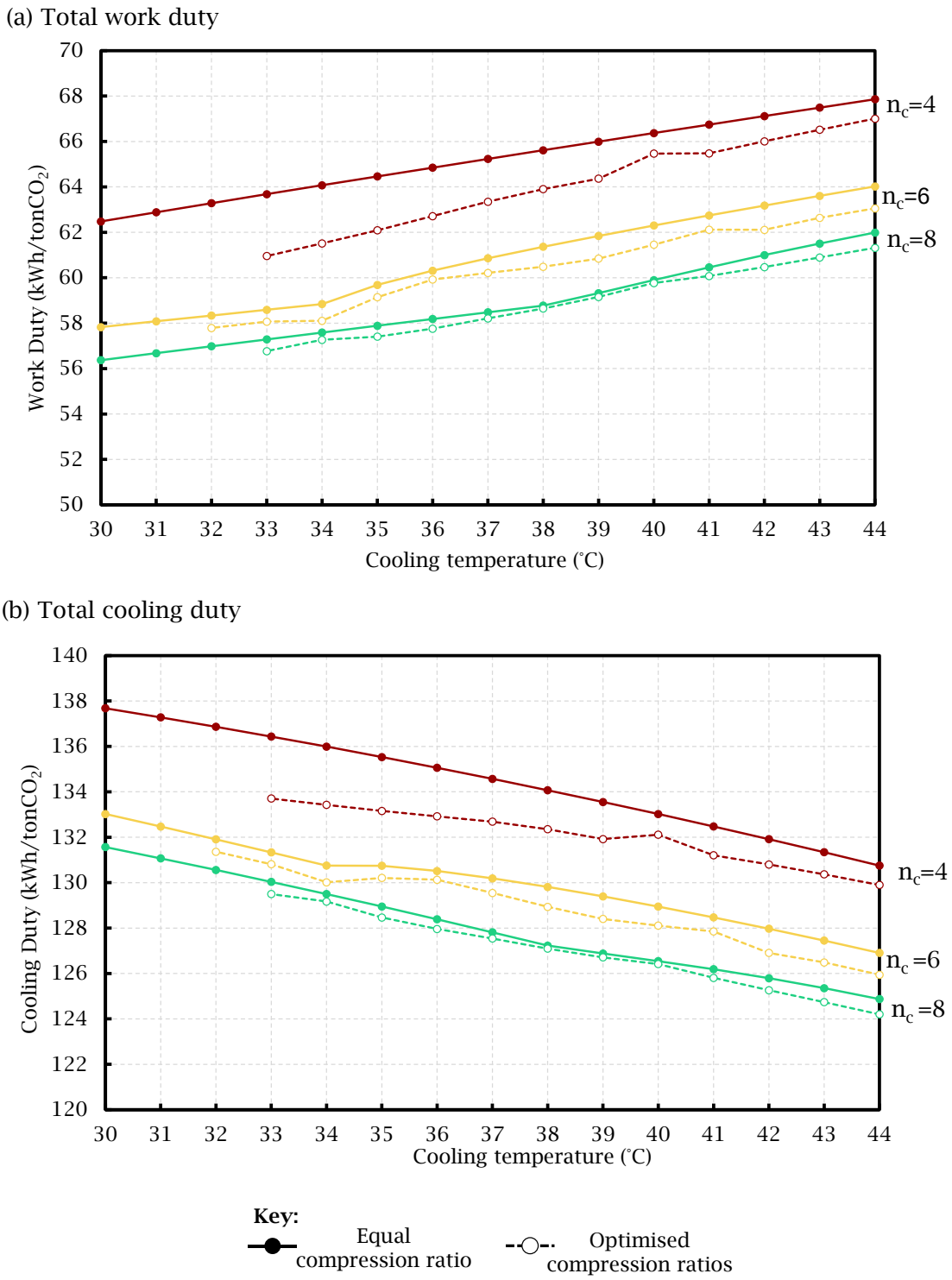

Figure 3.5: The effect of intercooling temperature, compression stages, and compression ratio on (a) total compression duty, and (b) total cooling duty. This is for compression of a CO_2 stream for transport via 10-inch pipeline diameter.

For the gas compression base cases, Figure 3.5 (a) shows that the optimal process scheme would require 8 compression stages, with additional compressor savings leading to less than 2% in work duty savings. To maintain a 5°C minimum temperature

approach, the interstage temperature was fixed at 35˚C for base cases where cooling water available at 30˚C was utilised.

3.4.3.2 The effect of liquefaction pressure on work duty

Figure 3.6 shows the effect of the liquefaction pressure on the work duty for the different areas of process schemes Case 2a and 2b. The liquefaction pressure is defined as the stream pressure delivered after the compression circuit and before liquefaction. A similar methodology, as in section 3.4.3.1, was followed to optimise the compression circuit of the subcritical liquefaction and pumping process schemes at each liquefaction pressure. The ammonia temperature was varied at each stream liquefaction pressure to maintain a 5˚C minimum temperature approach in the condenser.

Figure 3.6 reveals that there exists a trade-off between process compressor and refrigeration compressor duties. In line with expectations, the process compressors perform less work for stream delivery at low liquefaction pressures, as they operate at low compression ratios at these conditions. In contrast, the refrigeration compressor duty rises steeply at low liquefaction pressures, as the CO_2 enthalpy of condensation rises with a decline in pressure. This culminates in a high ammonia mass flow rate in the refrigeration cycle and refrigeration cycle compressors operating at a high compression ratio, leading to a higher refrigeration cycle work duty at low liquefaction pressures.

Overall, the total work duty of the process schemes, respectively, declines by 23.2% and 16.2% with a rise in liquefaction pressure from 15 bar to 45 bar for Case 2a and 2b. Furthermore, pre-cooling of the CO_2 stream (Case 2c) significantly reduces the work duty requirement of the refrigeration cycle, with a duty saving of up to 9.1% achievable at a 15 bar liquefaction pressure. However, this energy savings with heat integration decline at higher liquefaction pressures, due to the contraction of the temperature difference between the heat exchanging streams in the pre-cooler. It can be concluded that with the utilisation of ammonia as a refrigerant, the optimum liquefaction pressure for the minimisation of total work duty is 45 bar.

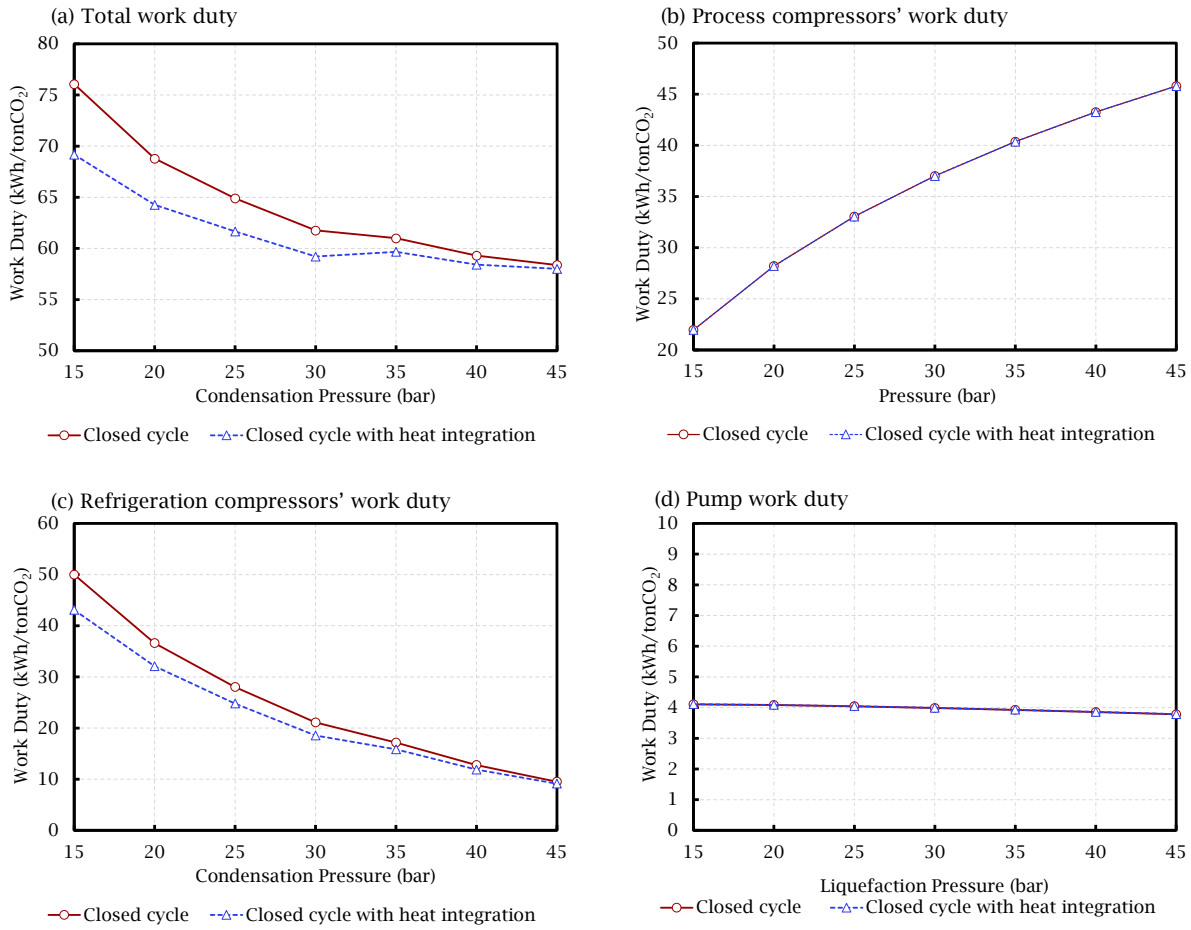

Figure 3.6: The effect of liquefaction pressure on work duty for Case 2b and 2c. This is presented for an optimum number of compressors, optimum compressor ratio, and interstage cooling of 35˚C, and a 10-inch pipeline diameter.

3.4.4 Development of alternative process schemes

3.4.4.1 Areas of improvement and alternative process schemes

Analyses have identified intercooling temperature as a key energy consumption driver across the process schemes. Additionally, subcritical liquefaction and pumping schemes show that pumping has the least sensitivity towards the liquefaction pressure. The study further considers the use of seawater as a cooling utility in both process scheme categories. Here, seawater temperatures of 5˚C and 20˚C are explored, as these are typical North Sea temperatures.

Although seawater could lead to significant heat exchanger fouling, it presents significant process scheme alternatives for CO_2 conditioning. For the gas compression route, seawater would be utilised to cool the captured stream in interstage heat exchangers. In the subcritical liquefaction and pumping schemes,

seawater would be utilised as both a cooling and condensing utility. This would, therefore, eliminate the need for the ammonia refrigeration cycle. While maintaining a heat exchanger approach of 5˚C across the condenser, the captured CO_2 would, respectively, condense at 45 bar and 65 bar at seawater temperatures of 5˚C and 20˚C. The two alternative process schemes are presented in Figure 3.7.

(a) Case 1b: Gas compression with seawater cooling

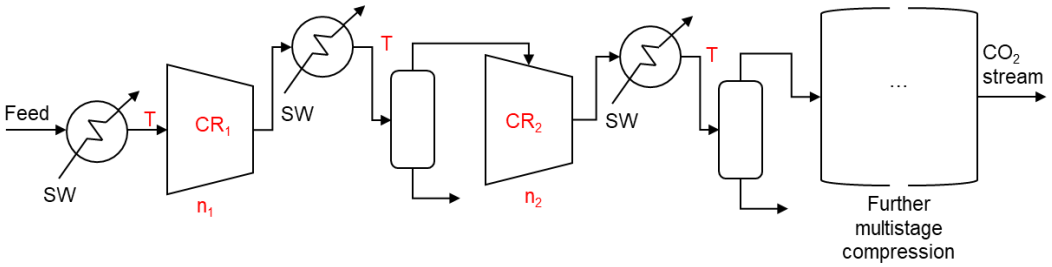

(b) Seawater subcritical liquefaction and pumping

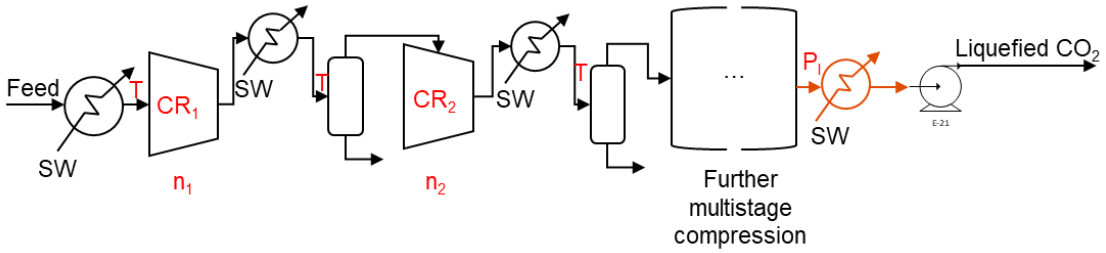

Figure 3.7: Alternative process schemes for the conditioning of the captured CO_2 stream, utilising seawater (SW).

3.4.5 Summary of electricity consumption across a selection of pipeline diameters

Figure 3.8 summarises the optimisation results for the base case and alternative process schemes at a selection of pipeline diameters.

Consistent with Figure 3.3, the work duty of the process schemes declines with larger pipeline diameters, as a lower pipeline inlet pressure is required. Figure 3.8 further highlights that the optimum number of compressor stages (as per definition in section 3.3.3) remains the same for each process scheme across the selected pipeline diameters.

For base cases utilising cooling water, the choice of process scheme is driven by capital and operating costs trade-offs. Figure 3.8 (a) indicates that the gas compression process scheme has the lowest work duty relative to the subcritical liquefaction and pumping process schemes. However, the gas compression pathway

requires five more process compression stages to attain this work duty saving relative to the subcritical liquefaction and pumping process. This is since for the latter schemes, the pressurisation work is shifted away from the compression circuit to the pump. It should be noted that, in addition, the subcritical liquefaction and pumping route will require two compression stages as part of the refrigeration cycle.

Figure 3.8 demonstrates that when cooling water temperatures above 30 °C are used, the gas compression process has the lower work duty, while for cooling water temperatures below 20 °C, the subcritical liquefaction and pumping process is the most energy efficient. Furthermore, the utilisation of seawater instead of 30 °C cooling water leads to significant total work duty savings for both pressurisation pathways. In these cases, seawater is used as both a cooling utility in interstage compression heat exchangers and also as a liquefaction utility for the captured CO_2 stream for subcritical liquefaction and pumping process schemes. Figure 3.8 illustrates that, with gas compression with cooling water at 30 °C as a basis, a work duty saving of up to 10.2% is attainable for a case utilising seawater at a temperature of 5 °C, whilst still maintaining the same number of optimum compression stages. Additionally, for the subcritical liquefaction and pumping pathway, a 27.0% work duty saving is possible with the utilisation of seawater at 5 °C relative to 30 °C. In this instance, it was found that the addition of compression stages significantly increased overall work duty, leading to this process scheme requiring 5 process compression stages, relative to 3 that are required for the scheme utilising cooling water at 30 °C.

Figure 3.8 illustrates that, based on seawater availability, cooling with an accessible utility below 20°C and its utilisation to liquefy the captured CO_2 stream culminates in the least work duty requirement. Furthermore, a shift from a 10 to 14-inch pipeline offers significant work duty savings only for cases utilising cooling water as a primary utility, where duty savings of up to 3.1% can be attained, while a minimal work duty saving can be realised for an 18-inch pipeline diameter at the nameplate capacity of 1 $MtCO_2$/y.

	Process configuration	Work Duty (kWh/tonCO_2) Inner Pipeline Diameter (inches) 10	14	18	Number of compression stages (CO_2 / Ammonia Refrigeration)
Cooling water (30°C)	Gas compression	57.4	55.4	55.5	8
	Closed cycle liquefaction	59.1	58.1	57.8	3 / 2
	Closed cycle liquefaction with heat integration	58.7	57.3	56.9	3 / 2
Seawater (20°C/5°C)	Gas compression (20°C)	54.8	54.5	53.3	8
	Gas compression (5°C)	51.5	50.7	49.8	8
	Seawater cooling, liquefaction and pumping (20°C)	52.1	50.8	50.4	5
	Seawater cooling, liquefaction and pumping (5°C)	42.8	41.8	41.5	5

Figure 3.8: Process configurations' optimised work duty (kWh/CO_2) and number of compression stages at selected pipeline diameters for a capacity of 1 $MtCO_2$/y.

3.5 Work duty variation with pipeline mass flow rate

New pipeline development across the CCUS value chain requires that a return is maximised from the capital outlay of pipeline and conditioning development through the sharing of pipeline transportation capacity. Figure 3.9 and Figure 3.10, respectively, present the work duty for process schemes utilising cooling water and seawater for scenarios where the pipeline mass flow rate should rise from the nameplate capacity of 1 $MtCO_2$/y. The work duties for all pipeline mass flow rate scenarios are computed based on the optimised number of compression stages as presented in Figure 3.8. Therefore, the change in work duty is only due to changes in the required pipeline inlet pressure (see Figure 3.3). In pipeline modelling, it was found that a 10-inch inner diameter pipeline would result in significant pressure drop for a mass flow rate of 5 $MtCO_2$/y, hence the energy requirements for this scenario were not considered. Across all pipeline mass flow rate scenarios, the subcritical liquefaction and pumping of CO_2 with seawater at 5 °C leads to the least work duty.

The work duty sensitivities to a step-up in pipeline mass flow rate varies across the optimised process schemes and the selected pipeline diameters. At greater pipeline flow rates, larger pipeline diameters cushion the rise in work duty across all process scheme cases. For instance, a step-up in pipeline flow rate from 1 $MtCO_2$/y to 5 $MtCO_2$/y for a 14-inch and 18-inch pipeline, requires 20.1% and 8.1% rise in work duty,

respectively. Additionally, the temperature of the cooling/liquefying utility is critical in limiting the rise in work duty, with cases utilising cooling water displaying the greatest sensitivity to changes in the pipeline mass flow rate.

The difference between subcritical liquefaction and pumping and conventional gas compression declines as pipeline inlet pressures rise far above the critical point of CO_2. This is illustrated by Figure 3.10 (a) and (c) for a 14-inch inner diameter pipeline with a mass flow rate of 5 $MtCO_2/y$. Here the required pipeline inlet pressure is ca. 230 barg (see Figure 3.3) and at these conditions, CO_2 exhibits similar properties to CO_2 in the liquid phase [6]. Therefore, at these conditions, the majority of the pressurisation work occurs at these high pressures, with downstream compressor(s) and pump(s) having an insignificant work duty difference at these supercritical conditions.

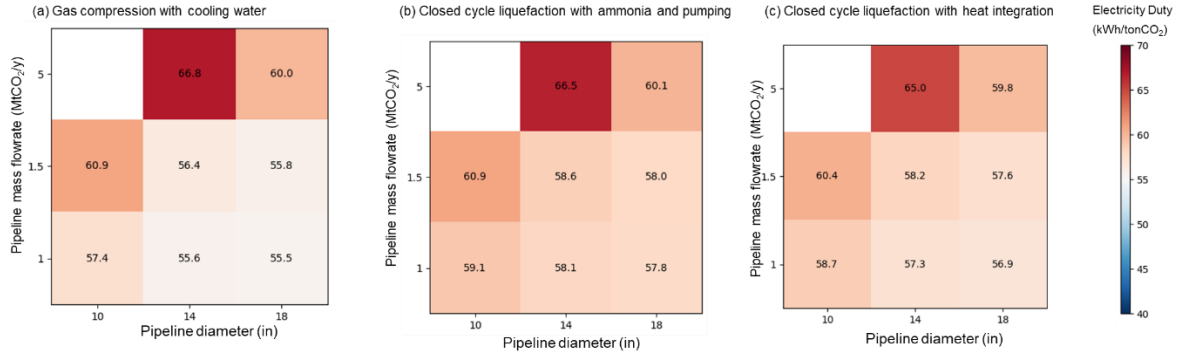

Figure 3.9: Effect of mass flow rates on overall work duty for cases utilising cooling water available at 30˚C at a selection of pipeline diameters. The number of compression stages are optimised for a nameplate capacity of 1 $MtCO_2/y$ and for a final stream delivery of 100 barg.

Figure 3.9 and Figure 3.10, further indicate that the liquefaction of CO_2 with seawater culminates to the least work duty sensitivity with varying pipeline mass flow rate. Figure 3.10 (d) and Figure 3.9 (c) demonstrate that a 14-inch pipeline a 17.5% and a 37.4% rise in work duty, respectively, is required for a pipeline step-up from 1 $MtCO_2/y$ to 5 $MtCO_2/y$. This work duty sensitivity with pipeline mass flow rate has differing implications for each of the process schemes, as additional process units may be required, such as greater interstage cooling capacity due to the higher compression ratios. The subcritical and pumping pathway offers a significant advantage to conventional gas compression, as alterations to the process scheme would only be required downstream of the pump.

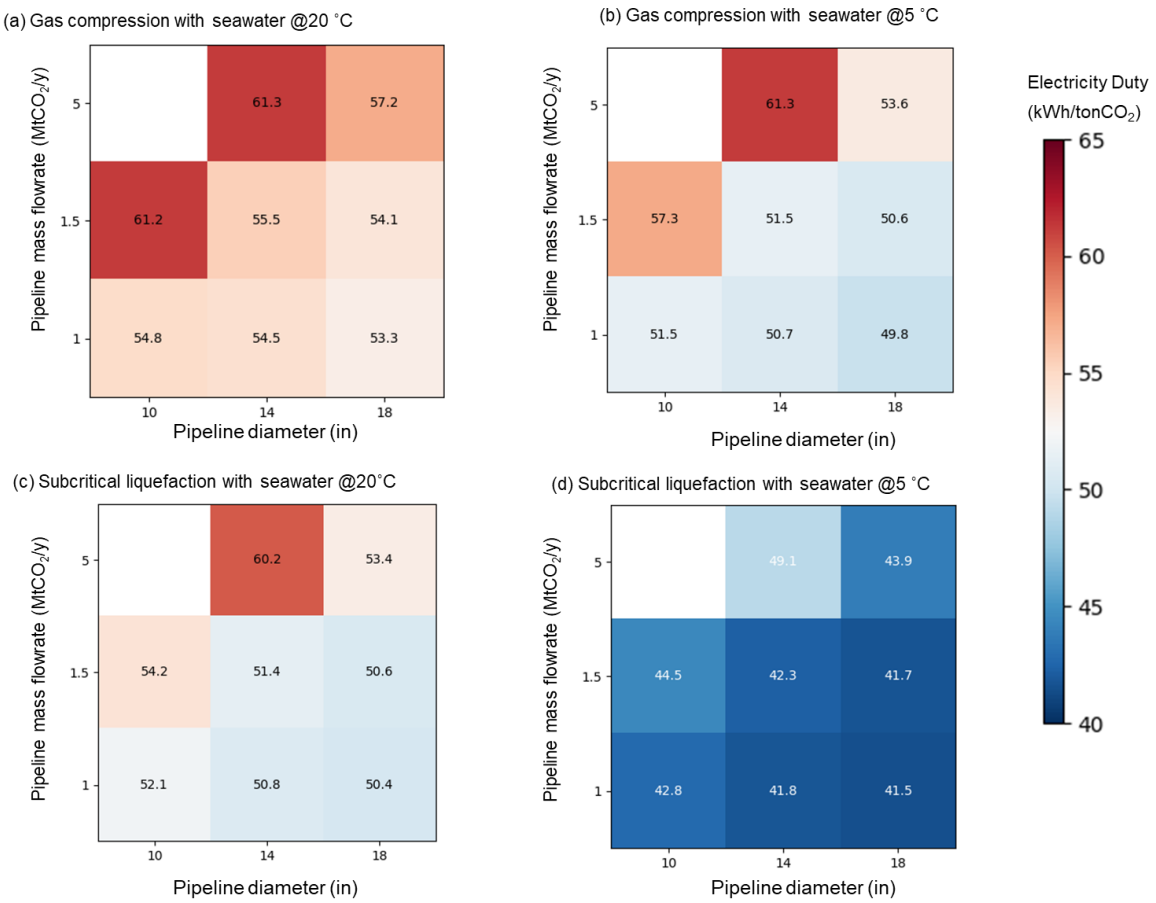

Figure 3.10: Effect of mass flow rates on overall work duty for cases utilising seawater at a selection of pipeline diameters. The number of compression stages are optimised for a nameplate capacity of 1 $MtCO_2/y$ and a final stream delivery of 100 barg.

3.6 Conclusions

This study provides a comprehensive comparison and optimisation of two CO_2 pressurisation pathways for pipeline transport: gas compression and subcritical liquefaction and pumping. In all cases, the effect of the number of compressor stages, compression ratio, interstage cooling temperature, and the liquefaction pressure (for subcritical liquefaction and pumping cases) were investigated for a conditioning capacity of 1.0 $MtCO_2/y$ and a variability in pipeline mass flow rate.

The process pathway with the least work duty is largely driven by the temperature of cooling water. In cases that use cooling water above a temperature of 30°C, there exists a trade-off between additional compression stages and the overall work duty. At these conditions, the gas compression process is found to have a lower work duty, while requiring more compression stages relative to the subcritical liquefaction and pumping of CO_2. The use of a cold utility, such as seawater, culminates in significant

reductions in the overall work duty across both pathways. The use of seawater at 5°C in the compressor interstage cooling and the liquefaction of CO_2 is found to reduce the work duty requirements by 25.4% and requires fewer compression stages relative to the gas compression pathway using cooling water at 30°C. Across all process pathways, the optimisation of the compression ratio across stages was also shown to minimise work duty, especially in cases with a low number of compression stages.

This study has also shown that the subcritical liquefaction and pumping pathway has the least work duty sensitivity to variabilities in pipeline mass flow rate, with this sensitivity declining as a colder utility is employed. Furthermore, an increase in work duty requirements with rising pipeline mass flow rates, can be further cushioned through the utilisation of large-diameter pipelines, though this would need to be evaluated against additional capital requirements. Consequently, as the CCUS value chain develops, the subcritical liquefaction and pumping of CO_2 offers energy and capital cost savings in cases where future pipeline mass flow rate is variable or uncertain, and in contexts where installation of booster compressors along the pipeline is limited, such as in offshore pipelines.

Acknowledgements

This project has received funding from the 3D Project – a project under the European Union's Horizon 2020 research and innovation programme under Grant Agreement No 838931, and from the Technical University of Denmark in the form of a PhD Scholarship.

References

[1] M.E. Boot-Handford, J.C. Abanades, E.J. Anthony, M.J. Blunt, S. Brandani, N. Mac Dowell, J.R. Fernández, M.-C. Ferrari, R. Gross, J.P. Hallett, R.S. Haszeldine, P. Heptonstall, A. Lyngfelt, Z. Makuch, E. Mangano, R.T.J. Porter, M. Pourkashanian, G.T. Rochelle, N. Shah, J.G. Yao, P.S. Fennell, Carbon capture and storage update, Energy Environ. Sci. 7 (2014). https://doi.org/10.1039/C3EE42350F.

[2] M.K. Chandel, L.F. Pratson, E. Williams, Potential economies of scale in CO2 transport through use of a trunk pipeline, Energy Convers Manag 51 (2010). https://doi.org/10.1016/j.enconman.2010.06.020.

[3] E. Mechleri, S. Brown, P.S. Fennell, N. mac Dowell, CO 2 capture and storage (CCS) cost reduction via infrastructure right-sizing, Chemical Engineering Research and Design 119 (2017). https://doi.org/10.1016/j.cherd.2017.01.016.

[4] A. Brunsvold, J.P. Jakobsen, J. Husebye, A. Kalinin, Case studies on CO2 transport infrastructure: Optimization of pipeline network, effect of ownership, and political incentives, Energy Procedia 4 (2011) 3024–3031. https://doi.org/10.1016/j.egypro.2011.02.213.

[5] N. Ghazi, J.M. Race, Techno-Economic Modelling and Analysis of CO2 Pipelines, in: Volume 1: Upstream Pipelines; Project Management; Design and Construction; Environment; Facilities Integrity Management; Operations and Maintenance; Pipeline Automation and Measurement, American Society of Mechanical Engineers, 2012. https://doi.org/10.1115/IPC2012-90455.

[6] L.M. Romeo, I. Bolea, Y. Lara, J.M. Escosa, Optimization of intercooling compression in CO2 capture systems, Appl Therm Eng 29 (2009). https://doi.org/10.1016/j.applthermaleng.2008.08.010.

[7] L.M. Romeo, P. Lisbona, Y. Lara, Combined carbon capture cycles: An opportunity for size and energy penalty reduction, International Journal of Greenhouse Gas Control 88 (2019) 290–298. https://doi.org/10.1016/j.ijggc.2019.06.023.

[8] Z.X. Zhang, G.X. Wang, P. Massarotto, V. Rudolph, Optimization of pipeline transport for CO2 sequestration, Energy Convers Manag 47 (2006). https://doi.org/10.1016/j.enconman.2005.06.001.

[9] S.P. Peletiri, I.M. Mujtaba, N. Rahmanian, Process simulation of impurity impacts on CO2 fluids flowing in pipelines, J Clean Prod 240 (2019) 118145. https://doi.org/10.1016/j.jclepro.2019.118145.

[10] S. Martynov, N. mac Dowell, S. Brown, H. Mahgerefteh, Assessment of Integral Thermo-Hydraulic Models for Pipeline Transportation of Dense-Phase and Supercritical CO_2, Ind Eng Chem Res 54 (2015). https://doi.org/10.1021/acs.iecr.5b00851.

[11] D.-Y. Peng, D.B. Robinson, A New Two-Constant Equation of State, Industrial & Engineering Chemistry Fundamentals 15 (1976) 59–64. https://doi.org/10.1021/i160057a011.

[12] M. Mazzoccoli, B. Bosio, E. Arato, S. Brandani, Comparison of equations-of-state with P–ρ–T experimental data of binary mixtures rich in CO2 under the conditions of pipeline transport, J Supercrit Fluids 95 (2014) 474–490. https://doi.org/10.1016/j.supflu.2014.09.047.

[13] A.G. Perez, C. Coquelet, P. Paricaud, A. Chapoy, Comparative study of vapour-liquid equilibrium and density modelling of mixtures related to carbon capture and storage with the SRK, PR, PC-SAFT and SAFT-VR Mie equations of state for industrial uses, Fluid Phase Equilib 440 (2017) 19–35. https://doi.org/10.1016/j.fluid.2017.02.018.

[14] S.M. Hall, Rules of Thumb for Chemical Engineers, Elsevier, 2018. https://doi.org/10.1016/C2016-0-00182-1.

[15] S.B. Martynov, N.K. Daud, H. Mahgerefteh, S. Brown, R.T.J. Porter, Impact of stream impurities on compressor power requirements for CO 2 pipeline transportation, International Journal of Greenhouse Gas Control 54 (2016). https://doi.org/10.1016/j.ijggc.2016.08.010.

[16] S. Jackson, E. Brodal, Optimization of the Energy Consumption of a Carbon Capture and Sequestration Related Carbon Dioxide Compression Processes, Energies (Basel) 12 (2019). https://doi.org/10.3390/en12091603.

4 Modelling Phase Equilibria of Sulphur Compounds in Mixtures Relevant to Carbon Capture and Storage with New Association Schemes

Abstract

This study models the phase equilibria of the sulphur compounds – SO_2, H_2S, and COS – in mixtures relevant to carbon capture and storage (CCS). The modelling tool used is the cubic plus association (CPA) equation of state. Modelling of binary and multicomponent mixtures of these sulphur compounds with CO_2, water, glycols, methane, and other inert compounds is performed. In the modelling approach, sulphur compounds are treated as inert or cross-associating (solvating) compounds with multiple association sites, culminating in the proposal of new association schemes. Throughout the study, the predictive and correlative performance of CPA is assessed. It has been found that the allocating of association sites for the sulphur compounds leads to improved modelling of phase equilibria behaviour. Further analysis against multicomponent systems will need to be performed to conclude on the appropriate association schemes for these compounds.

4.1 Introduction

Carbon capture and storage (CCS) is a long value chain, involving the capture of carbon dioxide (CO_2) typically from industrial point sources, the transport of this stream, and concludes with its storage or utilisation. Throughout this value chain, CO_2 coexists with impurities that originate from various sources [1]. These impurities play a significant role in influencing the properties of the captured CO_2 stream across the segments of the CCS value chain. For instance, the presence of water during the transport of the captured CO_2 may lead to the corrosion of pipeline transport infrastructure [2]. The presence of impurities has culminated in strict specifications of the captured CO_2 stream across the CCS value chain. Therefore, impurities need to be removed before the capture process, or in post-capture polishing.

A common class of impurities are sulphur compounds such as sulphur dioxide (SO_2), hydrogen sulphide (H_2S), and carbonyl sulphide (COS). These compounds have a wide range of sources and are commonly present in natural gas and petroleum processing. They are formed through the complete or partial oxidation of hydrocarbon fuels, such as coal and biomass, and as side products from industrial processes such as the

Claus reaction [1,3]. Furthermore, in the presence of water, H_2S can be formed through the hydrolysis of COS or CS_2.

In industrial processes, sulphur compounds interact with solvents, and other components commonly associated with CO_2. One of these is the glycol series: mono-ethylene glycol (MEG), diethylene glycol (DEG), and triethylene glycol (TEG), which are employed as stripping agents primarily in the dehydration of process streams. Therefore, understanding the phase equilibria of mixtures containing these sulphur compounds systems and other components, besides CO_2, is vital in the design of processes across the entire CCS value chain.

In the open literature, two main approaches have been taken in the modelling of phase equilibria of mixtures containing sulphur compounds. The first approach involves the treatment of this class of impurities with the use of classical cubic equations of state to model the phase equilibria of these systems [4]. This approach relies heavily on binary interaction coefficients to correlate binary experimental data. A more recent approach has been to recognise that these components can have significant self-association interactions, and also can cross-associate with other compounds. Tsivintzelis and co-workers [5], explored the modelling of H_2S with association sites by employing the Cubic Plus Association equation of state (CPA EoS). SO_2 has also been modelled to solvate in water, by allocating it electron acceptor cross-associating sites via the PC-SAFT model [6]. In both cases, association has been found to yield good agreement with experimental phase equilibria data for binary and multicomponent systems. However, in the previous work, a limited number of association schemes are considered, and the performance of this modelling approach is not evaluated with potential impurities within the CCS value chain.

This work aims to systematically model phase equilibrium in mixtures containing sulphur compounds, evaluating the necessity of accounting for association and solvation for relevant pure components and mixtures within the CCS value chain. The tool that has been chosen to perform this analysis, is the CPA equation of state, which allows for the explicit allocation of association sites. Section I of this work gives the formulation of the CPA equation of state, its extension to mixtures and its utilisation in modelling sulphur-containing systems. Section II presents the association schemes considered for the modelling of sulphur-containing compounds, the modelling approach, and pure component parameters computed in this work. This is then followed by Part III and IV, which presents the results of modelling binary and

multicomponent systems. The modelling in these cases, is performed with both associating and non-associating compounds.

4.2 CPA equation of state and mixing rules

4.2.1 Pure components

The CPA model was developed by Kontogeorgis and co-workers [7,8] and consists of two contributions - the physical interactions and association terms. The physical term is represented by the Soave-Redlich-Kwong (SRK) equation of state, and the association contribution is derived from Wertheim's theory [9–12], which accounts for specific site-to-site interactions. This equation is outlined in detail in other studies [13,14], with a summary provided here. The CPA equation of state can be expressed as in equation (4.1).

$$P = \frac{RT}{V_m - b} - \frac{\alpha(T)}{V_m(V_m + b)} - \frac{1}{2}\frac{RT}{V_m}\left(1 + \rho\frac{\partial \ln g}{\partial \rho}\right)\sum_i x_i \sum_{A_i}\left(1 - X_{A_i}\right) \tag{4.1}$$

The key term in the CPA equation is X_{A_i} which describes the fraction of sites A in compound i not bonded to other active sites. x_i is the mole fraction of component i. X_{A_i} is expressed in equation (4.2).

$$X_{A_i} = \frac{1}{1 + \left(\frac{1}{V_m}\right)\sum_j x_j \sum_{B_j} X_{B_j}\Delta^{A_iB_j}} \tag{4.2}$$

In equation (4.2), the term $\Delta^{A_iB_j}$ is the association strength between site A of molecule i, and site B of molecule j. The association strength is expressed in (4.3).

$$\Delta^{A_iB_j} = g(\rho)\left(\exp\left(\frac{\varepsilon^{A_iB_j}}{RT}\right) - 1\right) b_{ij}\beta^{A_iB_j} \tag{4.3}$$

Where $g(\rho)$ is the radial distribution function,

$$g(\rho) = \frac{1}{1 - 1.9\eta}, \eta = \frac{1}{4}b\rho \tag{4.4}$$

In equation (4.3), $\varepsilon^{A_iB_j}$ and $\beta^{A_iB_j}$ are respectively, the association energy, and volume of interaction between site A of molecule i and site B of molecule j.

In equation (4.1), $\alpha(T)$ is the attractive energy parameter from the SRK equation of state, shown in equation (4.5). Here T_r is the reduced temperature, expressed as $T_r = \frac{T}{T_c}$, and T_c being the critical temperature of that compound.

$$\alpha(T) = a_0\left(1 + c_1\left(1 - \sqrt{T_r}\right)\right)^2 \tag{4.5}$$

For pure compounds, CPA requires the specification of five parameters. Three parameters from the non-associating SRK part, which are a_0, b and c_1 , and two parameters to be specified only for self-associating components – association energy, $\varepsilon^{A_iB_j}$, and association volume, $\beta^{A_iB_j}$. In this work, a_0, is reported as the reduced energy parameter, $\Gamma = \frac{a_0}{Rb}$.

4.2.2 Extension of CPA to mixtures

The extension of the CPA model to mixtures requires the use of mixing and combining rules. The classical van der Waals one-fluid rules are employed as mixing and combining rules for the SRK part of CPA.

$$\alpha = \sum_i \sum_j x_i x_j \alpha_{ij} \tag{4.6}$$

$$b = \sum_i \sum_j x_i x_j b_{ij} \tag{4.7}$$

Where α_{ij} and b_{ij} are determined as:

$$\alpha_{ij} = \sqrt{\alpha_i \alpha_j}\left(1 - k_{ij}\right) \tag{4.8}$$

$$b_{ij} = \frac{b_i + b_j}{2} \tag{4.9}$$

The k_{ij} parameter is usually determined from binary data, and hence its specification is optional. In the latter case, only pure component parameters are utilised to predict binary or multicomponent phase equilibria.

For cross-associating systems, where both components are self-associating, the cross-associating energy and cross-associating volume can be determined through the CR-1 rule.

$$\varepsilon^{A_iB_j} = \frac{\varepsilon^{A_iB_i} + \varepsilon^{A_jB_j}}{2} \tag{4.10}$$

$$\beta^{A_iB_j} = \sqrt{\beta^{A_iB_i}\,\beta^{A_jB_j}} \tag{4.11}$$

The CPA equation of state can be further extended to systems in which one of the components does not self-associate, however, they interact with associating compounds. To account for association in such systems, the modified CR-1 (mCR-1) combining rule allows for the fitting of the cross-associating volume using binary component data. The cross-association energy between the two compounds is

determined from the self-associating compound, as shown in equation (4.12), while the cross-associating volume is fitted to binary data.

$$\varepsilon^{A_iB_j} = \frac{\varepsilon_{associating}}{2} \tag{4.12}$$

$$\beta^{A_iB_j} = \beta^{fit}_{cross-association} \tag{4.13}$$

The mCR-1 combining rule has been successfully demonstrated to be effective in reproducing data of solvating systems, such as CO_2-Water [15], and other systems [16].

4.3 Modelling approach, pure compounds and mixtures parameter estimation

In this section association schemes for SO_2, H_2S, and COS are proposed. For each of the association schemes, CPA pure component parameters are determined from liquid density and saturation pressure data. The modelling is then extended to binary and ternary mixtures.

4.3.1 Association Schemes

Four association schemes are considered for the modelling of SO_2. These association schemes are shown in Figure 4.1.

The first scheme considers the solvation of SO_2 in the presence of other associating compounds. This could occur on either of the oxygen lone pairs. The second scheme treats the oxygen lone pairs as negative sites, while the sulphur is treated as a positive site. This is since oxygen has a higher electron affinity, relative to sulphur, hence, the sulphur is slightly positive. The third scheme considers the sulphur and both the oxygens as bipolar sites (bp), and the remaining oxygen lone pairs as electron donor (ed) sites. It should be noted that bipolar sites can interact with both electron donor and electron acceptor (ea) sites. The fourth and fifth association schemes consider sulphur as a positive site, and the oxygen lone pairs as negative sites.

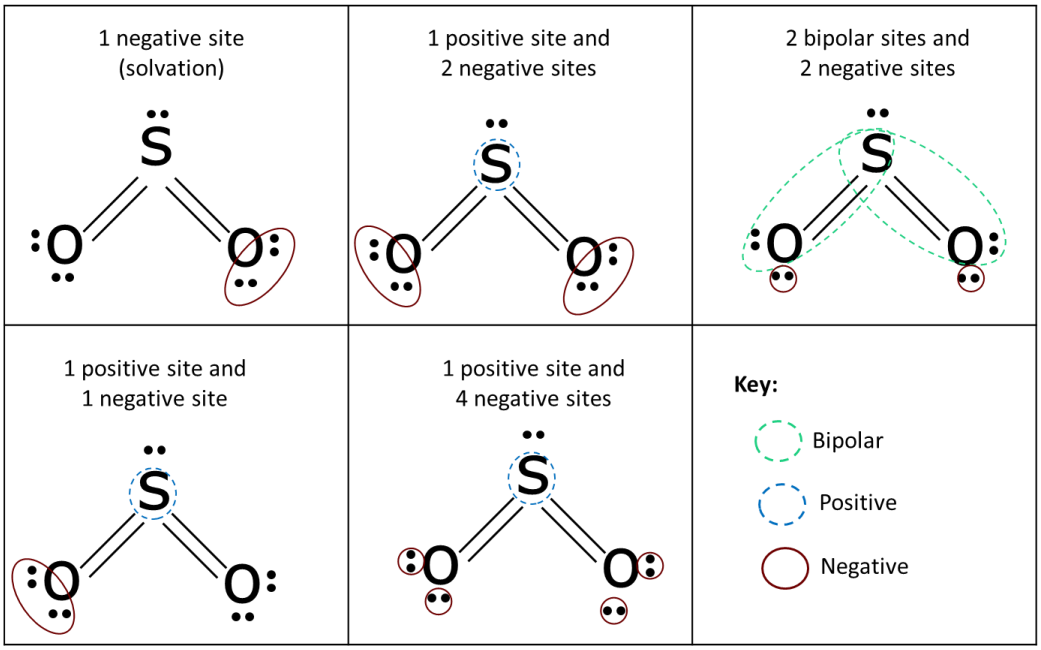

Figure 4.1: Proposed SO_2 association schemes.

Though COS is a linear molecule, it is polar, which is due to the strong electron affinity of oxygen and sulphur relative to carbon. Consequently, the net dipole is towards the oxygen. Figure 4.2 highlights the six association schemes considered for COS. Similar association schemes as those of SO_2 have been identified. The main exception is the last association scheme, which considers the carbon and sulphur as electron acceptor sites, with the oxygen lone pairs considered as electron donor sites. This is largely driven by the molecule's net dipole being in the direction of the oxygen.

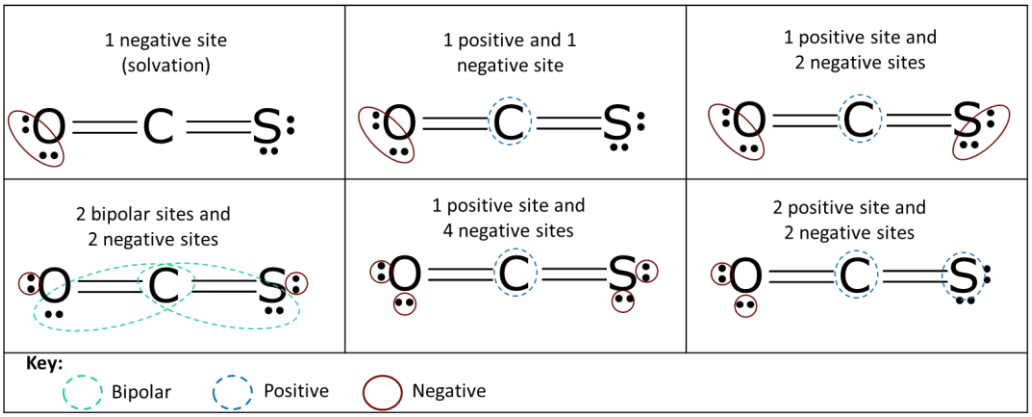

Figure 4.2: Proposed COS association schemes.

A detailed evaluation of H_2S association schemes has been undertaken by Tsivintzelis and co-workers [17], where H_2S is treated to have multiple association schemes: 2B (1ea-1ed), 3B (1ea-2ed), and 4C (2ea-2ed). This work considers these association

schemes, and additional schemes, which treat H_2S with 2ea-1ed sites or 2bp sites. The 2ea-1ed scheme considers each of the sulphur lone pairs to be negative sites, with either of the hydrogens as positive sites. Similar to COS, bipolar sites are also considered, between the lone electron and hydrogen atoms. All the H_2S association schemes considered in this work are shown in Figure 4.3.

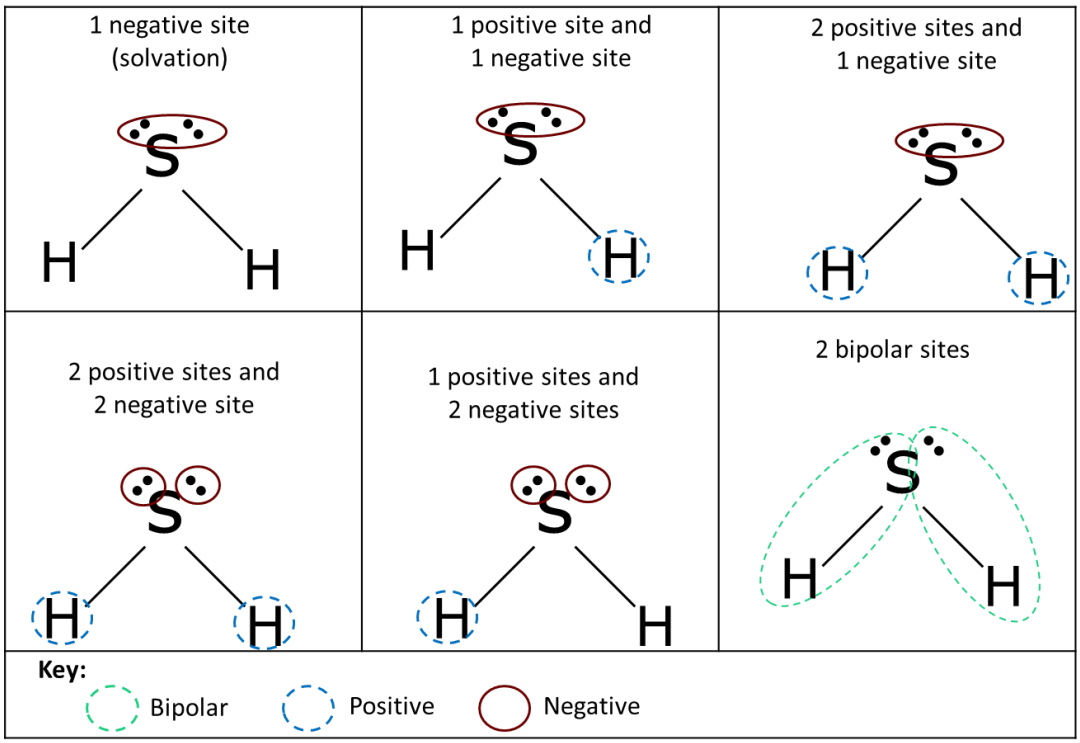

Figure 4.3: Proposed H_2S association schemes.

4.3.2 Pure components and mixtures parameter estimation

The CPA equation of state requires the specification of five pure component parameters. To obtain these parameters for SO_2, H_2S, and COS, the CPA is regressed to experimental saturation pressure and liquid density data for each compound's association schemes. To perform this regression, the DIPPRR database [18] was utilised to obtain pure component experimental data. The pure component parameters were fitted to minimise the objective function in equation (4.14), for data within the temperature range – $0.5T_c \leq T \leq 0.9T_c$. CPA pure component parameters for other compounds were obtained from literature.

$$OF_{min}(b, \Gamma, c_1, \varepsilon, \beta) = \sum_{i=1}^{N} \left(\frac{P^{sat,exp} - P^{sat,calc}}{P^{sat,exp}} \right)^2 + \sum_{i=1}^{N} \left(\frac{\rho_{liq}^{exp} - \rho_{liq}^{calc}}{\rho_{liq}^{exp}} \right)^2 \quad (4.14)$$

The performance of the CPA model is evaluated against experimental data by computing the average absolute deviation (AAD), shown in equation (4.15). Here X is the output of interest and n is the number of experimental data points.

$$\%AAD = \frac{1}{n}\sum_{i=1}^{n}\left|\frac{X^{calc} - X^{exp}}{X^{exp}}\right| \cdot 100 \qquad (4.15)$$

Table 4.1 – 4.3 presents the CPA parameters and deviations from experimental data for SO_2, COS, and H_2S, respectively, across the considered association schemes. In all cases, the CPA model is in satisfactory agreement with experimental saturation pressure and liquid density data. Taking into account self-association leads to a slight improvement in the minimisation of AAD, relative to cases that consider the components as non-associating. Table 4.4 consolidates the pure component parameters obtained from open literature. These pure component parameters are used to model the phase equilibria of binary and ternary mixtures.

Table 4.1: SO_2 Pure component parameters determined in this work. Abbreviations: n.a.- non-associating, bp-bipolar, ea-electron acceptor, and ed-electron.

Scheme	**b (cm^3/mol)**	**$\Gamma = \frac{a_0}{Rb}$ [K]**	**c_1**	**β x 1000**	**$\frac{\varepsilon}{R}$[K]**	**%AAD in P^{sat}**	**% AAD in ρ_{liq}**
n.a	35.18	2182.53	0.8379	-	-	0.48	0.69
1ea-2ed	35.66	2088.03	0.8181	35.70	446.67	0.45	0.58
2bp-2ed	35.69	2089.86	0.8203	14.15	388.13	0.45	0.58
1ea-1ed	35.63	2083.57	0.8167	62.69	507.38	0.44	0.58
1ea-4ed	35.67	2090.35	0.8185	18.87	420.44	0.45	0.58

Table 4.2: COS Pure component parameters determined in this work. Abbreviations: n.a.- non-associating, bp-bipolar, ed-electron donor, ea-electron acceptor.

Scheme	b (cm^3/mol)	$\Gamma = \frac{a_0}{Rb}$ [K]	c_1	β x 1000	$\frac{\varepsilon}{R}$[K]	%AAD in P^{sat}	% AAD in ρ_{liq}
n.a	40.51	1915.98	0.58801	-	-	0.24	0.71
1ea-2ed	41.00	1846.01	0.5684	39.80	323.24	0.19	0.69
2bp-2ed	41.04	1845.24	0.5690	15.53	288.30	0.18	0.69
1ea-1ed	40.96	1845.80	0.5675	68.64	363.34	0.19	0.69
1ea-4ed	41.02	1846.03	0.5685	21.30	305.96	0.19	0.69
2ea-2ed	41.05	1845.07	0.5694	24.49	277.37	0.18	0.69

Table 4.3: H_2S Pure component parameters determined in this work. Abbreviations: n.a.- non-associating, bp-bipolar, ed-electron, ea-electron acceptor.

Scheme	b (cm^3/mol)	$\Gamma = \frac{a_0}{Rb}$ [K]	c_1	β x 1000	$\frac{\varepsilon}{R}$[K]	%AAD in P^{sat}	% AAD in ρ_{liq}
n.a	28.64	1861.48	0.6199	-	-	1.11	1.03
1ea-1ed	28.46	1404.90	0.5336	144.59	847.46	1.16	0.64
2ea-1ed	29.17	1648.79	0.5926	85.03	437.52	1.14	0.69
2ea-2ed	29.32	1674.41	0.5979	57.24	314.92	1.14	0.70
1ea-2ed	29.17	1648.71	0.5927	85.17	437.20	1.14	0.69
2bp	28.46	1404.40	0.5336	72.35	847.84	1.16	0.64

Table 4.4: Pure component parameters of compounds utilised in this study. Abbreviations: n.a.- non-associating, bp-bipolar, ed-electron, ea-electron acceptor.

Component	Scheme	b [cm³/mol]	$\Gamma = \frac{a_0}{Rb}$ [K]	c_1	β x 1000	$\frac{\varepsilon}{R}$ [K]	References
CO_2	n.a	27.2	1551.11	0.7602	-	-	[19]
Water	2ea-2ed	14.5	1017.34	0.6736	69.2	2003.25	[20]
Ethylene Glycol (MEG)	2ea-2ed	51.4	2531.71	0.6744	14.1	2375.75	[21]
Diethylene glycol (DEG)	2ea-2ed	92.1	3448.8	0.7991	6.4	2367.44	[21]
Triethylene glycol (TEG)	2ea-2ed	132.1	3562.28	1.1692	18.8	1724.34	[21]
O_2	n.a	21.7	774.70	0.4758	21.7		This work

Five approaches were adopted for the modelling of binary and ternary phase equilibria data with CPA, which are shown in Table 4.5. For some binary systems, the predictive capabilities of the CPA model were assessed. In such cases, modelling was performed without a binary interaction parameter (kij=0), while in other cases kij was adjustable. The adjustable kij was determined from regressing the CPA model to binary phase equilibria experimental data. For cases where component solvation is considered (approach B), the mCR-1 combining rule was utilised to obtain cross-association energy, while the cross-associating volume was fitted to binary phase equilibria data (see equations (4.12) and (4.13)). This culminates in an additional regression parameter for modelling approaches that consider solvation, as shown in Table 4.5.

Table 4.5: Modelling approaches for binary and ternary systems.

Method	Sulphur compound association scheme	Association in other compounds	ε_{cross}	β_{cross}	Binary interaction parameters [k_{ij}]
A1	non-associating	self-associating or non-associating			adjustable
A2	non-associating	self-associating or non-associating			not adjustable
B1	1 negative site	self-associating	mCR-1 rule	adjustable	adjustable
B2	1 negative site	self-associating	mCR-1 rule	adjustable	not adjustable
C1	self-associating	self-associating or non-associating	CR-1 rule	CR-1 rule	adjustable
C2	self-associating	self-associating or non-associating	CR-1 rule	CR-1 rule	not adjustable

4.4 Phase behaviour of mixtures with sulphur compounds

4.4.1 Binary mixtures with SO_2

4.4.1.1 SO_2-water

The solubility of SO_2 in water was predicted ($kij = 0$) over the 298 K to 393 K temperature range, shown in Figure 4.4. When SO_2 is modelled as non-associating, the solubility of SO_2 in water is underpredicted, resulting in the highest deviation from experimental data, as presented in Table 4.6. By allocating association sites to SO_2, the solubility predictions are improved. In particular, the treatment of SO_2 with 1 ed

(solvating) or 1ed-1ea associating sites, culminates in a strong agreement with experimental data across the temperature range. These association schemes each have an AAD in pressure below 9%, as shown in Table 4.6.

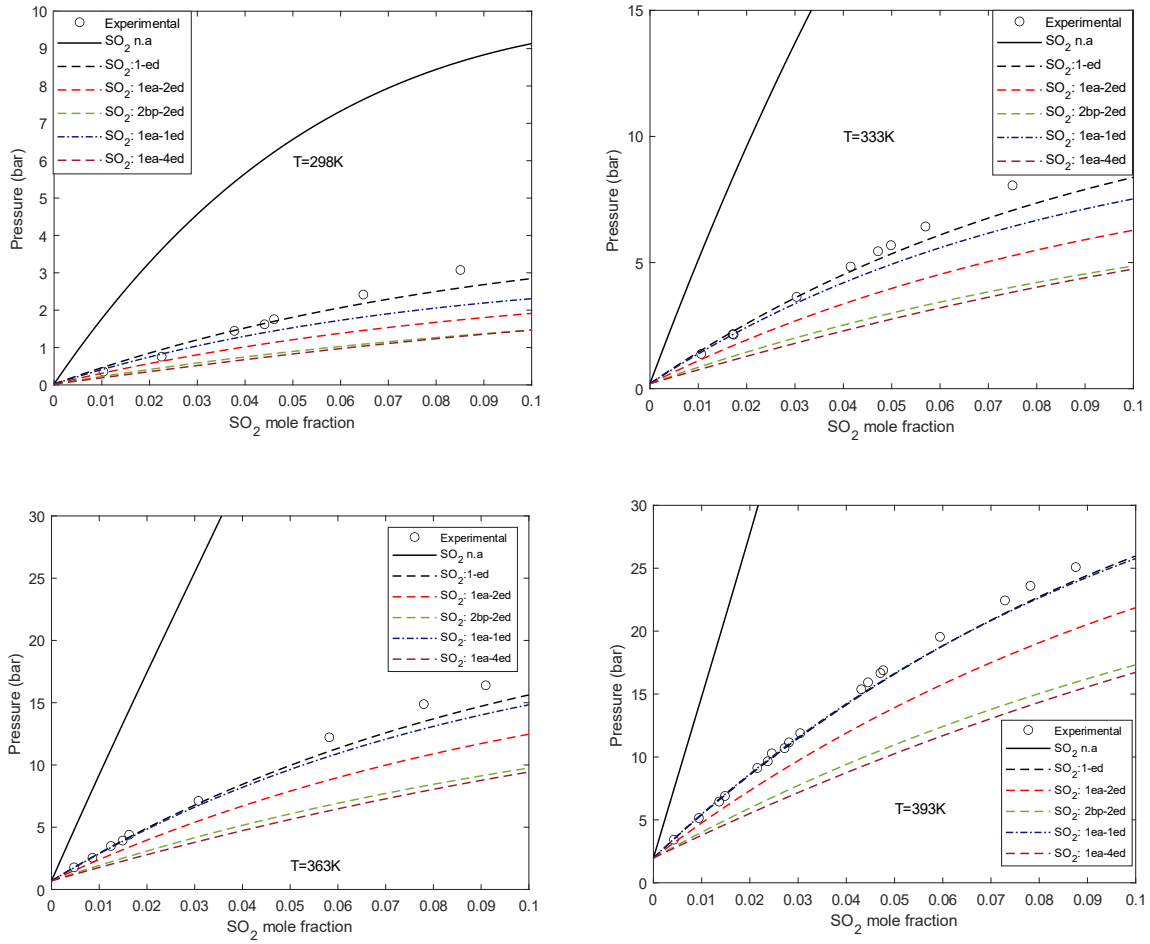

Figure 4.4: SO_2 solubility in water at various temperatures for CPA calculations performed across the proposed SO_2 association schemes, with kij=0. Experimental data [22] is shown as points, and CPA calculations as lines. To satisfactorily model this system, the figures show that the cross-association between SO_2 and water needs to be accounted.

To evaluate the CPA model's correlative capabilities, an adjustable binary interaction parameter, kij, is introduced. The kij was determined for each binary through the regression of the CPA model with the binary data. Figure 4.5 shows some characteristic plots of the SO_2 solubility modelled at two temperatures, with an adjustable kij. The model is still inaccurate when SO_2 is treated as a non-associating compound. For cases that allocate SO_2 association sites, Table 4.6, shows that the average deviation to experimental data is significantly reduced through the introduction of small kij with a magnitude less than 0.1.

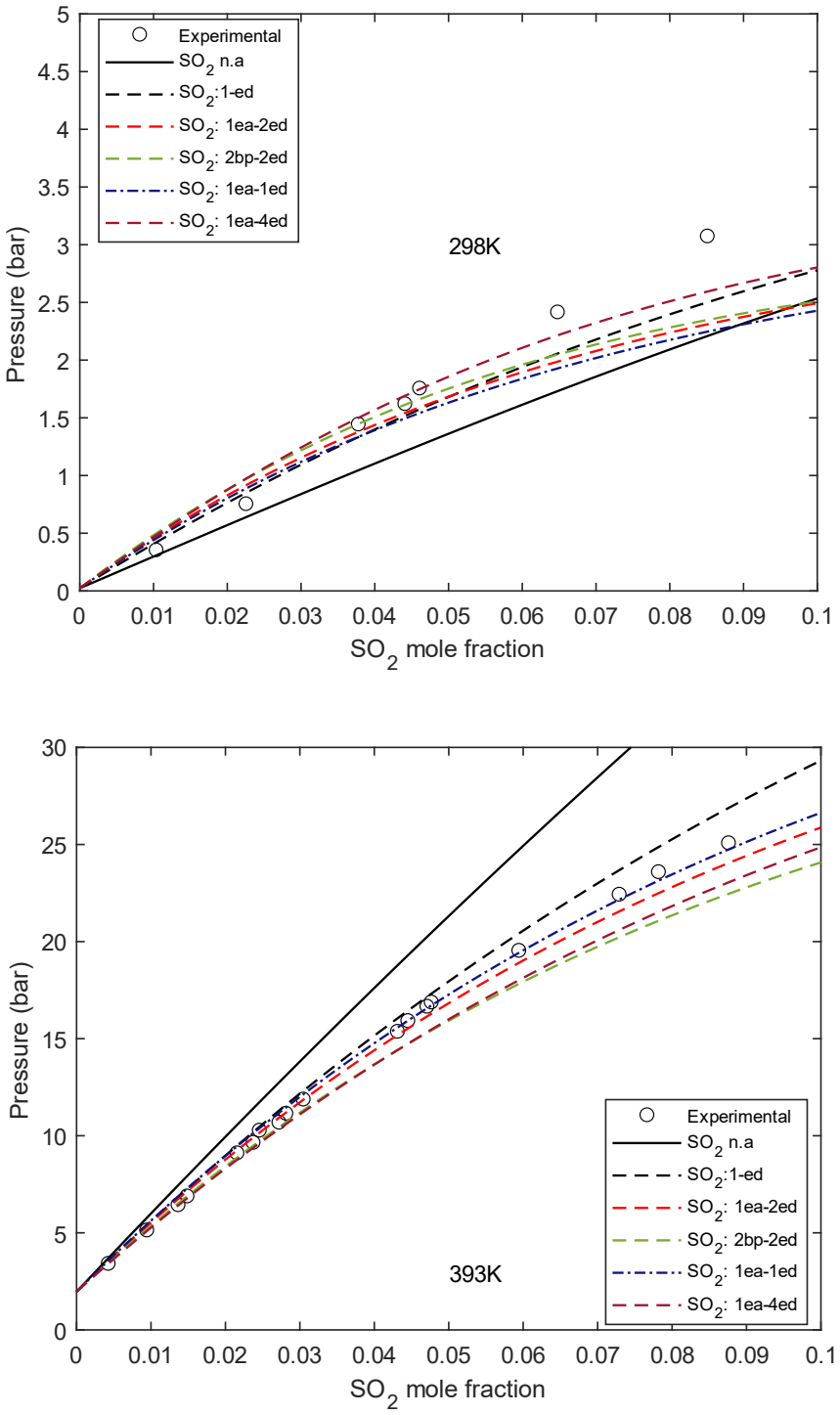

Figure 4.5: SO_2 solubility in water at various temperatures for CPA calculations at SO_2 association schemes, with an adjustable kij. Experimental data [22] points, and CPA calculations lines.

Table 4.6: CPA SO_2 solubility in water calculations and deviations from experimental data [22].

SO_2 association scheme	Non-adjustable kij		Adjustable kij		
	β_{cross} x 1000	%AAD in P	kij	β_{cross} x 1000	%AAD in P
n.a	-	242.60	-0.1460		8.24
1ed	313.51	6.97	-0.0388	185.94	3.96
1ea-2ed	CR-1	23.22	0.0325	CR-1	5.40
2bp-2ed	CR-1	40.49	0.0664	CR-1	6.34
1ea-1ed	CR-1	8.90	0.0062	CR-1	5.40
1ea-4ed	CR-1	45.43	0.0798	CR-1	5.43

4.4.1.2 SO_2-MEG

The availability of phase equilibria data for SO_2 and glycols in the open literature is limited, therefore, the CPA modelling is only performed for MEG at a temperature of 273 K, which is shown in Figure 4.6. Here, two approaches were taken, where the binary mixture was modelled with and without kijs (approach B and C) for cases where SO_2 is non-associating and can cross-associate with MEG. The deviations of these modelling approaches from experimental data are shown in Table 4.7.

Modelling SO_2 with a 1 ed site (solvation), shows the best agreement with the experimental data. This association scheme best describes the SO_2 solubility behaviour. This is since with this scheme, the model follows the same trend as the experimental data (even without an adjustable kij), where the saturation pressure rises steeply at low SO_2 concentrations, and later stabilises at higher concentrations.

In contrast, modelling SO_2 as a non-associating compound culminates in the underestimation of the SO_2 solubility across the pressure range, with this being improved when an adjustable kij is introduced. Furthermore, the modelling of SO_2 as non-associating culminates in the CPA model indicating the presence of liquid-liquid

equilibrium (LLE), resulting in significant inconsistencies with experimental data, especially when an adjustable kij is not used.

The rest of the association schemes predict an almost linear relationship between SO_2 solubility in MEG and pressure. Therefore, both Figure 4.6 (a) and (b) illustrate that to obtain positive agreement with experimental data, the CPA model requires the accounting of SO_2 and MEG cross-association.

Table 4.7: CPA calculations for SO_2 solubility in MEG and deviations from experimental data [23].

SO_2 association scheme	**Non-adjustable kij**		**Adjustable kij**		
	β_{cross} x 1000	**%AAD in *P***	**kij**	**β_{cross} x 1000**	**%AAD in *P***
n.a	-	225.99	-0.1151	-	8.31
1ed	350.75	8.08	-0.0110	289.37	8.00
1ea-2ed	CR-1	22.97	-0.0262	CR-1	17.62
2bp-2ed	CR-1	19.77	-0.00910	CR-1	19.19
1ea-1ed	CR-1	27.83	-0.0353	CR-1	18.36
1ea-4ed	CR-1	16.81	-0.0123	CR-1	15.27

(a) $kij = 0$

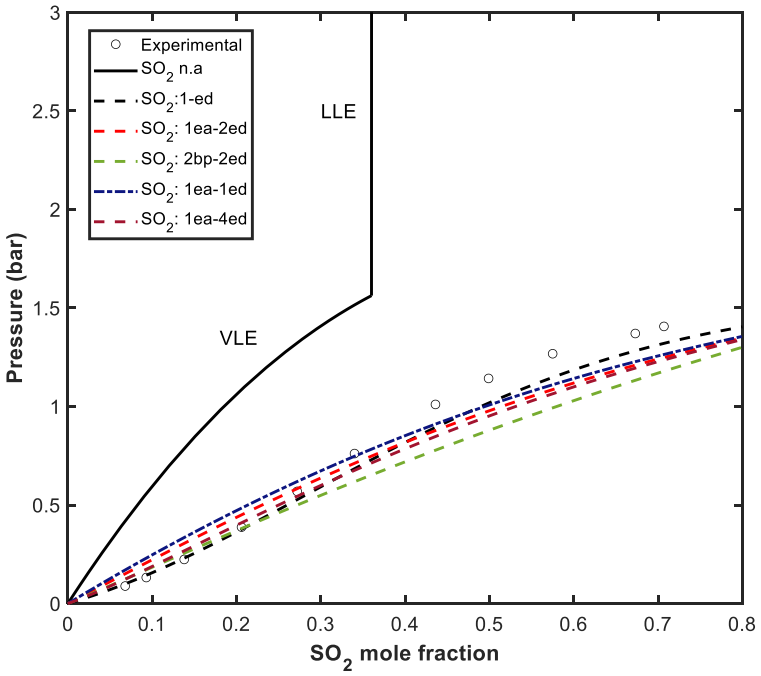

(b) Adjustable kij

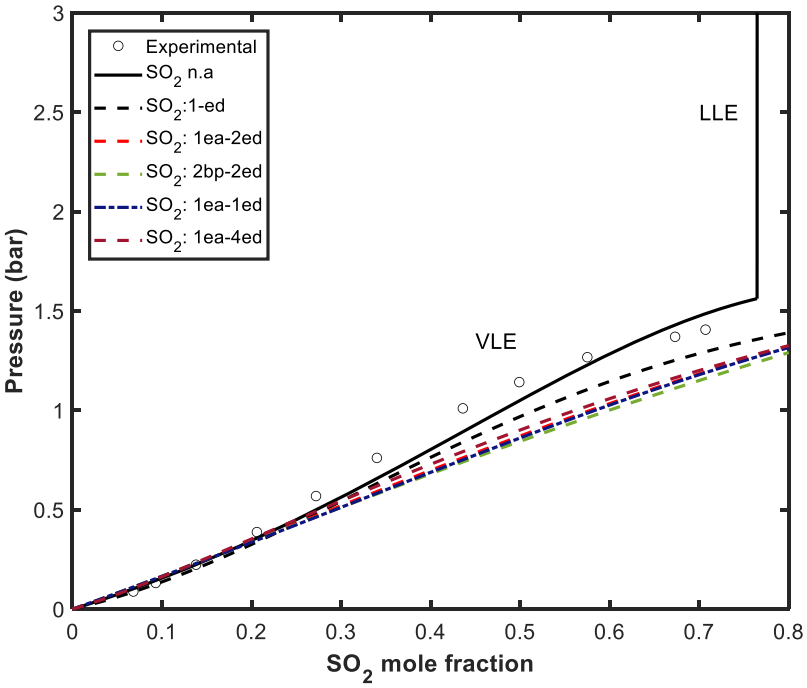

Figure 4.6: SO_2 solubility in MEG at various association schemes at 273 K. CPA calculations (lines) and experimental data [23] (points) of SO_2 solubility in MEG. Modelling SO_2 with 1 negative site (solvation) best describes the experimental data.

4.4.1.3 SO_2-CO_2

The vapour-liquid-equilibrium (VLE) of SO_2-CO_2 was modelled for different SO_2 association schemes, while CO_2 is treated as a non-associating compound, consistent with approach C1, from Table 4.5. These CPA modelling calculations are shown in Figure 4.7 and the average deviation from experimental data is presented in Table 4.8. All modelling treatments of SO_2 reproduce the experimental data. This is slightly improved when SO_2 is modelled as self-associating, which further minimises the deviation from experimental data, even when a kij is employed. The introduction of a kij, improves the overall model performance, however, for cases where is modelled as self-associating, this compromises the accuracy of the vapour phase composition.

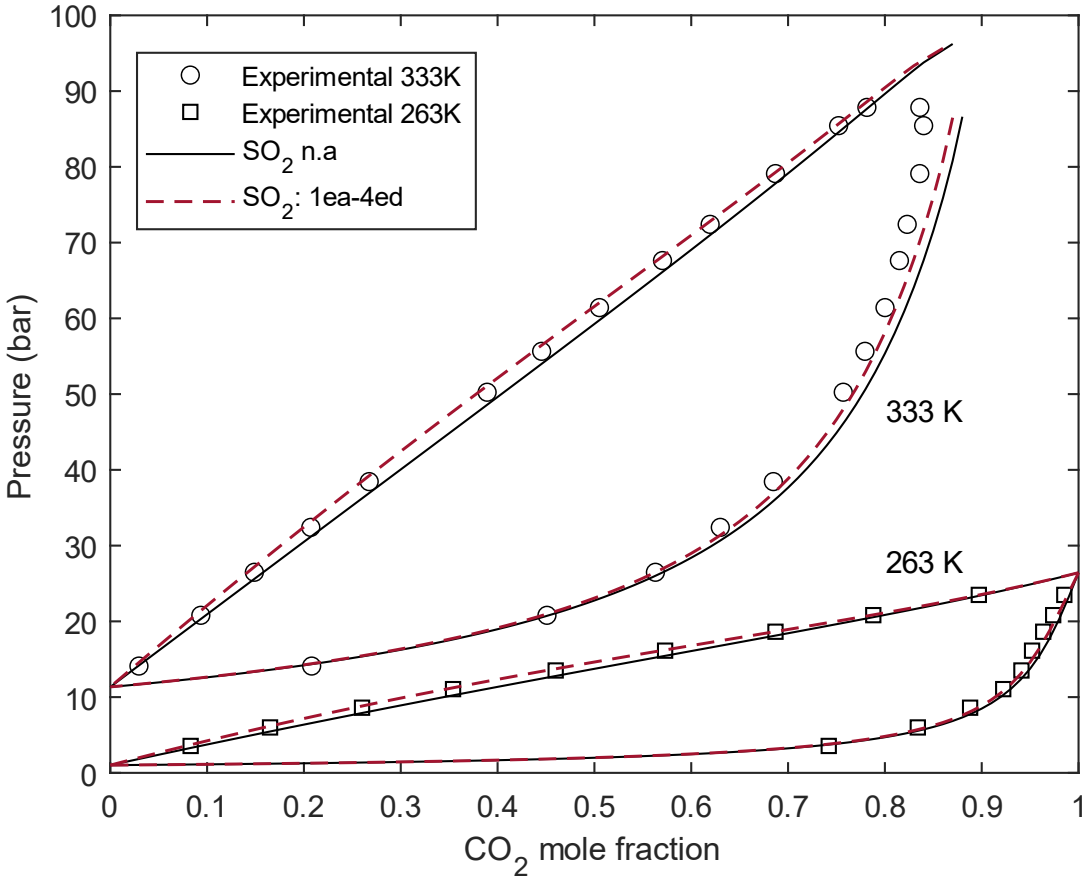

Figure 4.7: SO_2-CO_2 VLE modelling at 263 K and 333 K, with experimental data (points) [24]. CPA calculations were performed without the use of kijs. This indicates that the allocation of association sites yields slightly improved VLE predictions relative to the treatment of SO_2 as non-associating.

Table 4.8: CPA calculations for SO_2-CO_2 VLE and deviations from experimental data [24].

SO_2 association scheme	Non-adjustable kij		Adjustable kij		
	%AAD in *y*	%AAD in *P*	kij	%AAD in *y*	%AAD in *P*
n.a	8.13	6.55	0.0177	5.08	3.85
1ea-2ed	4.45	3.89	-0.0041	5.02	3.76
2bp-2ed	4.41	3.86	-0.0037	4.91	3.76
1ea-1ed	4.48	3.94	-0.0047	5.15	3.76
1ea-4ed	4.45	3.87	-0.0037	4.95	3.76

4.4.1.4 SO_2-O_2

Similarly, to the previous section, the VLE of the SO_2-O_2 binary mixture is modelled taking for cases where O_2 is treated as inert, while SO_2 is treated as non-associating or self-associating. The VLE calculations of this binary mixture are shown in Figure 4.8, while the deviations are reported in Table 4.9.

Modelling this binary system without kijs results in the overestimation of the critical point. This is a common drawback of the CPA model [19,25] since the pure component parameters of the CPA model have been determined away from the pure component's critical pressure and temperature. Therefore, close to the critical point, the model should be employed with caution. The use of a binary interaction parameter, further depresses the model's critical point, yielding a significant reduction in the deviation from experimental data. An assessment of Table 4.9 illustrates that for this system, the allocation of SO_2 association sites has a limited effect on improving the outputs of the model.

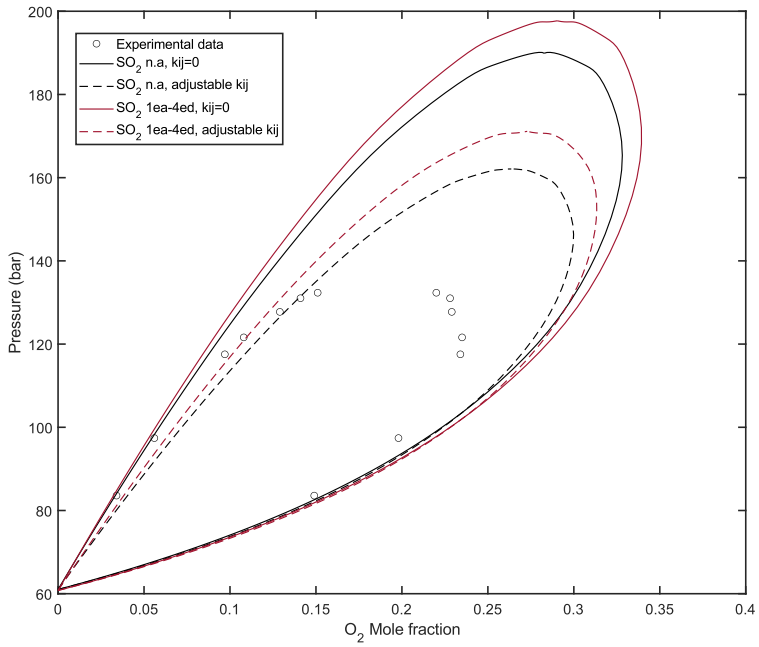

Figure 4.8: SO_2-O_2 VLE at 413.5 K, with CPA calculations performed considering an adjustable kij, and kij=0 for cases where SO_2 is non-associating or SO_2 following the 1ea-ed scheme. Experimental data [26] is shown as points, with lines showing CPA calculations.

Table 4.9: CPA SO_2-O_2 VLE calculations and deviations from experimental data [26].

SO_2 Association scheme	**Non-adjustable kij**		**Adjustable kij**		
	%AAD in *y*	**%AAD in *P***	**kij**	**%AAD in *y***	**%AAD in *P***
n.a	10.55	20.31	0.1562	3.76	7.33
1ea-2ed	9.34	17.97	0.1345	3.92	7.97
2bp-2ed	9.46	17.96	0.1358	3.92	7.95
1ea-1ed	9.18	17.95	0.1325	3.92	8.07
1ea-4ed	9.42	17.98	0.1354	3.92	7.96

4.4.2 Binary mixtures with COS

4.4.2.1 COS-glycol series

The CPA calculations of COS solubility in glycols were performed for cases where kij=0, and adjustable kijs were employed.

The implementation of COS-glycol modelling was unsuccessful without the incorporation of an adjustable binary interaction parameter. Figure 4.9 illustrates this for a computation where COS is treated as inert, and self-associating, with kij=0. At a select pressure and temperature, the CPA model, qualitative follows the same trend as the experimental data. However, the COS solubility across the glycols is overestimated. The apparent overestimation may be due to the presence of water as an impurity in glycols used in experiments. Water has been shown to drive the hydrolysis of COS [27], however its role in the limited experimental data is not discussed.

Table 4.10 to Table 4.12 presents the modelling results for the COS-glycols binary systems, where an adjustable and non-adjustable kij is used. Figure 4.10 presents characteristic calculations of the solubility of COS in glycols across the 288 K to 333 K temperature range. Modelling with an adjustable kij significantly improves the CPA computations. Across all glycols, the best performance is achieved when COS is treated as an inert compound. In these cases, the modelling of COS as solvating in the glycols does not culminate in improved modelling, rather, the optimise cross-association volume is low. This may suggest that cross-association between COS and glycols is limited (see also equation (4.3)). This is further supported by other COS association schemes having a high average deviation relative to experimental data (though this decreases as the molecular weight of the glycol rises).

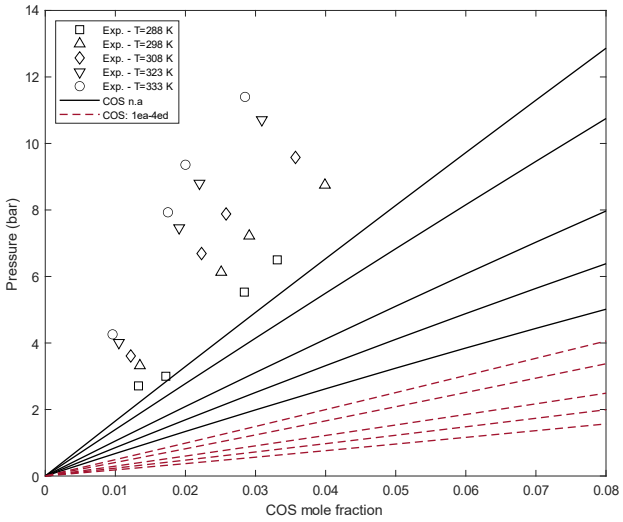

Figure 4.9: COS solubility in MEG, with CPA calculations performed without a binary interaction parameter. This indicates that the CPA model significantly overestimates the COS solubility across the pressure and temperature range of the experimental data [28].

(a) COS-MEG

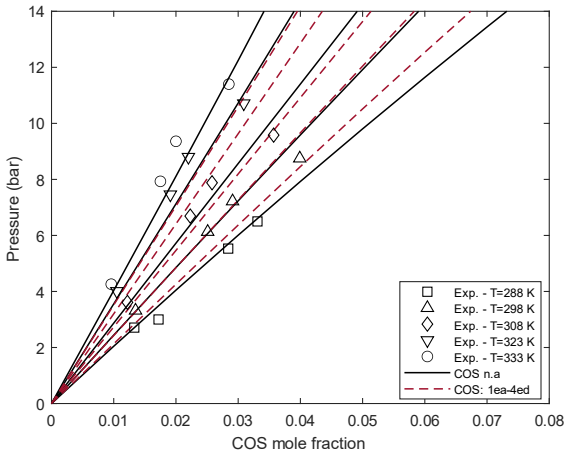

(b) COS-DEG

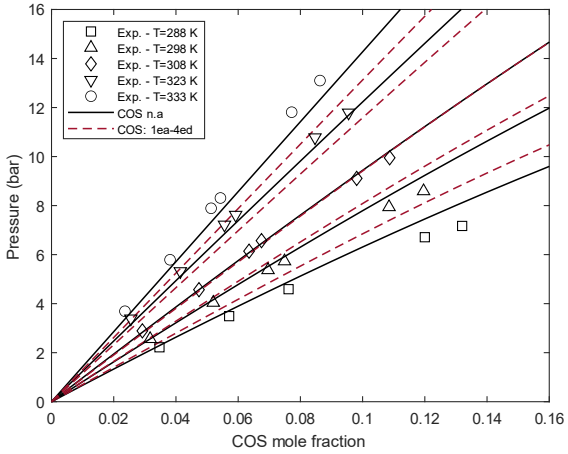

(c) COS-TEG

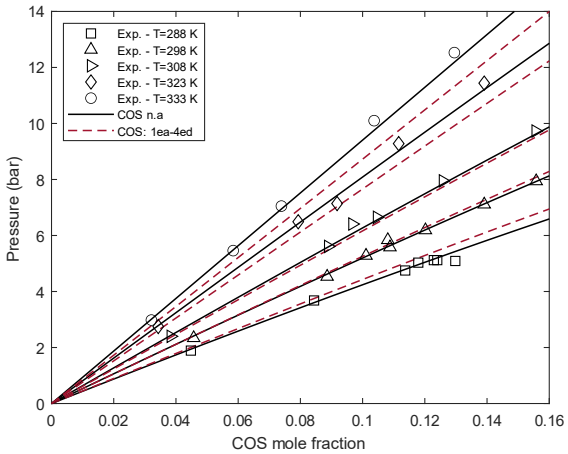

Figure 4.10: COS solubility in glycols at various temperatures. Experimental data [28] is shown as points and CPA calculations shown as lines are for cases where COS is non-associating, and a characteristic case where COS has association sites (1ea-4ed).

Table 4.10: CPA calculations for COS solubility in MEG and deviations from experimental data [28].

COS association scheme	Non-adjustable kij		Adjustable kij		
	β_{cross} x 1000	%AAD in P	kij	β_{cross} x 1000	%AAD in P
n.a	-	64.28	0.0949	-	6.11
1ed	0.50	64.38	0.0955	0.50	6.12
1ea-2ed	CR-1	86.48	0.1894	CR-1	10.48
2bp-2ed	CR-1	89.1	0.2099	CR-1	11.67
1ea-1ed	CR-1	84.38	0.1757	CR-1	9.74
1ea-4ed	CR-1	89.67	0.2149	CR-1	12.33
2ea-2ed	CR-1	86.84	0.1919	CR-1	10.55

Table 4.11: CPA calculations for COS solubility in DEG and deviations from experimental data [28].

COS association scheme	Non-adjustable kij		Adjustable kij		
	β_{cross} x 1000	%AAD in P	kij	β_{cross} x 1000	%AAD in P
n.a	-	50.97	0.0739	-	4.38
1ed	0.50	51.32	0.0747	0.50	4.41
1ea-2ed	CR-1	77.48	0.1594	CR-1	7.56
2bp-2ed	CR-1	81.03	0.1780	CR-1	8.41
1ea-1ed	CR-1	74.98	0.1481	CR-1	6.95
1ea-4ed	CR-1	81.44	0.1801	CR-1	9.25
2ea-2ed	CR-1	77.88	0.1614	CR-1	4.38

Table 4.12: CPA calculations for COS solubility in TEG and deviations from experimental data [28].

COS association scheme	Non-adjustable kij		Adjustable kij		
	β_{cross} x 1000	%AAD in P	kij	β_{cross} x 1000	%AAD in P
n.a	-	50.14	0.0755	-	1.82
1ed	0.50	50.31	0.0759	0.50	1.82
1ea-2ed	CR-1	74.50	0.1523	CR-1	3.76
2bp-2ed	CR-1	78.00	0.1690	CR-1	4.38
1ea-1ed	CR-1	72.18	0.1426	CR-1	3.44
1ea-4ed	CR-1	78.37	0.1708	CR-1	4.8
2ea-2ed	CR-1	74.74	0.1534	CR-1	3.75

4.4.2.2 COS-CO_2

The VLE of COS and CO_2 binary was modelled at two temperature conditions, shown in Figure 4.11. Here two approaches were explored, whereby the system was modelled without kijs (approach A1), and with an adjustable (approach A2). In both approaches, COS and CO_2 were treated as inert compounds.

From Figure 4.11, the model was incapable of predicting the VLE of the binary system when a kij is not employed. In particular, the model poorly models the liquid phase, when the overall CO_2 composition exceeds a mole fraction of 0.5. The introduction of a kij, significantly improves the VLE calculations of the model. Through this approach, an AAD of 1.47% is achieved (see Table 4.8), across the temperature range.

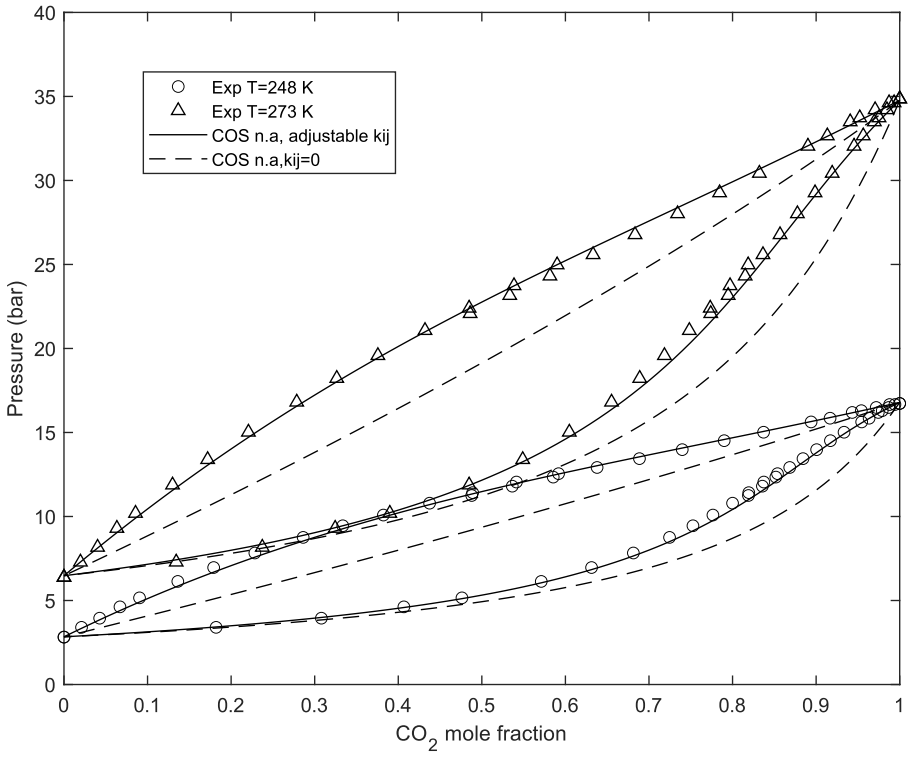

Figure 4.11: COS-CO_2 VLE at two temperatures. Points indicate experimental data [29], while lines show CPA calculations. This shows that introducing an adjustable kij significantly improves CPA computations.

Table 4.13: CPA calculations for COS-CO_2 VLE and deviations from experimental data [29].

COS Association scheme	**Non-adjustable kij**		**Adjustable kij**		
	%AAD in *y*	**%AAD in *P***	**kij**	**%AAD in *y***	**%AAD in *P***
n.a	18.69	11.68	0.0833	2.34	1.06
1ea-2ed	15.44	9.06	0.0646	2.23	1.08
2bp-2ed	15.34	9.04	0.0644	2.16	1.06
1ea-1ed	15.19	8.98	0.064	2.12	1.03
1ea-4ed	15.28	9.02	0.0642	2.14	1.04
2ea-2ed	15.16	8.97	0.0639	2.11	1.03

4.4.2.3 COS-CH_4

VLE calculations for the COS-CH_4 system were performed using two approaches. The first approach sets kij=0, while the second approach allowed for an adjustable kij.

The results of both approaches are shown in Table 4.14, with characteristic plots shown in Figure 4.12.

(a) COS-CH_4 VLE with kij=0

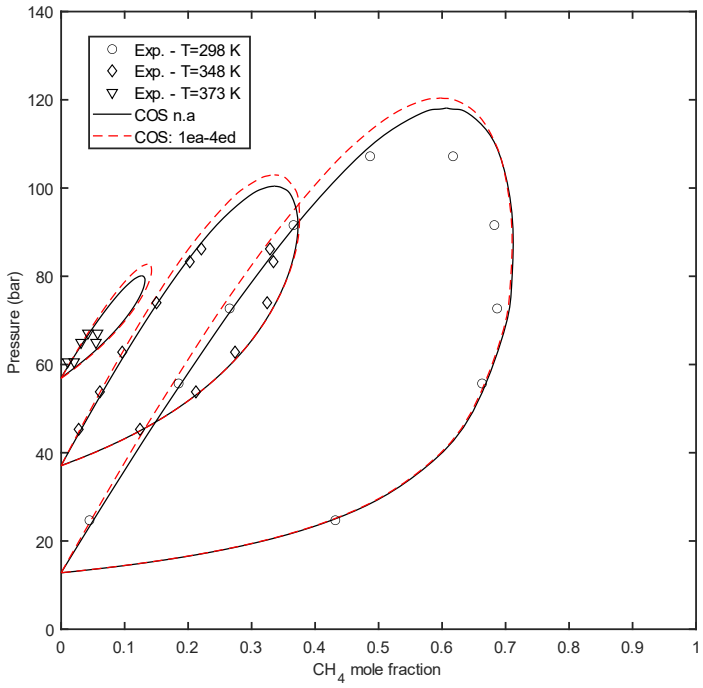

(b) COS-CH_4 VLE with adjustable kij

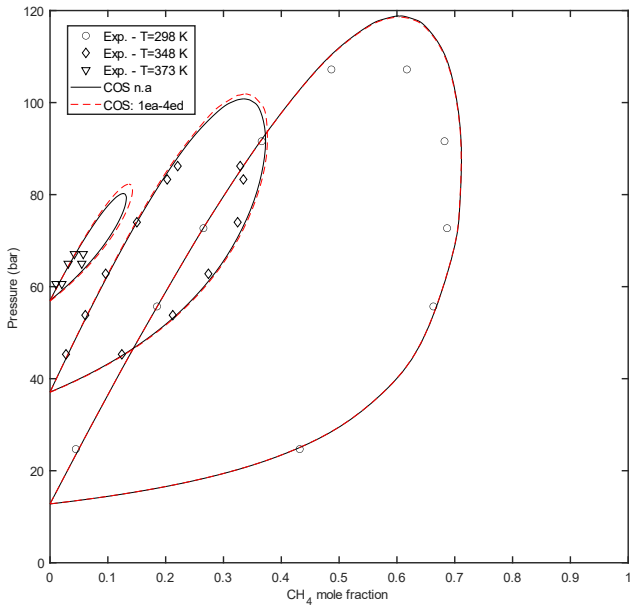

Figure 4.12: VLE calculations of COS-CH_4, utilising an adjustable and non-adjustable kij.. CPA calculations are represented as lines, while experimental data [30] as points.

Across all COS association schemes, COS-CH_4 VLE calculations are in satisfactory agreement with experimental data, even in cases with a kij. The model yields liquid concentrations consistent with experimental data, while the vapour concentration exceeds an AAD of 6.70% in both modelling cases. From Figure 4.12, as expected for the CPA model, the model overestimates the mixture's critical point.

Table 4.14: CPA calculations for COS-CH_4 VLE and deviations from experimental data [30].

COS Association scheme	Non-adjustable kij		Adjustable kij		
	%AAD in y	%AAD in P	kij	%AAD in y	%AAD in P
n.a	6.98	7.02	0.0058	6.91	6.94
1ea-2ed	6.79	7.58	-0.0161	6.92	7.11
2bp-2ed	6.72	7.57	-0.0165	6.85	7.08
1ea-1ed	6.87	7.61	-0.0159	7.00	7.14
1ea-4ed	6.75	7.57	-0.0162	6.88	7.09
2ea-2ed	6.69	7.56	-0.0165	6.82	7.07

4.4.3 Binary mixtures with H_2S

4.4.3.1 COS-H_2S

In the open literature, COS-H_2S VLE data is limited, and in this work, only liquid phase data was obtained. Predictive ($kij = 0$) VLE calculations were performed for the COS-H_2S binary system, using different association schemes for both compounds. Table 4.15 shows the results of the average deviation across all association scheme combinations. Figure 4.13 shows a characteristic VLE plot of the COS-H_2S system, where both compounds are modelled as inert and a case where H_2S is self-associating.

The treatment of both compounds as non-associating leads to the underestimation of the COS liquid mole fraction. However, when H_2S is treated as inert, and COS is self-associating, the average deviation is slightly minimised, with all COS schemes showing a similar performance (see Table 4.15). The best association scheme combinations are when COS is treated as non-associating, with the treatment of H_2S as a self-associating compound. The approach also predicts the appearance of an azeotrope at all temperature conditions. The azeotrope can be correlated for non-associating systems when an interaction parameter is employed.

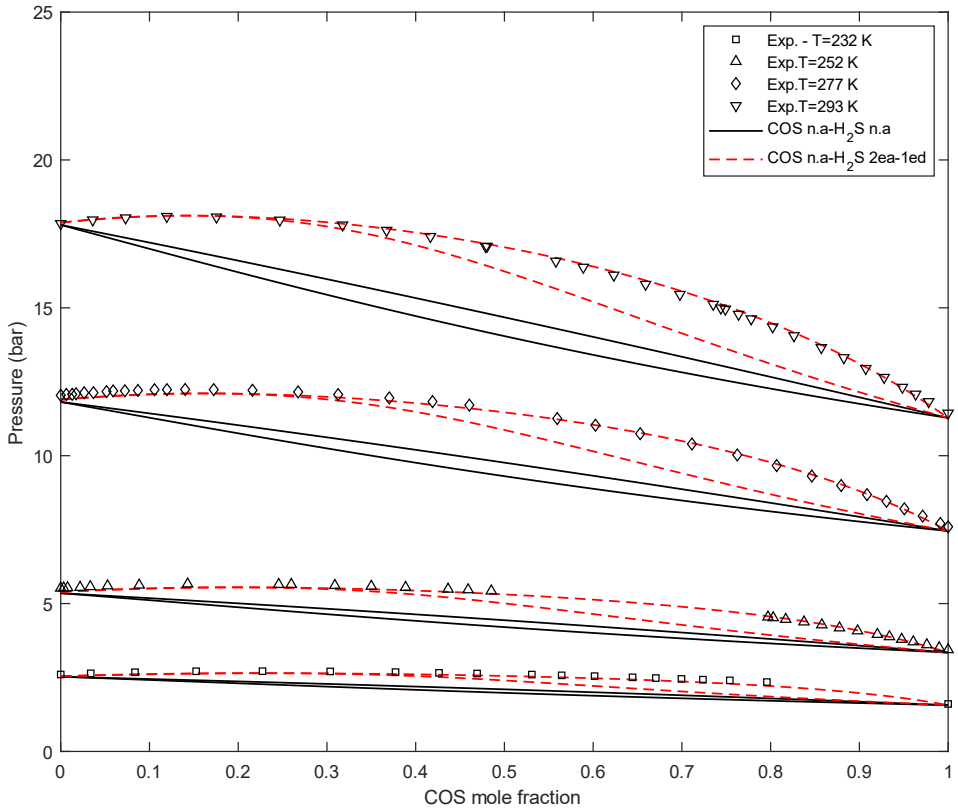

Figure 4.13: COS-H_2S VLE CPA predictions (kij=0) compared to liquid phase experimental data [31]. Cases shown are when both COS-H_2S were modelled as inert or when H_2S is modelled as self-associating.

Table 4.15: Pressure deviations for COS-H_2S CPA calculations performed at combinations of proposed COS and H_2S association schemes and kij=0. Experimental data from [31].

H_2S / COS	n.a	1ea-1ed	2ea-1ed	2ea-2ed	1ea-2ed	2bp
n.a	10.03	3.43	3.39	3.91	3.39	3.44
1ea-2ed	7.45	8.94	11.49	9.75	9.3	13
2bp-2ed	7.39	10.76	12.88	10.81	10.49	10.46
1ea-1ed	7.47	7.98	9.74	9.21	9.74	11.57
1ea-4ed	7.43	10.77	14.11	11.18	9.69	15.79
2ea-2ed	7.38	8.9	10.13	9.36	10.13	12.81

4.4.3.2 H_2S-CO_2

The VLE of the H_2S-CO_2 was computed for cases with $kij = 0$, and an adjustable kij (shown in Figure 4.14). Figure 4.14 illustrates that accounting for H_2S self-association, even without a binary interaction parameter, leads to satisfactory predictions of the H_2S-CO_2 VLE. In contrast, modelling H_2S as inert and without a binary interaction parameter culminates in the model being incapable of predicting the system's VLE behaviour, especially the liquid phase (see Figure 4.14(a)).

Table 4.16 shows the average deviation of the CPA model from experimental data. The association schemes that consider H_2S having two association sites (schemes 2bp, and 1ea-1ed) provide the most satisfactory results when a binary interaction parameter is not implemented. The rest of the association schemes require a positive kij to provide a satisfactory agreement with experimental data.

(a) kij=0 (b) Adjustable kij

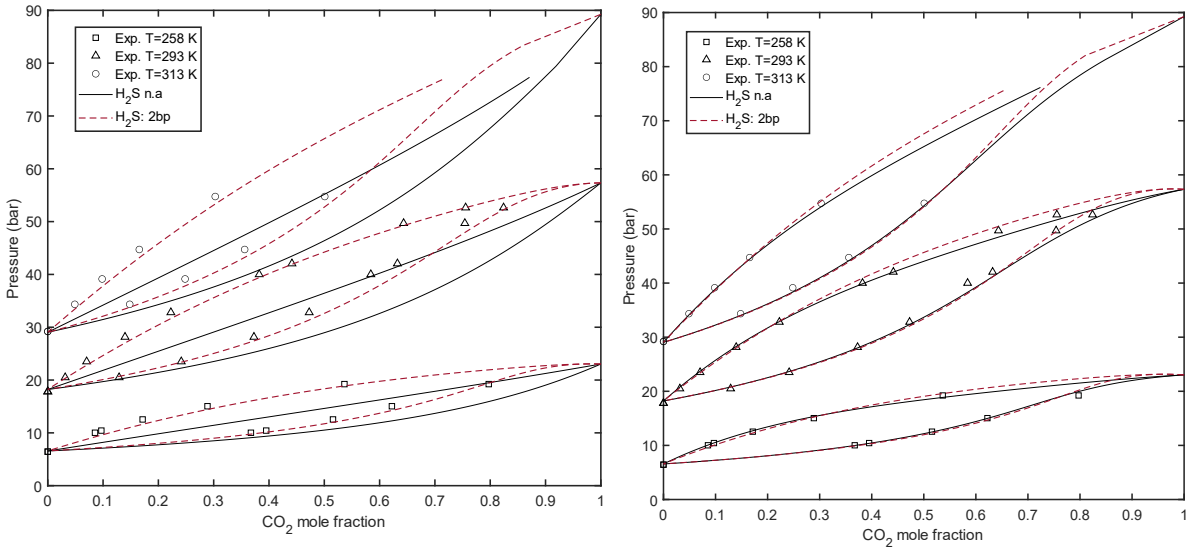

Figure 4.14: H_2S-CO_2 VLE over various temperatures, with points showing experimental data [32] and lines indicating CPA calculations. Modelling is performed for cases with kij=0, and an adjustable kij.

Table 4.16: H_2S-CO_2 VLE CPA calculations and deviations from experimental data [32].

H_2S association scheme	Non-adjustable kij		Adjustable kij		
	%AAD in *y*	%AAD in *P*	kij	%AAD in *y*	%AAD in *P*
n.a	24.89	13.31	0.1058	1.45	1.29

H_2S association scheme	Non-adjustable kij		Adjustable kij		
	%AAD in *y*	%AAD in *P*	kij	%AAD in *y*	%AAD in *P*
1ea-1ed	7.99	3.2	0.0226	3.09	1.95
2ea-1ed	15.92	7.51	0.0584	1.71	1.31
2ea-2ed	15.12	7.86	0.0607	1.55	1.29
1ea-2ed	15.92	7.51	0.0584	1.71	1.31
2bp	7.98	3.2	0.0225	3.09	1.95

4.4.4 Multicomponent system CO_2-SO_2-O_2

Pressure-Temperature (PT) flash calculations were performed for the SO_2(1)-O_2(2)-CO_2(3) system. Here, CO_2 and O_2 were modelled as inert compounds, while different association schemes for SO_2 were considered. In performing these computations, the kijs presented in Table 4.8 and Table 4.9 for the SO_2-CO_2, and SO_2-O_2 systems, were employed.

Figure 4.15 presents a characteristic vapour liquid phase envelope of the SO_2(1)-O_2(2)-CO_2 system, for a global mole fraction 0.0512/0.0283/0.9205, for cases where SO_2 is modelled as non-associating or self-associating via the 1ea-2ed association scheme. The experimental data points [33] shown in Figure 4.15 represent equilibrium states at a constant global composition, with experiments performed at a set of fixed temperatures, and varying system pressures where vapour and liquid phases were observed.

Figure 4.15 illustrates that the treatment of SO_2 as non-associating or associating culminates in satisfactory modelling of the phase envelope of this system, as all equilibrium data sets fall within the bounds of the envelopes. However, the different modelling treatments of SO_2 results in significant differences in computed vapour and liquid phase composition. These differences are presented in Table 4.17, which shows the deviation of the CPA model to experimental compositions of the liquid and vapour phases for the different SO_2 association schemes. Across the association schemes, the SO_2 and CO_2 liquid and CO_2 vapour compositions have a low AAD of less than 4.3%. However, the model is unable to capture the vapour phase and O_2 compositions across both phases. Furthermore, Table 4.17 shows that accounting for SO_2 self-association, yields a slight improvement in the computation of the vapour phase composition. Across all association schemes, the 1ea-1ed scheme yields the lowest overall AAD.

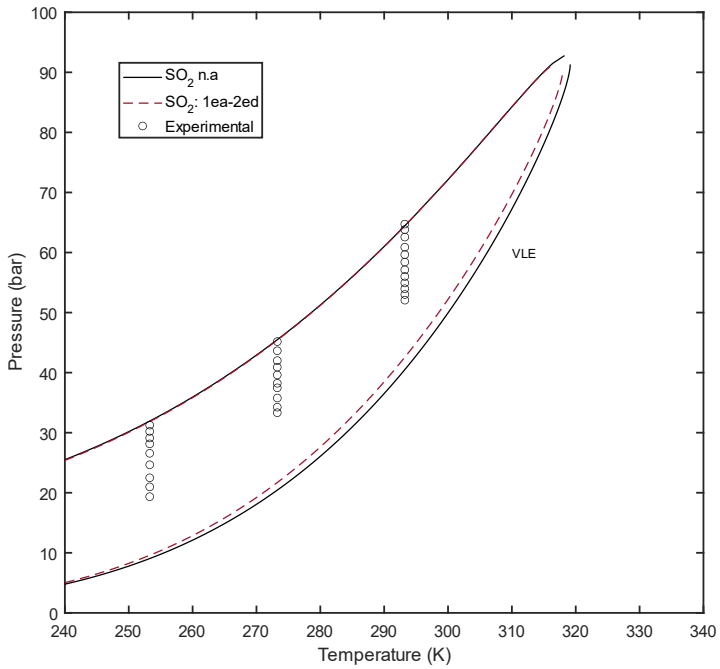

Figure 4.15: Pressure-Temperature phase envelope of the SO_2(1)-O_2(2)-CO_2 with mole fraction 0.0512/0.0283/0.9205. Points indicate experimental data pressure and temperature where vapour and liquid phases were observed [33]. CO_2 and O_2 are modelled as non-associating.

Table 4.17: CPA liquid and vapour phase composition calculations deviation from experimental data [33] for the SO_2(1)-O_2(2)-CO_2 (3) system. In these computations, the kijs presented in Table 4.8 andTable 4.9 were employed for the respective SO_2 association schemes.

SO_2 association scheme	**%AAD in x_1**	**%AAD x_2**	**%AAD x_3**	**%AAD y_1**	**%AAD y_2**	**%AAD y_3**
n.a	4.2	15.6	0.18	30.72	12.06	1.18
1ea-2ed	3.85	14.95	0.16	19.25	9.76	1.11
2bp-2ed	3.89	15.06	0.16	19.62	9.89	1.12
1ea-1ed	3.80	14.79	0.15	18.7	9.57	1.10
1ea-4ed	3.88	15.02	0.16	19.52	9.85	1.12

4.5 Conclusions

The CPA equation of state is applied to study the effect of allocating association sites to sulphur compounds – SO_2, COS, and H_2S – when modelling the binary and

multicomponent systems' phase equilibria containing these compounds. In performing this analysis, the predictive and correlative capabilities of the CPA model were evaluated. Furthermore, new association schemes and CPA parameters are proposed for the sulphur compounds.

The study found that the introduction of self-association or considering solvation for COS in the model has limited benefits in describing the phase equilibria of COS mixtures. In glycols, COS-CH_4, and COS-H_2S binary systems, modelling COS as non-associating yielded the best performance.

Systems with H_2S have been extensively studied with the CPA equation of state. This work develops new CPA parameters and proposes two new H_2S association schemes – 2ea-1ed and 2 bp. This work has found that the new parameters can satisfactorily describe the behaviour of systems for H_2S with glycols, and CO_2. The proposed 2 bp association scheme is found to have a similar performance to the previously proposed 1ea-1ed scheme.

When modelling systems with SO_2 it was necessary to account for self-association or solvation. When modelling the solubility of SO_2 in MEG or water, a case that considered the solvation of SO_2 yielded the best agreement with experimental data, even for cases without an adjustable binary interaction parameter ($kij = 0$). Furthermore, in the SO_2-O_2-CO_2 multicomponent system, this work demonstrated that cases with SO_2 as self-associating had a better performance compared with no association sites.

Nomenclature

Abbreviation	
AAD	Average absolute deviation (%)
bp	Bipolar site
CPA	Cubic Plus Association
CCS	Carbon Capture and Storage
ea	Electron acceptor site
EoS	Equation of state
ed	Electron donor site
DEG	Di-ethylene glycol
LLE	Liquid liquid equilibrium
MEG	Mono-ethylene glycol

n.a	Non-associating
SRK	Soave Redlich Kwong equation of state
TEG	Tri-ethylene glycol
VLE	Vapour liquid equilibrium
Mathematical Symbols	
b	Co-volume, $\left[\frac{\mathrm{cm}^3}{\mathrm{mol}}\right]$
c_1	Attractive energy temperature-correction
g	Radial distribution function
k_{ij}	Binary interaction parameter
P	Pressure
P^{sat}	Saturation Pressure
R	Gas constant, $\left[\frac{\mathrm{J}}{\mathrm{mol}\cdot\mathrm{K}}\right]$
T	Temperature, [K]
T_c	Critical temperature, [K]
T_r	Reduced temperature, $\mathrm{T} = \frac{\mathrm{T}}{\mathrm{T_c}}$
V_m	Molar volume
X_{A_i}	Fraction of association sites A on molecule I which are not bonded to other active sites
β	Association volume
β^{cross}	Cross-association volume
Γ	Reduced energy term, $\Gamma = \frac{\mathrm{a_0}}{\mathrm{Rb}}$,[K]
ε	Association energy, $\left[\mathrm{bar}\cdot\frac{\mathrm{cm}^3}{\mathrm{mol}}\right]$
$\alpha(T)$	Temperature dependent energy term

Acknowledgements

This project has received funding from the European Union's Horizon 2020 research and innovation programme under Grant Agreement No 838031.

References

[1] R.T.J. Porter, M. Fairweather, M. Pourkashanian, R.M. Woolley, The range and level of impurities in CO2 streams from different carbon capture sources, International Journal of Greenhouse Gas Control 36 (2015) 161–174. https://doi.org/10.1016/j.ijggc.2015.02.016.

[2] I.S. Cole, P. Corrigan, S. Sim, N. Birbilis, Corrosion of pipelines used for CO2 transport in CCS: Is it a real problem?, International Journal of Greenhouse Gas Control 5 (2011) 749–756. https://doi.org/10.1016/j.ijggc.2011.05.010.

[3] P.D.N. Svoronos, T.J. Bruno, Carbonyl Sulfide: A Review of Its Chemistry and Properties, Ind Eng Chem Res 41 (2002) 5321–5336. https://doi.org/10.1021/ie020365n.

[4] H. Li, J. Yan, Evaluating cubic equations of state for calculation of vapor–liquid equilibrium of CO2 and CO2-mixtures for CO2 capture and storage processes, Appl Energy 86 (2009) 826–836. https://doi.org/10.1016/j.apenergy.2008.05.018.

[5] I. Tsivintzelis, G.M. Kontogeorgis, M.L. Michelsen, E.H. Stenby, Modeling phase equilibria for acid gas mixtures using the CPA equation of state. I. Mixtures with H2S, AIChE Journal 56 (2010) 2965–2982. https://doi.org/10.1002/aic.12207.

[6] S.P. Tan, Y. Yao, M. Piri, Modeling the Solubility of SO_2 + CO_2 Mixtures in Brine at Elevated Pressures and Temperatures, Ind Eng Chem Res 52 (2013) 10864–10872. https://doi.org/10.1021/ie4017557.

[7] G.M. Kontogeorgis, E.C. Voutsas, I. v. Yakoumis, D.P. Tassios, An Equation of State for Associating Fluids, Ind Eng Chem Res 35 (1996) 4310–4318. https://doi.org/10.1021/ie9600203.

[8] G.M. Kontogeorgis, I. v. Yakoumis, H. Meijer, E. Hendriks, T. Moorwood, Multicomponent phase equilibrium calculations for water–methanol–alkane mixtures, Fluid Phase Equilib 158–160 (1999) 201–209. https://doi.org/10.1016/S0378-3812(99)00060-6.

[9] M.S. Wertheim, Fluids with Highly Directional Attractive Forces. I. Statistical Thermodynamics, 1984.

[10] M.S. Wertheim, Fluids with Highly Directional Attractive Forces. II. Thermodynamic Perturbation Theory and Integral Equations, 1984.

[11] M.S. Wertheim, Fluids with Highly Directional Attractive Forces. III. Multiple Attraction Sites, 1986.

[12] W.G. Chapman, K.E. Gubbins, G. Jackson, M. Radosz, SAFT: Equation-of-state solution model for associating fluids, Fluid Phase Equilib 52 (1989) 31–38. https://doi.org/10.1016/0378-3812(89)80308-5.

[13] G.M. Kontogeorgis, M.L. Michelsen, G.K. Folas, S. Derawi, N. von Solms, E.H. Stenby, Ten Years with the CPA (Cubic-Plus-Association) Equation of State. Part 1. Pure Compounds and Self-Associating Systems, Ind Eng Chem Res 45 (2006) 4855–4868. https://doi.org/10.1021/ie051305v.

[14] J.C. de Hemptine, P. Mougin, A. Barreau, L. Ruffine, S. Tamouza, R. Inchekel, Application to Petroleum Engineering of Statistical Thermodynamics – Based Equations of State, Oil & Gas Science and Technology - Revue de l'IFP 61 (2006) 363–386. https://doi.org/10.2516/ogst:2006039a.

[15] I. Tsivintzelis, G.M. Kontogeorgis, M.L. Michelsen, E.H. Stenby, Modeling phase equilibria for acid gas mixtures using the CPA equation of state. Part II: Binary mixtures with CO2, Fluid Phase Equilib 306 (2011) 38–56. https://doi.org/10.1016/j.fluid.2011.02.006.

[16] G.M. Kontogeorgis, G.K. Folas, N. Muro-Suñé, F. Roca Leon, M.L. Michelsen, Solvation Phenomena in Association Theories with Applications to Oil & Gas and Chemical Industries, Oil & Gas Science and Technology - Revue de l'IFP 63 (2008) 305–319. https://doi.org/10.2516/ogst:2008025.

[17] I. Tsivintzelis, G.M. Kontogeorgis, M.L. Michelsen, E.H. Stenby, Modeling phase equilibria for acid gas mixtures using the CPA equation of state. I. Mixtures with H2S, AIChE Journal 56 (2010) 2965–2982. https://doi.org/10.1002/aic.12207.

[18] Birmingham Young University (BYU), DIPPR DIADEM - The DIPPR Information and Data Evaluation Manager for the Design Institute for Physical Properties, (2006).

[19] I. Tsivintzelis, S. Ali, G.M. Kontogeorgis, Modeling Phase Equilibria for Acid Gas Mixtures using the Cubic-Plus-Association Equation of State. 3. Applications

Relevant to Liquid or Supercritical CO_2 Transport, J Chem Eng Data 59 (2014) 2955–2972. https://doi.org/10.1021/je500090q.

[20] G.M. Kontogeorgis, I. v. Yakoumis, H. Meijer, E. Hendriks, T. Moorwood, Multicomponent phase equilibrium calculations for water–methanol–alkane mixtures, Fluid Phase Equilib 158–160 (1999) 201–209. https://doi.org/10.1016/S0378-3812(99)00060-6.

[21] S.O. Derawi, M.L. Michelsen, G.M. Kontogeorgis, E.H. Stenby, Application of the CPA equation of state to glycol/hydrocarbons liquid–liquid equilibria, Fluid Phase Equilib 209 (2003) 163–184. https://doi.org/10.1016/S0378-3812(03)00056-6.

[22] B. Rumpf, G. Maurer, Solubilities of hydrogen cyanide and sulfur dioxide in water at temperatures from 293.15 to 413.15 K and pressures up to 2.5 MPa, Fluid Phase Equilib 81 (1992) 241–260. https://doi.org/10.1016/0378-3812(92)85155-2.

[23] H.W. Foote, J. Fleischer, Equilibrium in Systems Composed of Sulfur Dioxide and Certain Organic Compounds, J Am Chem Soc 56 (1934) 870–873. https://doi.org/10.1021/ja01319a031.

[24] C. Coquelet, A. Valtz, P. Arpentinier, Thermodynamic study of binary and ternary systems containing CO2+impurities in the context of CO2 transportation, Fluid Phase Equilib 382 (2014) 205–211. https://doi.org/10.1016/j.fluid.2014.08.031.

[25] A.M. Palma, M.B. Oliveira, A.J. Queimada, J.A.P. Coutinho, Re-evaluating the CPA EoS for improving critical points and derivative properties description, Fluid Phase Equilib 436 (2017) 85–97. https://doi.org/10.1016/j.fluid.2017.01.002.

[26] E. el Ahmar, B. Creton, A. Valtz, C. Coquelet, V. Lachet, D. Richon, P. Ungerer, Thermodynamic study of binary systems containing sulphur dioxide: Measurements and molecular modelling, Fluid Phase Equilib 304 (2011) 21–34. https://doi.org/10.1016/j.fluid.2011.02.008.

[27] W. Afzal, M. Amir, R. Dominique, Solubility of Sulfur Species in Glycol Aqueous Solutions, 2010.

[28] W. Afzal, M.P. Breil, I. Tsivintzelis, A.H. Mohammadi, G.M. Kontogeorgis, D. Richon, Experimental study and phase equilibrium modeling of systems

containing acid gas and glycol, Fluid Phase Equilib 318 (2012) 40–50. https://doi.org/10.1016/j.fluid.2011.12.025.

[29] R.J. McDougal, L. v. Jasperson, G.M. Wilson, Vapor–Liquid Equilibrium for Several Compounds Relevant to the Biofuels Industry Modeled with the Wilson Equation, J Chem Eng Data 59 (2014) 1069–1085. https://doi.org/10.1021/je400885z.

[30] N.H. Senturk, H. Kalra, D.B. Robinson, Vapor-liquid equilibrium in the methane-carbonyl sulfide binary system, J Chem Eng Data 24 (1979) 311–313. https://doi.org/10.1021/je60083a010.

[31] P. Guilbot, P. Théveneau, A. Baba-Ahmed, S. Horstmann, K. Fischer, D. Richon, Vapor–liquid equilibrium data and critical points for the system H2S+COS. Extension of the PSRK group contribution equation of state, Fluid Phase Equilib 170 (2000) 193–202. https://doi.org/10.1016/S0378-3812(00)00352-6.

[32] A. Chapoy, C. Coquelet, H. Liu, A. Valtz, B. Tohidi, Vapour–liquid equilibrium data for the hydrogen sulphide (H2S)+carbon dioxide (CO2) system at temperatures from 258 to 313K, Fluid Phase Equilib 356 (2013) 223–228. https://doi.org/10.1016/j.fluid.2013.07.050.

[33] C. Coquelet, A. Valtz, P. Arpentinier, Thermodynamic study of binary and ternary systems containing CO2+impurities in the context of CO2 transportation, Fluid Phase Equilib 382 (2014) 205–211. https://doi.org/10.1016/j.fluid.2014.08.031.

5 Water content measurements in compressed fluids (CO_2, H_2, N_2) using in-situ Raman spectroscopy

Abstract

This study provides an approach towards the quantitative determination of water content in compressed gas streams using only water-specific Raman spectra features. In an equilibrium cell, in-situ Raman scattering measurements were conducted for the CO_2-water, N_2-water, and H_2-water vapour phases at isothermal conditions and pressures ranging from 5 to 15 MPa. This study finds that the Raman peak position of the water symmetric stretch can be employed as a reliable indicator of water concentration. A correlation relating the water vapour phase concentration to the water symmetric stretch peak position is developed for the CO_2-water system and is successfully applied to the N_2-water and H_2-water systems yielding a satisfactory accuracy in predicting the water concentration for these systems.

5.1 Introduction

The water content of CO_2, N_2, and H_2 rich streams are essential parameters for many industries. In both the carbon capture and storage, as well as the hydrogen value chains, the presence of water in hydrogen or carbon dioxide rich streams can compromise the integrity and performance of transportation pipelines. Previous studies have highlighted that water and carbon dioxide elevate the risk of pipeline corrosion [1], and under specific temperature and pressure conditions, the formation of hydrates could be triggered, prompting pipeline plugging [2,3]. Apart from being a main impurity in post-combustion capture, the water content of N_2 is also relevant to the design of air separation units [4]. In the utilisation of H_2 in Proton Exchange Membrane Fuel Cells (PEMFCs), the influence of hydrogen water content is equally critical. Excessive water diminishes the diffusion of reactants to the catalyst, thus, impairing the normal functioning of PEMFCs [5]. As such, the precise and continuous monitoring of the water content of CO_2, N_2, and H_2 rich streams is crucial for the optimal performance of various industrial applications.

Common analytical techniques employed in high-pressure equilibrium and on-line measurements, including gas chromatography, typically involve the extraction of samples from the phases of interest and conducting ex-situ analysis at near-ambient conditions [6]. However, this approach has inherent challenges, such as condensation

in sampling capillaries or the disruption of equilibrium in the cell due to pressure drop induced by the sampling process. These challenges compromise the accurate evaluation of e.g., phase compositions or adsorption measurements of humid gas mixtures. In addressing these limitations, in-situ Raman spectroscopy emerges as a favourable option, as it is a non-invasive analytical method, allowing for the real-time monitoring of each phase.

However, a constraint of Raman spectroscopy is the absence of a widely accepted method for compositional quantification. This is because sample and instrumental parameters, such as irradiance of scattering volume and absolute Raman scattering cross sections (RSCS), are not easily experimentally accessible [7]. The prevailing method for quantitative analysis in Raman spectroscopy builds upon the foundational work by Placzek [8]. This approach relies on developing relative calibrations of the species in a sample. This method is commonly referred to as the 'ratio method'. It involves computing the Raman spectra peak area ratios of key species to that of a reference analyte and correlating this to their relative compositions [9–12]. This approach eliminates the requirement to determine some of the sample or instrumental parameters, as they are treated as constant throughout the calibration. Caumon et al. [9] employ this strategy to compute the equilibrium compositions of the gas and liquid phases of the carbon dioxide-water system. Studies by Ziparo et al. [12] and Li et al. [13] also employ a similar approach in determining the hydrogen solubility in water. A modified version of this approach has been developed to determine the ortho to para ratio in molecular hydrogen at varying temperature conditions [14]. This modified approach includes a factor which accounts for the anisotropy of the polarizability tensor for the hydrogen nuclear spin isomeric forms. Jeong et al. [15] employed Raman spectroscopy to quantify the CO_2 adsorption capacities of various materials. Their approach involves the introduction of refractive index-based correction factors to evaluate composition.

The ratio method is successful in several cases, however, its main limitations are that it relies on the presence of a reference analyte and is not extensible to other mixtures which may contain other compounds. In multicomponent mixtures, there may be an overlap of Raman scattering bands from several components, culminating in a difficulty in resolving the peak areas of the reference analyte. Additionally, in cases where there are transitions to multiple nuclear spin isomeric forms such as in H_2, the changes in peak area may not reflect changes in content, especially at low temperatures. Vitally, a key assumption in this approach relies on the relative RSCS

of the reference analyte and the species of interest being constant across temperature and pressure conditions. However, Ge et al. [16] showed that the relative RSCS can be highly temperature-sensitive in some cases and can also be influenced by the composition of other components in a mixture [17].

Accordingly, the objectives of the present study were twofold. First, it was to assess the feasibility of applying the ratio method to quantify the water content of CO_2, N_2, and H_2. Secondly, it was to explore a quantitative method for the determination of water content that utilises water-only Raman spectra features, using the well-understood CO_2-water binary mixture as a calibration system. The efficacy of this quantitative method was evaluated through its application to the N_2-water, and H_2-water binary mixtures. This investigation was performed at vapour liquid equilibrium conditions over wide ranges of temperature and pressure conditions. The immediate potential application of this quantitative approach would be in equilibrium water content measurements of compressed H_2-rich streams, which is inadequately investigated, and in the monitoring of dehydration processes of CO_2, N_2, and H_2 rich streams.

5.2 Materials and Methods

In this study, Raman spectroscopy measurements were made on the vapour phase of the CO_2-D_2O, N_2-D_2O, and H_2-D_2O systems. D_2O was used in place of H_2O due to the limited spectral range of the employed Raman spectrometer, as detailed in section 5.2.1. The chemicals used in the study are presented in Table 5.1.

Table 5.1: Description of chemical samples used in the study.

Chemical name	CAS number	Source	Purity
D_2O	7789-20-0	Merck, United Kingdom	99.9%
CO_2	124-38-9	BOC, United Kingdom	99.995%
N_2	7727-37-9	BOC, United Kingdom	99.998%
H_2	1333-74-0	BOC, United Kingdom	99.9995%

Isothermal equilibrium experiments were performed under the conditions listed in Table 5.2 with the Raman probe aligned with the gas phase of the two-phase sample. The applicability of the ratio method on the quantification of the water content of the CO_2-D_2O, N_2-D_2O and H_2-D_2O systems was assessed. Raman scattering

measurements of pure D_2O were performed to compare the spectra of its gas and liquid phases. Analysis from the CO_2-D_2O experiments was utilised to develop appropriate correlations for the prediction of the water content in the N_2-D_2O and H_2-D_2O system vapour phases. Experiments were conducted such that they are within ±0.5 MPa of the pressure listed in Table 5.2, to enable a reasonable qualitative comparison of experiments within the same pressure region.

Table 5.2: Conditions at which isothermal experiments are performed.

System	Temperature (K)	Pressure (MPa)
CO_2-D_2O	313.15, 333.15, 353.15	5.0, 8.0, 10.0, 12.5, 15.0
N_2-D_2O	373.15, 393.15	5.0, 10.0, 12.5, 15.0
H_2-D_2O	373.15, 393.15	5.0, 10.0, 12.5, 15.0
D_2O (l)	298.15 K	-
D_2O (g)	373.15 K	-

5.2.1 Experimental setup

Raman scattering measurements were carried out with the apparatus shown in Figure 5.1. This used a 10 ml jacketed equilibrium cell, designed by Videnberg et al. [18] and constructed from titanium alloy grade 5. One end of the cell was closed by a sapphire window assembly comprising a sapphire cylinder (20 mm diameter x 13 mm thick) inserted within a threaded titanium ring as shown in Fig. 1 (insert). The sapphire was thermally bonded to the titanium ring using a polymer film (DuPont Kapton 200FN919) comprising a 25 μm thick polyimide layer sandwiched between two 12.5 μm thick layers of thermosetting fluorinated ethylene propylene. The threaded window assembly screwed into the body of the cell and was sealed with a PTFE primary o-ring and a Viton secondary o-ring. The procedure that was followed to thermoset the sapphire window is outlined in Appendix A. The cell had a maximum working pressure of 70 MPa at a maximum working temperature of 200 ˚C. The cell temperature was measured with a calibrated Platinum Resistance Thermometer (PRT, Fluke model 5618B-6) which was inserted into an axial hole bored in the wall of the vessel. The cell was embedded in an insulated aluminium jacket fitted with four electric cartridge heaters, inserted into axial holes, and a PRT which was used with a process controller to maintain a constant temperature. The overall standard uncertainty of the cell temperature was estimated to be 0.05 K. The pressure was measured in the cell with a pressure transducer (Keller, 70 MPa full scale), which had

a standard uncertainty of 0.02 MPa. The agitation of the cell contents was regulated with a magnetic stirrer motor control unit positioned beneath the cell.

A Raman probe (InPhotonics Inc., model RIP-RPB-785-FC-SMA) fitted with a telescopic objective lens (65 mm working distance) was mounted on a three-axis stage. For this study, the probe was set to a fixed height, such that only the vapour phase was analysed. The positioning of the laser is described in Appendix B. The source was a GaAs diode laser (Innovative Photonic Solutions, USA) which generated an incident light of wavelength 785.26 nm with an intensity of up to 0.5 mW, linked to the probe via an optical fibre. The laser was operated in continuous mode. The Raman probe collected backscattered radiation which was passed to the spectrometer by an optical fibre. An opaque enclosure was used to ensure laser safety.

The Raman spectrometer (QE-Pro Raman, Ocean Optics) could detect Raman shifts in the range 233 cm^{-1} and 3052 cm^{-1} with a pixel resolution between 2 and 4 cm^{-1}, with the resolution nearing 2 cm^{-1} at higher Raman shifts. Since the symmetric O-H stretch, the most pronounced feature in the Raman spectrum of H_2O, falls above 3000 cm^{-1}, deuterium oxide (D_2O) was utilised in all experiments. This is since for D_2O, the gas-phase symmetric O-D stretch falls at approximately 2650 cm^{-1}, which is well within the working range of our instrument.

The spectrometer had a maximum integration time of 1h and an intensity count cap on each CCD channel. Long integration times were required to detect D_2O at low concentrations in the vapour phase, but this could lead to other spectral regions saturating. These limitations influence the resolution of low-concentration components and the observation of components at a high concentration. This is discussed further in section 5.2.3.

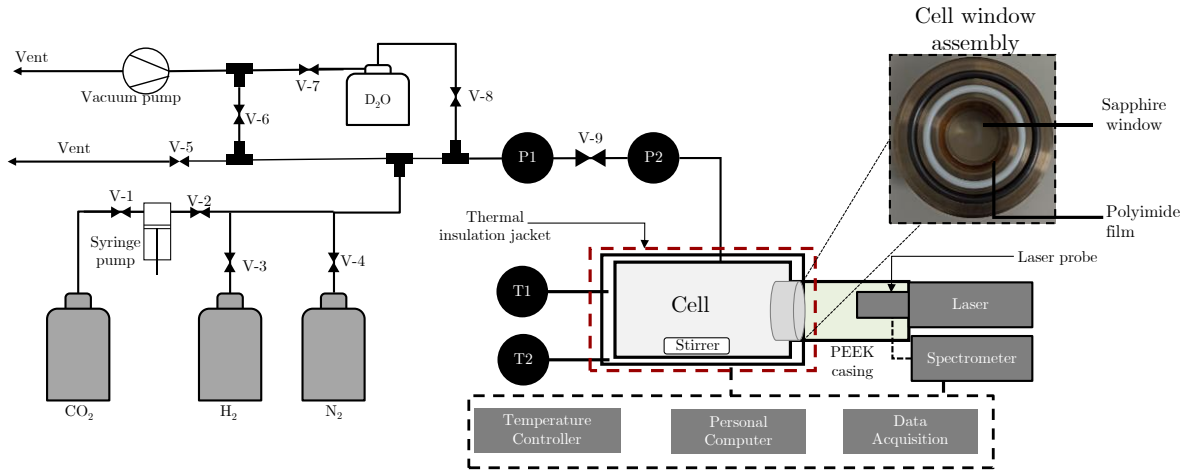

Figure 5.1: Schematic of the in-situ Raman spectroscopy setup, with the cell window assembly (inset). P1 and P2 are pressure sensors, T1 and T2 are temperature sensors, and equipment labelled with V- are manual valves.

5.2.2 Experimental procedure

The experimental procedure consisted of two main steps: Background scanning and Raman scattering measurements.

Background scans

Background scans of the cell were performed prior to each isothermal run. These were performed by flushing the cell with nitrogen and raising the cell temperature to the desired experiment temperature. The cell was then evacuated for an hour and background Raman scans were collected at integration times of 50s, 100s, 1000s, and 3600s.

Raman scattering measurements

The bottle containing the D_2O (see Figure 5.1) was evacuated with stirring to expel dissolved gases. Following this, the vacuum was relieved and about 1 mL of D_2O was drawn into the evacuated cell through valves V-8 and V-9. The cell was then further evacuated. Next, the gas under study (CO_2, N_2 or H_2) was admitted to the cell at an initial pressure of approximately 5 MPa. Following this, the cell was isolated by closing all valves, and the contents were agitated with the magnetic stirrer bar. Stirring was then halted and, once the pressure and temperature had stabilised, Raman spectra were collected at integration times of 50s, 100s, 1000s, and 3600s. Additional gas was then introduced to the cell up to the desired pressure of interest. In the case of CO_2, a refrigerated syringe pump was used to reach the desired

pressure. The previous steps were then followed to collect Raman spectra at the new pressure.

5.2.3 Raman Spectra Analysis

To derive compositional or density correlations based on Raman spectra features, the measured Raman bands were initially fitted with both Gaussian and Lorentzian functions. Across all experiments, it was established that the Lorentzian function provided the best fit of the measured data, and this function was therefore employed in all cases to obtain the peak position wavenumber, amplitude, and the Full Width at Half Maximum (FWHM) intensity. For analysis of the CO_2, N_2, and H_2 Raman active regions, the spectra collected at an integration time of 50s were utilised. For D_2O, the spectra collected at an integration time of 3600s were employed, which provided a high signal-to-noise ratio.

Ratio method calibration

According to Placzek's polarizability theory [8,16], the Raman peak area A_i, of a specific spectral line of component i is given by

$$A_i \propto \int_{\nu_1}^{\nu_2} \eta_i I_{\mathrm{L}} \sigma_i C_i \, \Omega \, \mathrm{d}\nu \tag{5.1}$$

where I_L and Ω are, respectively, the irradiance of the laser and the instrumental solid angle. Additionally, C_i and σ_i are respectively the volumetric concentration and the absolute RSCS for the given spectral feature of component *i*. RSCS describes the scattering efficiency of the molecular rotational or rotation-vibrational transition and η_i is the efficiency at which the scattered light is collected and measured. The irradiance of the laser was kept constant throughout all experiments, and the solid angle was also assumed to be constant across all temperature and pressure conditions. Therefore, according to Placzek's ratio method, the relative concentrations of Raman active components a and b can be related as follows:

$$\frac{A_a}{A_b} = \frac{\sigma_a \eta_a}{\sigma_b \eta_b} \cdot \frac{C_a}{C_b} = \frac{\sigma_a^*}{\sigma_b^*} \cdot \frac{y_a}{y_b} \tag{5.2}$$

Here, σ^* is the apparent RSCS [9], and the concentration ratio is equivalent to the mole-fraction ratio of components a and b. Equation (5.2) represents the key equation of the ratio method. The extent of applicability of equation (5.2) to the binary systems investigated in this work is explored.

Computation of vapour mole fraction and volumetric concentration

In this study, the vapour mole fraction of D_2O, y_{D_2O}, was computed using equations of state (EoS) relevant to the three binary systems. As there is only a minute difference in the vapour pressure of D_2O and H_2O [19], it was assumed that D_2O would have a similar solubility to H_2O in CO_2, N_2, and H_2. Therefore, for the CO_2-D_2O and N_2-D_2O systems, y_{D_2O} was determined using EoS developed by Gernert and Span [20]. For the H_2-D_2O system, work from [20] Kunz and Wagner [21] was used to compute y_{D_2O}.

The vapour phase volumetric concentration of D_2O, C_{D_2O}, was computed from the equation:

$$C_{D_2O}(T,p) = y_{D_2O}(T,p)\,\rho(T,p). \tag{5.3}$$

Under the conditions specified in Table 5.2, water has a low equilibrium mole fraction in the vapour phase and therefore has a negligible impact on the vapour phase density. Consequently, the vapour phase density, $\rho(T,p)$, was determined based on the density of the bulk gas (CO_2, N_2, H_2) at the measured temperature and pressure conditions, computed with the Span-Wagner EoS for CO_2 [22], Span et al. EoS for N_2 [23], and the Leachman et al. EoS for H_2 [24].

5.3 Results

5.3.1 Differences between liquid and vapour phase D_2O Raman spectra

Amongst water's vibrational modes, the symmetric O-H (O-D) stretch, v_1, is the most Raman active [2–5]. Figure 2 shows the Raman spectrum of liquid D_2O measured at 298.15 K, in the region of the symmetric O-D stretch. The spectrum exhibits similar features as that of liquid H_2O [5], with those of D_2O occurring at lower wavenumbers due to the heavier deuterium atoms.

It can be observed that the symmetric O-D stretch band of liquid D_2O is non-symmetric, broad and extends the wide range between 2150 and 2800 cm^{-1}, and has two distinct peaks at 2379 cm^{-1} and 2475 cm^{-1}. The broadness of the spectrum in this region is due to the rich hydrogen bonding network across D_2O molecules. Hydrogen bonding weakens the symmetric O-D stretching because the D_2O structure constitutes the formation of O-D--O bridges across molecules [4], yielding various extents of O-D stretching. Therefore, the broad D_2O spectrum in this region reflects the distribution of various levels of hydrogen bonding across liquid D_2O.

In Figure 2, these various levels of hydrogen bonding, have culminated in the spectrum deconvolution into five Lorentzian elements, with central wavenumbers 2368, 2427, 2493, 2556, and 2636 cm^{-1}. The shoulder between 2630 and 2640 cm^{-1}, also observed in other studies [2,5], has been associated with the fraction of non-hydrogen bonded O-H (O-D) segments in the fluid.

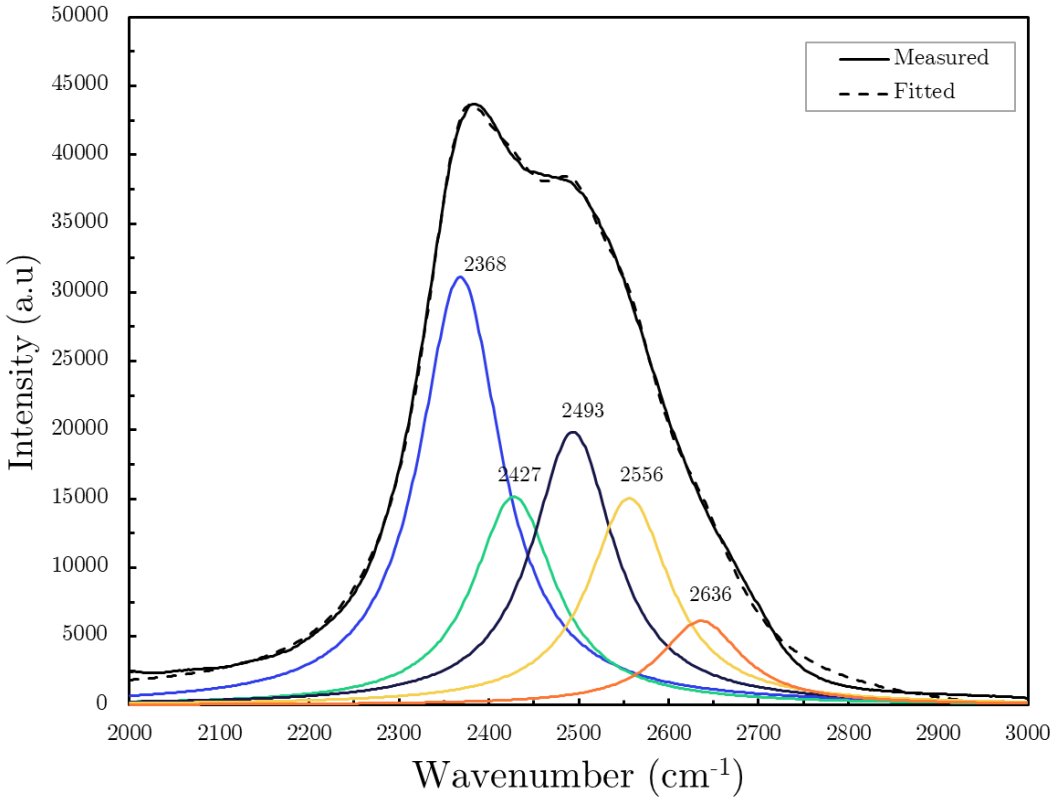

Figure 2: Deconvoluted Raman spectrum of liquid D_2O at 298.15 K.

To resolve the pure D_2O vapour phase Raman band, the integration time was identified as a key instrumental variable that impacts the identification of D_2O in the vapour phase. Raman spectra of vapour phase D_2O were collected at integration times in the range of 50s up to 3600s (1h), shown in Figure 3. Increasing the integration time enables the observation of a distinct vapour phase D_2O peak, and also improves the signal-to-noise ratio. Consequently, for binary system experiments of CO_2-D_2O and H_2-D_2O, the analysis of the O-D symmetric stretch band was performed for spectra collected at an integration time of 3600s.

In comparison to the liquid phase D_2O spectrum, at 373.15 K, the vapour phase spectrum is narrow, with one distinct peak. The narrower spectrum and positive shift of the band centre are due to differences in the extent of intermolecular interactions in the liquid and vapour phases. Molecules in the liquid phase experience stronger

intermolecular interactions and a complex interaction environment, which yields a broad distribution of Raman scattered photons. In contrast, the reduced hydrogen bonding environment in the vapour phase culminates in the shift of central peak wavenumber to 2663.8 cm^{-1}. This perhaps, reflects the higher fraction of non-hydrogen bonded O-D segments in the vapour phase.

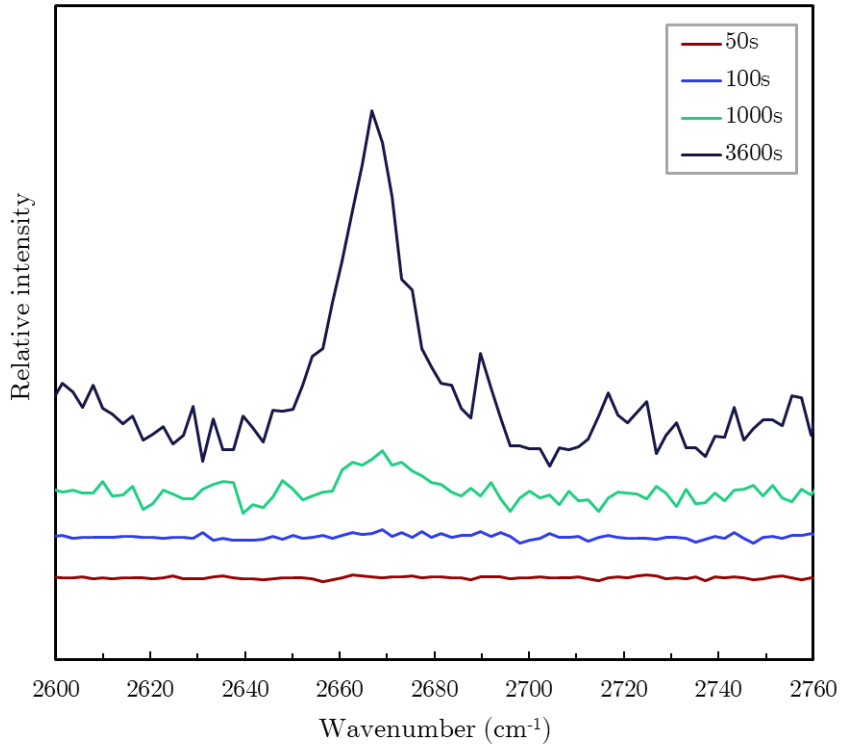

Figure 3. The effect of integration time on the resolution of pure gas phase D_2O at 373.15 K.

5.3.2 Bulk gas region in CO_2-D_2O, N_2-D_2O, and H_2-D_2O

Isothermal Raman scattering measurements of the CO_2-D_2O, N_2-D_2O, and H_2-D_2O vapour phases, coexisting with a D_2O-rich liquid phase, were performed at pressures ranging from 5 to 15 MPa. Figure 5.4 presents typical isothermal CO_2-D_2O, N_2-D_2O, and H_2-D_2O vapour phase spectra.

The CO_2 region spectrum is a Fermi diad, which arises from the interaction of the fundamental ν_1 band and $2\nu_2$ overtone [25,26]. This yields two prominent peaks at approximately 1280 and 1384 cm^{-1}, which are labelled as low frequency, v^- , and high frequency, v^+ , respectively. As can be observed in Figure 5.4, these prominent peaks are accompanied by smaller hot bands. N_2 has only one fundamental vibrational-rotational band in the spectral range covering the range 2300 to 2350 cm^{-1}. For H_2, four distinct pure-rotational transitions can be observed in the region between 300

to 1200 cm^{-1}. The peaks at 351 and 814 cm^{-1} correspond to para-hydrogen (even rotation quantum number), while the peaks at 583 and 1031 cm^{-1} correspond to rotational modes of ortho-hydrogen (odd rotation quantum number) [13].

All the Raman bands demonstrate pressure sensitivity, characterised by peak broadening, and increasing intensities with increasing pressure. This is largely due to a rise in density with pressure, which culminates in more molecules interacting with the incident laser in the scattering volume. For CO_2, a distinct escalation in intensity is observed between pressures 7.8 and 10.3 MPa, which corresponds to a rapid rise in density.

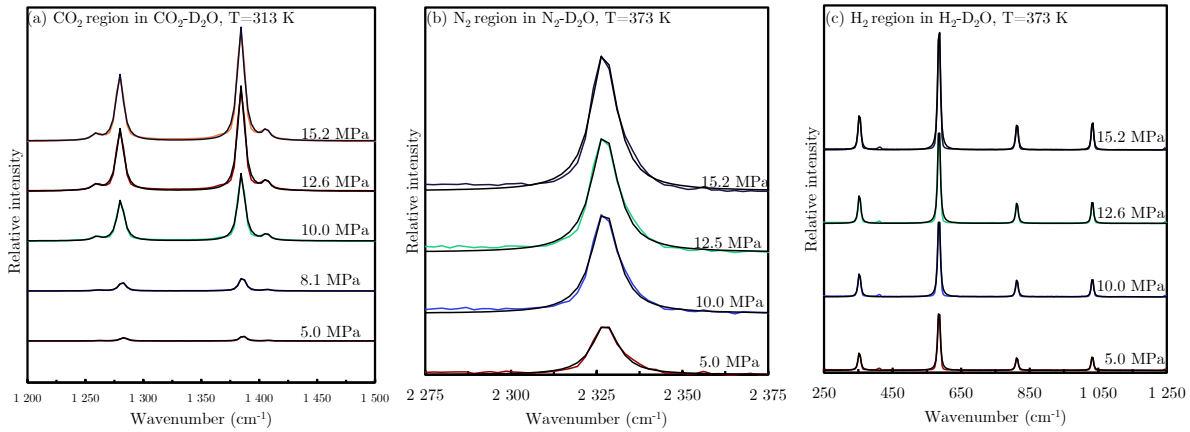

Figure 5.4: Isothermal Raman Spectra of the (a) CO_2, (b) N_2, and (c) H_2 regions for the CO_2-D_2O, N_2-D_2O, and H_2-D_2O vapour phases at various pressures. Each spectrum was collected at an integration time of 50s.

Furthermore, it was observed that the change in density of the vapour phase influences the band centres of the CO_2 Fermi diad components. Figure 5.5 presents the band centres of the v^- and v^+ CO_2 bands at the respective molar densities. Overall, the Raman spectrum in the CO_2 region shifts towards lower wavenumbers with the rise in density across all isothermal conditions. Vitally, in the experimental conditions, the band centres of the two Fermi dad components have a strong linear response with changes in density, with the v^- band being the most sensitive to density. Li et al. [27] showed that a similar density correlation can be observed across all phases of pure CO_2. As the Fermi diad components emerge from the interaction of the fundamental ν_1 band and the $2\nu_2$ overtone, their band centre shifts with density occur either due to alterations in the unperturbed excited levels of these vibrations and/or changes in their Fermi coupling constant [28]. These changes are influenced by temperature and density conditions which affect intermolecular forces,

intermolecular distances, and molecular collisions [27]. Figure 5.5, which also includes band centres of pure CO_2, indicates that the presence of D_2O in the vapour phase has a negligible impact on the band centres of the two major CO_2 Fermi-diad components. This shows that, at the conditions of the experiments, the band centres of the Fermi-diad components can be correlated with the CO_2-D_2O vapour phase density.

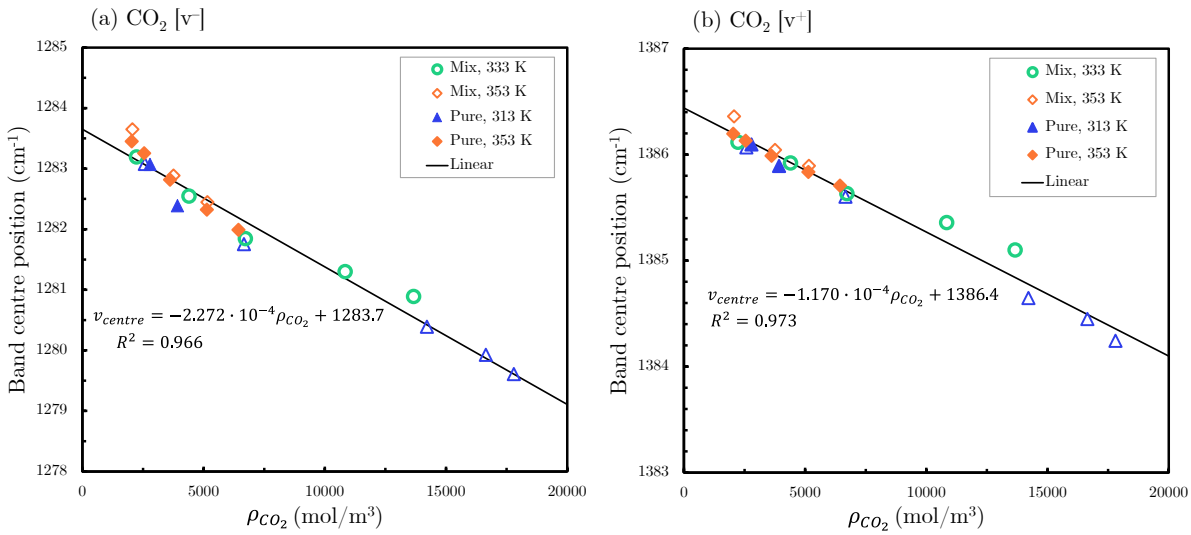

Figure 5.5: Correlation of the major CO_2 Fermi diad components band centres with CO_2 density over a range of temperature and pressure conditions. Open shapes indicate measurements taken in the presence of D_2O, while filled shapes indicate pure CO_2 measurements.

5.3.3 D_2O Raman band in CO_2-D_2O, N_2-D_2O, and H_2-D_2O

Amongst water's vibrational modes, the symmetric O-H (O-D) stretch, ν_1, is the most Raman active [29–32]. In the binary systems, the D_2O ν_1 peak was observed within the wavenumber range of 2600 to 2700 cm^{-1}. The spectral parameters measured are given in Table 5.3. It should be noted that the parameters presented in Table 5.3, while repeatable in our apparatus, would differ if measured with another apparatus or analysed with a different fitting approach.

Table 5.3 shows that the position of the D_2O ν_1 peak varies significantly across the binary systems, with the CO_2-D_2O system having the greatest variations. Generally, it can be observed that at isothermal conditions, the D_2O ν_1 peak position shifts to lower wavenumbers with an increase in pressure.

Table 5.3: Parameters of the Lorentzian fit for conditions where the D_2O v_1 symmetric stretch could be observed for the Raman spectra of the CO_2-D_2O, N_2-D_2O, and H_2-D_2O vapour phases.

Temperature (K)	Pressure (MPa)	Amplitude (a.u)	FWHM (cm^{-1})	D_2O ν_1 peak position (cm^{-1})
CO_2-D_2O				
313.18	8.13	124318	16.25	2661.99
313.19	9.97	473684	14.87	2657.84
313.18	12.56	715085	14.09	2656.68
313.18	15.22	864291	13.87	2656.10
333.13	5.00	81547	21.02	2666.31
333.13	8.05	154238	15.86	2663.80
333.18	10.10	321962	14.78	2661.81
333.12	12.57	650616	14.34	2659.25
333.14	14.92	1134697	13.96	2657.99
353.16	5.12	98763	29.72	2667.04
353.16	8.17	401353	14.87	2663.99
353.15	10.15	530778	14.20	2663.07
353.16	12.76	842876	14.19	2661.36
353.17	15.00	1267394	14.03	2660.01
N_2-D_2O				
373.17	5.04	40306	11.93	2667.14
373.20	10.01	50997	13.44	2665.99
373.09	12.48	60599	15.20	2665.77
373.08	15.16	60787	15.08	2665.20
393.19	5.09	158999	14.29	2666.87
393.16	10.19	408087	13.78	2666.30
393.17	12.57	532220	13.74	2666.25
393.10	15.17	551377	13.54	2665.89
H_2-D_2O				
373.28	5.02	278829	14.41	2667.42
373.22	10.01	165068	14.20	2666.98
373.22	12.57	146023	14.45	2667.01
373.12	15.03	163476	15.85	2666.65

Temperature (K)	Pressure (MPa)	Amplitude (a.u)	FWHM (cm^{-1})	D_2O ν_1 peak position (cm^{-1})
393.24	5.06	687041	14.63	2667.14
393.24	9.97	712428	14.48	2666.96
393.25	12.53	737854	14.77	2666.91
393.23	14.70	733351	14.50	2666.81

5.3.3.1 CO_2-D_2O

Figure 5.6 presents the isothermal Raman spectra at various pressures for the CO_2-D_2O vapour phase in the region of the D_2O ν_1 peak, with the intensity axis plotted at the same scale across the three temperature conditions. Figure 5.6 shows that for each isothermal condition, the height of the peak rises with pressure. Consequently, there is a positive relationship between the pressure and peak area at each isothermal condition as presented in Table 5.3. According to equation (5.1), this would suggest that at each isotherm, the volumetric concentration of D_2O in the vapour phase rises with pressure.

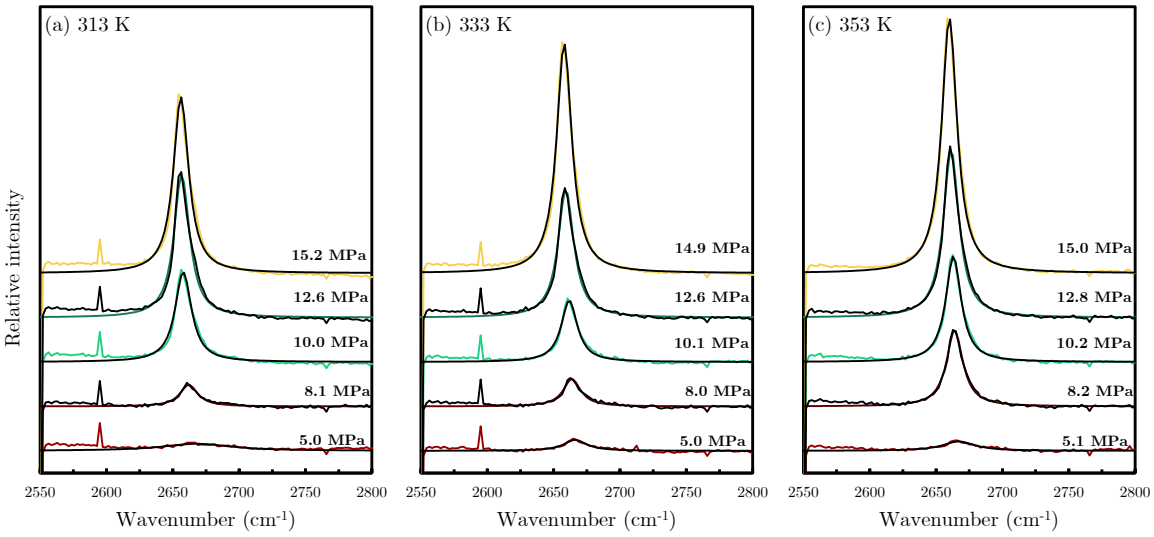

Figure 5.6: Isothermal Raman spectra of O-D symmetric stretch region for CO_2-D_2O system at various pressures. The Lorentzian fit of each peak is shown in black.

Furthermore, Figure 5.6 also reveals three trends across the isothermal experiments. To begin with, at 5.0 MPa, a distinct peak for the symmetric O-D stretch is not resolved at 313 K, however, this peak can be observed at higher temperatures. Secondly, at all corresponding pressures, the peaks at 353 K, have the greatest intensity (see peak amplitude in Table 5.3). Lastly, at approximately 10 MPa, the peak

rises and falls across the isotherms, being intense at 313 K, diminishing at 333 K, and finally rising again at 353 K.

To a limited extent, the three trends can be attributed to variations in volumetric concentration. Figure 5.7 shows the evolution of the isothermal volumetric water concentration in the CO_2-rich vapour phase with pressure. As presented in equation (5.3), the volumetric concentration of D_2O is the product of the interplay between the D_2O vapour mole fraction and the density of the vapour phase, which both rise rapidly as CO_2 transitions from the gas phase to the supercritical phase [33]. At a low pressure of 5 MPa, the volumetric concentration of D_2O in the carbon dioxide vapour phase is the lowest for each isotherm, culminating in the weak resolve of the O-D symmetric stretch peak at 333 K. At pressures above 8 MPa, the volumetric concentration of D_2O is highest for the 333 K isotherm, however, it has the lowest Raman response (see peak amplitude in Table 5.3). Based on equation (5.1), these observations suggest that there are significant variations in the apparent RSCS of the D_2O ν_1 stretch across the three isotherms. This is further elaborated on in section 5.4.1.

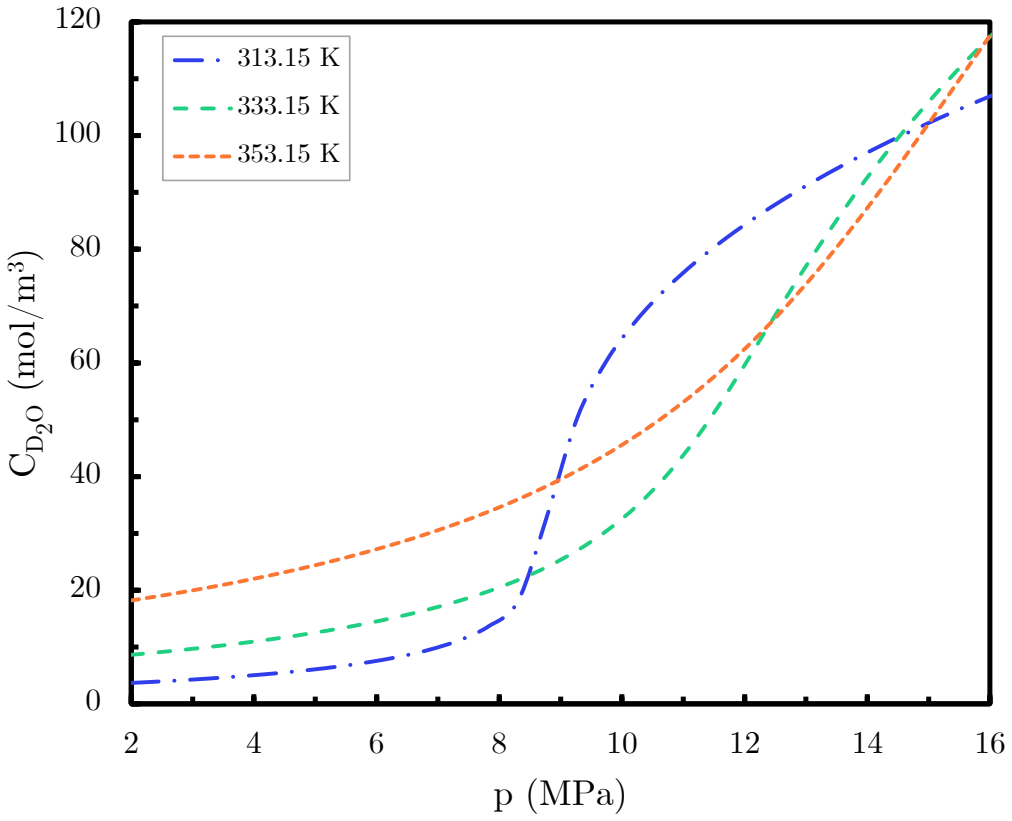

Figure 5.7: Isothermal equilibrium D_2O volumetric concentrations in the CO_2-rich phase as a function of pressure. The volumetric concentration was computed using equation (5.3).

5.3.3.2 N_2-D_2O and H_2-D_2O

Isothermal experiments for the N_2-D_2O and H_2-D_2O systems were conducted at 373 and 393 K, and at pressures between 5 and 15 MPa. The characteristic spectra of the D_2O ν_1 peak for both systems are shown in Figure 5.8. Similar to the CO_2-D_2O system, the D_2O ν_1 peak can be observed in the range 2600 and 2750 cm^{-1}.

Across the isothermal experiments, the peak intensity increases with pressure, indicating a rise in the volumetric concentration of the gas phase (see also Table 5.3). The primary exception to this is the spectrum obtained at 373 K and 5.0 MPa for the H_2-D_2O system, which has a higher peak area relative to the other pressure conditions. Table 5.3 and Figure 5.8 also show a significant rise in the peak areas with a temperature rise. Furthermore, Table 5.3 highlights that the D_2O ν_1 peak position in the N_2-D_2O and H_2-D_2O systems change with temperature and pressure, and is significantly lower than those observed for the CO_2-D_2O system at the experimental conditions.

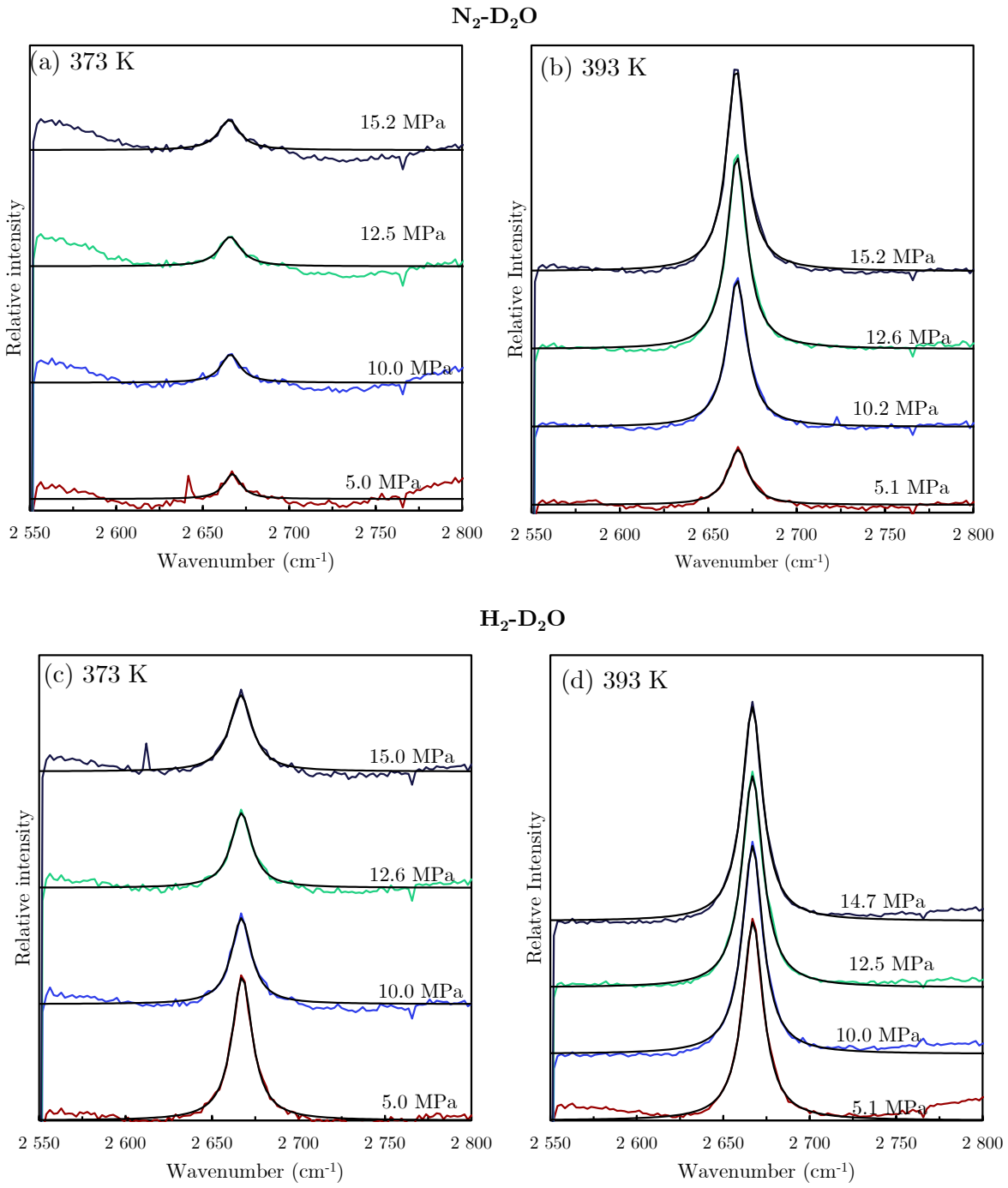

Figure 5.8: Isothermal Raman spectra of O-D symmetric stretch region for N2-D2O (a), (b), and H_2-D_2O (c), (d). The Lorentzian fit of each peak is shown in black.

5.4 Discussion

5.4.1 Investigating the applicability of the ratio method calibration model

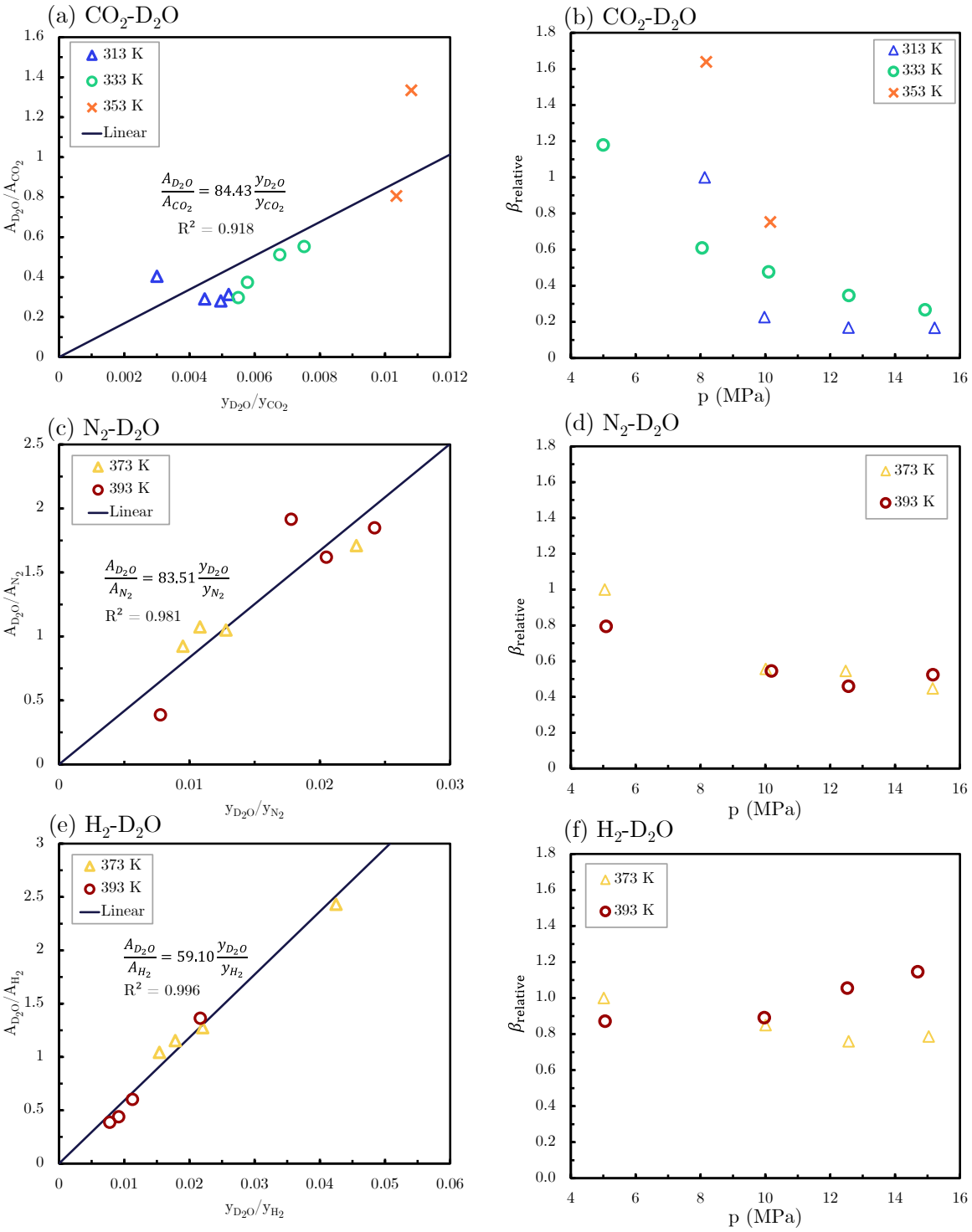

Figure 5.9: (a),(c),(e) Relative band areas plotted with relative composition of D_2O and bulk gases; (b),(d),(f) $\beta_{relative}$ plots for binary systems reflecting the influence of pressure and temperature.

From equation (5.2), for the peak area ratios to be proportional to the relative volumetric concentration of components a and b, the apparent RSCS of the two components should be constant or change at the same rate across all temperature and pressure conditions. Figure 5.9 (a), (c), (e) apply equation (5.2) based on the assumption that the relative apparent RSCS is constant across all conditions. The H_2-D_2O system has good agreement with the linear model, while the CO_2-D_2O and N_2-D_2O systems have significant scatter and thus yield poor calibration results. The CO_2-D_2O results are consistent with Caumon et al. [9] where a poor direct correlation between the area ratio and relative concentrations vapour phase was observed.

Insight into the poor correlation could be gained by assessing the temperature and pressure sensitivity of the relative apparent RSCS in equation (5.2). Here an approach described by Ge et al. [16] and Wu et al. [17] is followed. From equation (5.2), the relative apparent RSCS is defined as the quantification factor (β) presented in equation (5.4). β can be determined from the band area of the O-D symmetric stretch and the specific band area of the bulk gases CO_2, N_2, and H_2, and their relative vapour phase mole fractions. The band area of the bulk gases was computed from their respective Raman active regions described in section 5.3.2, while the equilibrium mole fraction at each condition is determined from an EoS as per section 5.2.3.

$$\beta(T,p) = \frac{\sigma^*_{D_2O}(T,p)}{\sigma^*_{bulk}(T,p)} = \frac{A_{D_2O}(T,p)}{A_{bulk}(T,p)} \cdot \frac{y_{bulk}(T,p)}{y_{D_2O}(T,p)} \tag{5.4}$$

To enable an analysis of the effect of temperature and pressure on β, a new parameter $\beta_{relative}$ is introduced. $\beta_{relative}$ is a normalisation of each quantification factor by the $\beta(T_{low}, p_{low})$, which is the quantification factor determined at the lowest pressure and temperature experiment for each binary mixture. In a general sense, $\beta_{relative}$ represents, for a fixed D_2O volumetric concentration, the extent to which the Raman response of the D_2O ν_1 peak will change with changes in temperature and pressure.

$$\beta_{relative}(T,p) = \frac{\beta(T,p)}{\beta(T_{low}, p_{low})} \tag{5.5}$$

Figure 5.9 (b), (d), (f) illustrates that across the binary systems, $\beta_{relative}$ trends systematically with temperature and pressure, although to varying degrees. In the CO_2-D_2O system, pressure and temperature have a significant impact on $\beta_{relative}$, with a decline observed with increasing pressure and an increase with rising temperatures. This indicates that lower temperatures and higher pressures diminish the Raman response compared to conditions at higher temperatures and lower pressures at the

same D_2O volumetric concentrations. A major contribution to this is likely due to a sharp alteration in the refractive index of the CO_2 rich vapour phase, as CO_2 shifts from the gas phase to the supercritical phase as pressure rises. Jeong et al. [15] addressed this in their study by introducing a refractive index factor when analysing data from CO_2 adsorption experiments, and successfully accounted for changes in the apparent RSCS. In their experiments of the CO_2-water system, Caumon et al. [9] also noted that condensation would occasionally occur on the window of their cell, which may affect the collected Raman spectra. However, Figure 5.9 (b) does indicate that the changes in the apparent RSCS are systematic and are not random.

The $\beta_{relative}$ for the N_2-D_2O system also declines with pressure, while temperature has a minimal influence. Conversely, the $\beta_{relative}$ in the H_2-D_2O system is highly sensitive to both temperature and pressure. At temperatures of 373 and 393 K, respectively, $\beta_{relative}$ decreases and increases with a rise in pressure. However relative to the other systems, the overall changes in β of the H_2-D_2O system are within a narrow band. Therefore, for this system, the overall influence of both pressure and temperature is minimal under the experimental conditions, resulting in a direct proportionality between peak area ratios and relative concentrations.

This underscores that the changes in the D_2O v_1 peak areas not only reflect changes in D_2O volumetric concentrations but also stem from variations in the relative apparent RSCS. To improve the ratio method, it may be beneficial to model the changes in $\beta_{relative}$, especially since they exhibit a systematic trend.

5.4.2 The compositional sensitivity of the D_2O v_1 peak centre

Section 5.4.1 has demonstrated the efficacy of the ratio method for calibrating the H_2-D_2O under the investigated conditions. However, this approach is ineffective when applied to the CO_2-D_2O and N_2-D_2O systems, due to notable changes in the relative apparent RSCS with temperature and pressure.

The Raman shift in the symmetric O-H and O-D stretch has been associated with the extent of intermolecular hydrogen bonding [29–32], as discussed in section 5.3.1. This is since hydrogen bonding weakens the symmetric O-D stretching because the D_2O structure forms O-D--O bridges across molecules, thus a positive Raman shift in the symmetric O-H and O-D stretch reflects the breaking of hydrogen bonds [29]. Therefore, in this study, the changes in the hydrogen bonding environment are reflected by a shift in the D_2O v_1 peak centre, which is observed across the binary systems explored in this study. In particular, as presented in Table 5.3, the CO_2-D_2O

system has the largest shift in the peak centre ranging between 2656.1 and 2667.0 cm^{-1}.

Figure 5.10 (a) is a visualisation of the D_2O ν_1 peak centre in the CO_2-D_2O vapour phase at isothermal conditions as a function of pressure. Figure 5.10 (a) highlights two phenomena: (1) hydrogen bond-making with the rise in pressure, (2) hydrogen bond breaking with rising temperature. Elevating the pressure leads to a shift of the D_2O ν_1 stretch towards lower wavenumbers. This pressure sensitivity is further accentuated by higher temperatures, which causes the D_2O v_1 stretch to shift to higher wavenumbers. At the temperature conditions of this study, this shift in the D_2O v_1 peak centre aligns with the work of Oparin et al. [34], where the shift in the O-H symmetric stretch in the CO_2-water system was investigated. Essentially, under isothermal conditions, increasing pressure corresponds to a denser vapour phase and a higher D_2O solubility in CO_2, leading to shorter intermolecular distances between molecules, and stronger hydrogen bonding. Conversely, higher temperatures reduce the fluid density and result in the breakage of hydrogen bonds. Consequently, the D_2O v_1 peak centre declines with the vapour phase density, as presented in Figure 5.10 (b).

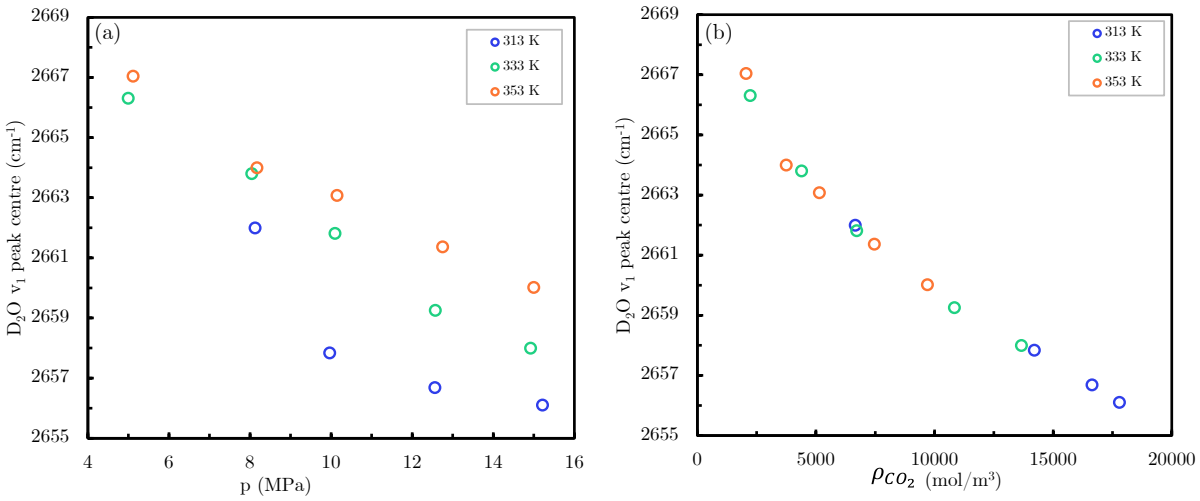

Figure 5.10: D_2O O-D v_1 stretch peak centre as a function of pressure (a) and CO_2 density (b) at isothermal temperatures in the CO_2-D_2O binary system.

5.4.3 D_2O v_1 stretch peak centre as a proxy for water content

As the D_2O ν_1 peak centre indicates the extent of hydrogen bonding across D_2O molecules, this section endeavours to link the D_2O ν_1 peak centre to the vapour phase water content. To achieve this, the CO_2-D_2O binary is used as a calibration system, as it has a wide volumetric concentration range at accessible temperatures and

pressures. Through investigating the relationship between the D_2O ν_1 peak centre and the volumetric concentration, equation (5.6) was arrived at for the conditions investigated in this study.

$$\nu_{\text{centre}} = (a_1 T + b_1) \cdot \left(\frac{C_{D_2O}}{c_1}\right)^{a_2 T + b_2} \tag{5.6}$$

Equation 6 highlights that the D_2O ν_1 peak centres, ν_{centre}, fall on unique isotherms, as presented in Figure 5.10 (a), which is also observed in other studies [30,34,35]. Equation (5.6), further relates the ν_{centre} to the vapour phase volumetric concentration of D_2O, C_{D_2O}, and the thermodynamic temperature T. The fitted parameters are a_1, b_1, a_2, and b_2, while c_1 is a dimensionless factor and is $c_1 = 1\, mol\, m^{-3}$.

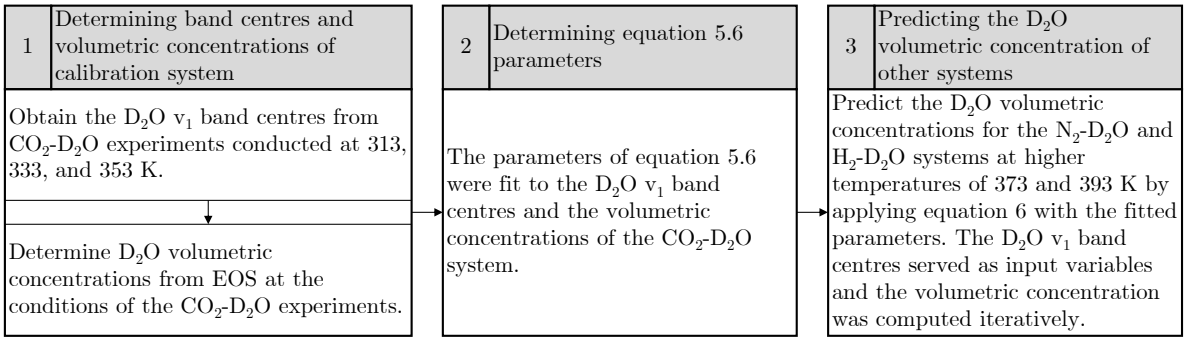

Figure 5.11: The process of parameterising equation (5.6), and prediction of D_2O volumetric concentration for the N_2-D_2O and H_2-D_2O.

Figure 5.12 outlines the process that was followed to parameterise equation (5.6), and the prediction of the D_2O volumetric concentration in the N_2-D_2O and H_2-D_2O systems. Equation (5.6) parameters were obtained by fitting it to the D_2O v_1 stretch peak centres obtained from CO_2-D_2O experiments conducted at temperatures of 313, 333, and 353 K to the calculated D_2O volumetric concentration. Here, the volumetric concentrations were determined from equation 3. The parameters derived from the fitting process were determined as: $a_1 = 1.892 \cdot 10^{-1}\, K^{-1} cm^{-1}$, $b_1 = 2.615 \cdot 10^{3} cm^{-1}$, $a_2 = -6.417 \cdot 10^{-6}\, K^{-1}$, and $b_2 = 5.029 \cdot 10^{-4}$. It is crucial to note that the parameters are specific to the employed experimental apparatus, the Raman band fitting approach employed, and the chosen calibration system. Thus, the parameters need to be fitted for each experimental campaign.

Equation (5.6), which used parameters obtained from the CO_2-D_2O fitting, was then utilised to predict the D_2O volumetric concentration in the N_2-D_2O and H_2-D_2O binary systems based on the O-D symmetric stretch peak centre positions. The result of this

prediction is shown in Figure 5.12, where the model predictions are compared to the calculated volumetric concentrations.

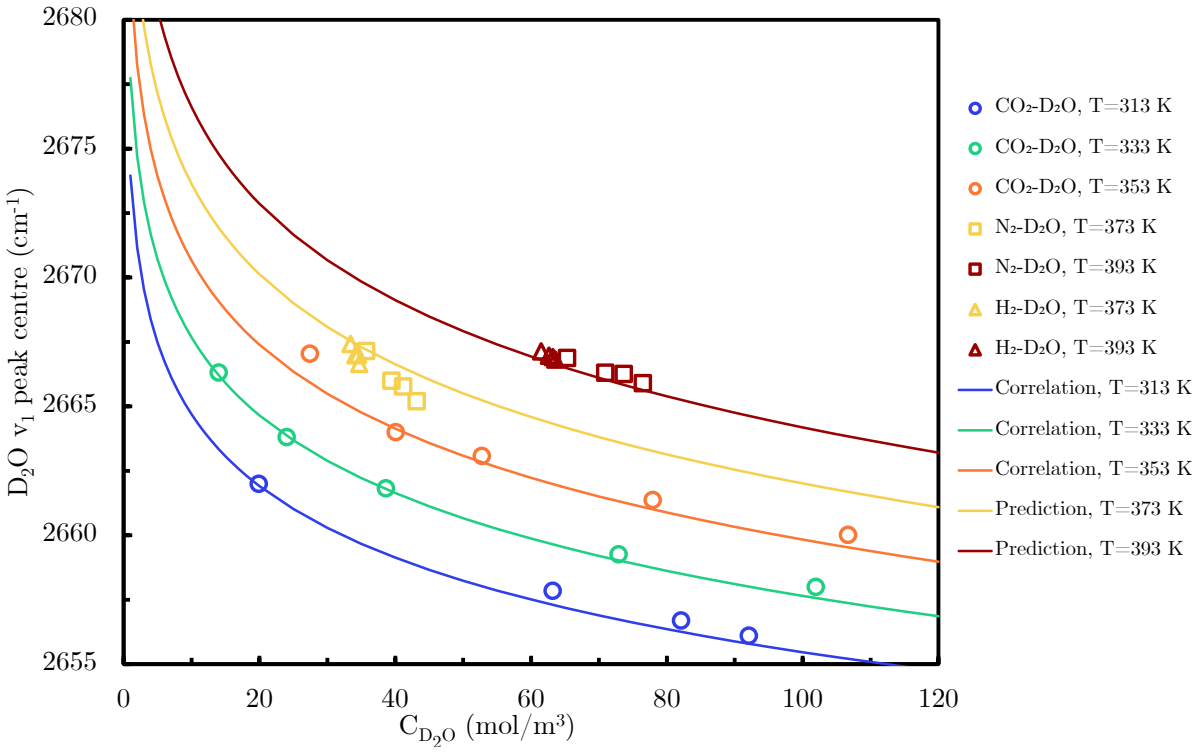

Figure 5.12: Relationship between O-D v_1 peak centre positions and volumetric concentration at isothermal conditions. Lines represent the proposed model with its parameters derived from fitting data from the CO_2-D_2O system. The points are the binary systems' O-D v_1 peak centre positions, with volumetric concentrations obtained from EoS at corresponding temperature and pressure conditions.

The predicted and calculated volumetric concentrations are compared through parity plots presented in Figure 5.13. An overall absolute average relative (AARD) of less than 10% is attained across the N_2-D_2O and H_2-D_2O binary systems. Particularly, low deviations are observed at the 393 K isotherm, along with similarly low deviations observed for the H_2-D_2O system. This underscores the utility of the proposed approach, as it can be used as an internal calibration for a fixed binary system or employed to predict the D_2O volumetric concentrations of other binary systems. In this study, this approach was successfully employed to predict the D_2O volumetric concentration of N_2-D_2O and H_2-D_2O beyond the temperatures covered by the CO_2-D_2O calibration.

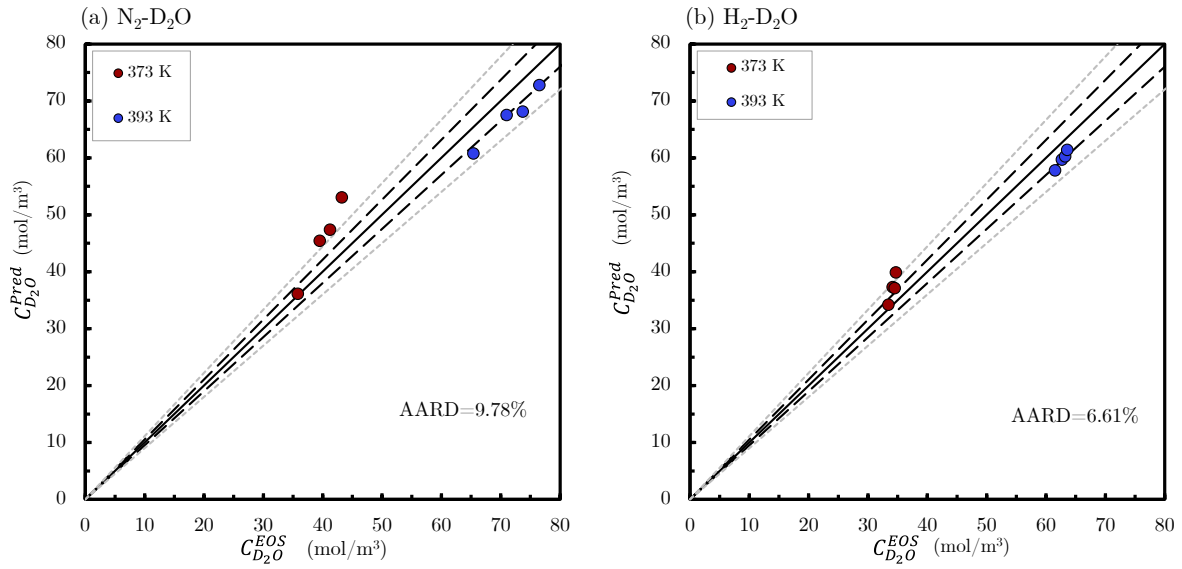

Figure 5.13: Parity plot of the volumetric concentration determined from EoS, and predicted data obtained from peak centre model for the N_2-D_2O and H_2-D_2O systems. Deviation lines for 0% (solid, black), 5% (dashed, black), and 10% (dashed, grey) are shown.

5.4.4 Prediction of vapour mole fraction

The predicted D_2O volumetric concentrations allow for the determination of water mole fraction in both the N_2-rich and H_2-rich vapour phases. The transformation of equation (5.3) to equation (5.7), gives an explicit expression of the D_2O vapour mole fraction. Equation (5.7), highlights that the key constraint in vapour mole fraction determination is the prior knowledge or the computation of the phase density. This could be determined through a correlation of the bulk phase peak area and density, or from accurate thermodynamic models. In cases where equation (5.6) is utilised as a calibration standard for the CO_2-D_2O, this work has demonstrated that the band centre positions of the CO_2 diads can be utilised to compute the CO_2-rich phase density.

$$y_{D_2O}^{predicted}(T,P) = \frac{C_{D_2O,v}^{predicted}(T,P)}{\rho(T,P)} \tag{5.7}$$

Figure 5.14 compares the predicted water mole fractions in the N_2-rich and H_2-rich vapour phases to EoS predictions and available experimental data. The predicted vapour mole fractions are also presented in Table 5.4. Figure 5.14 highlights that there is a close agreement between the predicted water mole fractions and the EoS model and experimental data. Deviations of the predicted water vapour mole fractions may also stem from uncertainties in the EoS models which have been

employed to predict vapour phase density and vapour phase mole fractions. A significant improvement of the proposed approach would be coupling the Raman measurements with direct measurements of the vapour phase density.

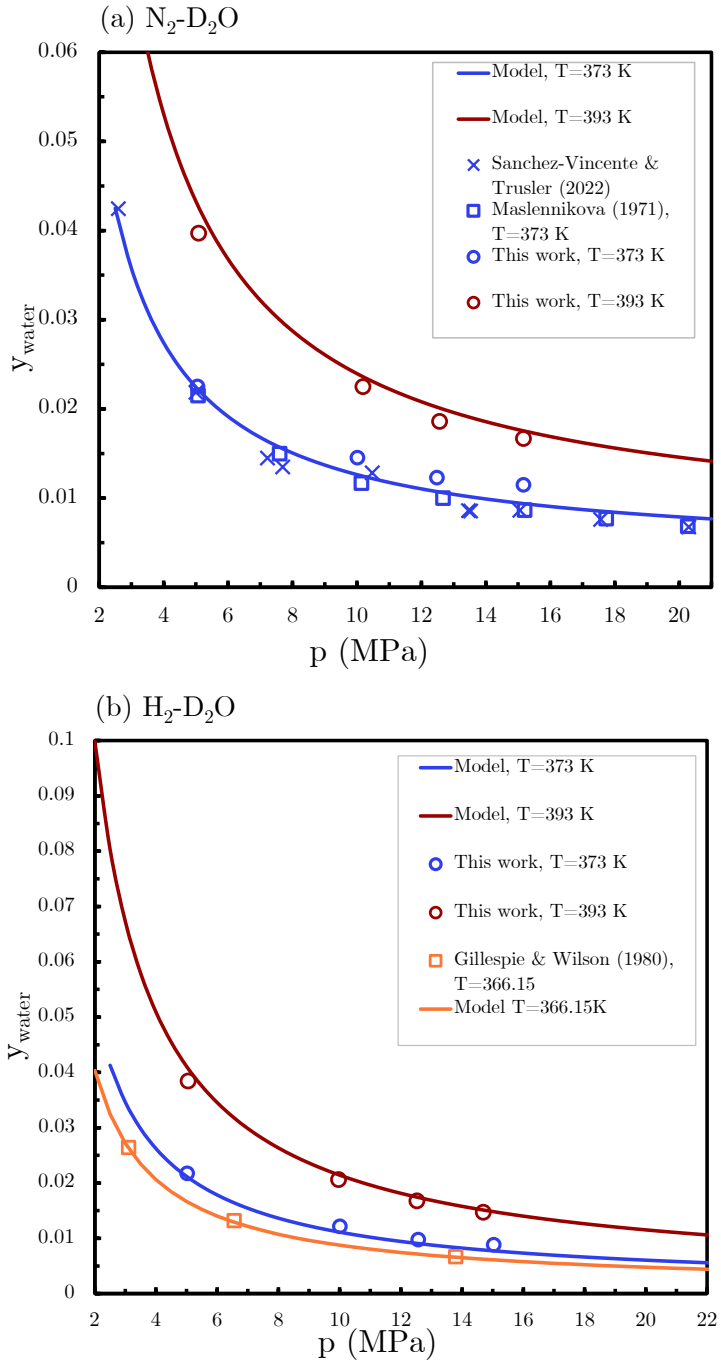

Figure 5.14: Comparison of predicted vapour phase water mole fractions with EoS predictions and experimental data. N_2-D_2O model – Gernert and Span [20], and experimental data from Sanchez-Vincente and Trusler [36], and Maslennikova et al. [37]; H_2-D_2O model - Kunz and Wagner [21] and experimental data from Gillespie and Wilson [38].

Table 5.4: Predicted vapour phase water mole fraction of the N_2-D_2O and H_2-D_2O systems.

Temperature (K)	Pressure (MPa)	y_{water}
N_2-D_2O		
373.17	5.04	0.0225
373.20	10.01	0.0146
373.09	12.48	0.0123
373.08	15.16	0.0115
393.19	5.09	0.0397
393.16	10.19	0.0225
393.17	12.57	0.0186
393.10	15.17	0.0167
H_2-D_2O		
373.28	5.02	0.0218
373.22	10.01	0.0122
373.22	12.57	0.0098
373.12	15.03	0.0089
393.24	5.06	0.0384
393.24	9.97	0.0206
393.25	12.53	0.0167
393.23	14.70	0.0147

5.5 Conclusions

In-situ Raman spectroscopy measurements were conducted for the CO_2-D_2O, N_2-D_2O, and H_2-D_2O vapour phases at a wide range of temperatures, and pressures ranging from 5 to 15 MPa to assess different quantitative approaches for water content determination. In assessing the ratio method, it was found that it could be employed successfully to calibrate the H_2-D_2O system, however, when this method was applied to the CO_2-D_2O and N_2-D_2O binary systems, it yielded significant deviations. This has been demonstrated to be due to the significant pressure and temperature sensitivities of the relative apparent RSCS of the D_2O ν_1 stretch and the respective Raman active regions of the bulk gases across the investigated temperature and pressure conditions.

As an alternative approach, this study provided an explicit correlation linking the D_2O ν_1 stretch peak centre to the D_2O volumetric concentration. Under the studied

conditions, the CO_2-D_2O system was used to calibrate the parameters of this correlation, which culminates in satisfactory predictions of the equilibrium water content of N_2 and H_2 at wide temperature and pressure conditions. This proposed quantitative approach allows for the determination of water content utilising only water-specific Raman features.

This study has illustrated that Raman spectroscopy is a suitable alternative for measuring the water content of high-pressure fluids. Future studies will need to validate the proposed quantitative approach in other fluid mixtures and improve the prediction of density to enable the direct computation of mole fraction based compositions.

Acknowledgements

This work is supported by the European Union's Horizon 2020 research and innovation programme (Grant Agreement No. 838931), Technical University of Denmark, and Otto Mønsteds Fond. The authors thank the Deutsche Forschungsgemeinschaft (DFG, German Research Foundation) who fund the work of C.W. within the Walter Benjamin Fellowship Programme (Grant No. 497236263).

References

[1] I.S. Cole, P. Corrigan, S. Sim, N. Birbilis, Corrosion of pipelines used for CO2 transport in CCS: Is it a real problem?, International Journal of Greenhouse Gas Control 5 (2011) 749–756. https://doi.org/10.1016/j.ijggc.2011.05.010.

[2] S. Adisasmito, R.J. Frank, E.D. Sloan, Hydrates of carbon dioxide and methane mixtures, J Chem Eng Data 36 (1991) 68–71. https://doi.org/10.1021/je00001a020.

[3] X. Lv, W. Li, B. Shi, S. Zhou, Study on the blockage mechanism of carbon dioxide hydrate slurry and its microscopic particle characteristics, RSC Adv 8 (2018) 36959–36969. https://doi.org/10.1039/C8RA07259K.

[4] A.R. Smith, J. Klosek, A review of air separation technologies and their integration with energy conversion processes, Fuel Processing Technology 70 (2001) 115–134. https://doi.org/10.1016/S0378-3820(01)00131-X.

[5] X.R. Wang, Y. Ma, J. Gao, T. Li, G.Z. Jiang, Z.Y. Sun, Review on water management methods for proton exchange membrane fuel cells, Int J Hydrogen Energy 46 (2021) 12206–12229. https://doi.org/10.1016/j.ijhydene.2020.06.211.

[6] R. Dohrn, J.M.S. Fonseca, S. Peper, Experimental Methods for Phase Equilibria at High Pressures, Annu Rev Chem Biomol Eng 3 (2012) 343–367. https://doi.org/10.1146/annurev-chembioeng-062011-081008.

[7] B. Wopenka, J.D. Pasteris, Limitations to Quantitative Analysis of Fluid Inclusions in Geological Samples by Laser Raman Microprobe Spectroscopy, Appl Spectrosc 40 (1986) 144–151. https://doi.org/10.1366/0003702864509592.

[8] G. Placzek, Handbuch der Radiologie, 1934.

[9] M.-C. Caumon, J. Sterpenich, A. Randi, J. Pironon, Measuring mutual solubility in the H 2 O–CO 2 system up to 200 bar and 100 °C by in situ Raman spectroscopy, International Journal of Greenhouse Gas Control 47 (2016) 63–70. https://doi.org/10.1016/j.ijggc.2016.01.034.

[10] Brigitte. Wopenka, J.Dill. Pasteris, Raman intensities and detection limits of geochemically relevant gas mixtures for a laser Raman microprobe, Anal Chem 59 (1987) 2165–2170. https://doi.org/10.1021/ac00144a034.

[11] R. Adami, J. Schuster, S. Liparoti, E. Reverchon, A. Leipertz, A. Braeuer, A Raman spectroscopic method for the determination of high pressure vapour liquid equilibria, Fluid Phase Equilib 360 (2013) 265–273. https://doi.org/10.1016/j.fluid.2013.09.046.

[12] C. Ziparo, A. Giannasi, L. Ulivi, M. Zoppi, Raman spectroscopy study of molecular hydrogen solubility in water at high pressure, Int J Hydrogen Energy 36 (2011) 7951–7955. https://doi.org/10.1016/j.ijhydene.2011.01.178.

[13] L. Li, X. Zhang, Z. Luan, Z. Du, S. Xi, B. Wang, L. Cao, C. Lian, J. Yan, Raman vibrational spectral characteristics and quantitative analysis of H_2 up to 400°C and 40 MPa, Journal of Raman Spectroscopy 49 (2018) 1722–1731. https://doi.org/10.1002/jrs.5420.

[14] A.J. Parrott, P. Dallin, J. Andrews, P.M. Richardson, O. Semenova, M.E. Halse, S.B. Duckett, A. Nordon, Quantitative In Situ Monitoring of Parahydrogen Fraction Using Raman Spectroscopy, Appl Spectrosc (2018) 000370281879864. https://doi.org/10.1177/0003702818798644.

[15] K. Jeong, A. Arami-Niya, X. Yang, G. Xiao, G. Lipinski, Z.M. Aman, E.F. May, M. Richter, P.L. Stanwix, Direct characterization of gas adsorption and phase

transition of a metal organic framework using in-situ Raman spectroscopy, Chemical Engineering Journal 473 (2023) 145240. https://doi.org/10.1016/j.cej.2023.145240.

[16] Y. Ge, L. Li, S. Xi, Y. Zhang, Z. Luan, X. Zhang, Comparison of Raman spectral characteristics and quantitative methods between 13CH4 and 12CH4 from 25 to 400 °C and 50 to 400 bar, Spectrochim Acta A Mol Biomol Spectrosc 304 (2024) 123380. https://doi.org/10.1016/j.saa.2023.123380.

[17] X. Wu, W. Lu, W. Ou, M.-C. Caumon, J. Dubessy, Temperature and salinity effects on the Raman scattering cross section of the water OH-stretching vibration band in NaCl aqueous solutions from 0 to 300 °C, Journal of Raman Spectroscopy 48 (2017) 314–322. https://doi.org/10.1002/jrs.5039.

[18] V. Theodor, G. Inés, T. J.P. Martin, Confinement effects on the physical properties of shale oil and gas, Imperial College London, 2018.

[19] A.H. Harvey, E.W. Lemmon, Correlation for the Vapor Pressure of Heavy Water From the Triple Point to the Critical Point, J Phys Chem Ref Data 31 (2002) 173–181. https://doi.org/10.1063/1.1430231.

[20] J. Gernert, R. Span, EOS–CG: A Helmholtz energy mixture model for humid gases and CCS mixtures, J Chem Thermodyn 93 (2016) 274–293. https://doi.org/10.1016/j.jct.2015.05.015.

[21] O. Kunz, W. Wagner, The GERG-2008 Wide-Range Equation of State for Natural Gases and Other Mixtures: An Expansion of GERG-2004, J Chem Eng Data 57 (2012) 3032–3091. https://doi.org/10.1021/je300655b.

[22] R. Span, W. Wagner, A New Equation of State for Carbon Dioxide Covering the Fluid Region from the Triple-Point Temperature to 1100 K at Pressures up to 800 MPa, J Phys Chem Ref Data 25 (1996) 1509–1596. https://doi.org/10.1063/1.555991.

[23] R. Span, E.W. Lemmon, R.T. Jacobsen, W. Wagner, A. Yokozeki, A Reference Equation of State for the Thermodynamic Properties of Nitrogen for Temperatures from 63.151 to 1000 K and Pressures to 2200 MPa, J Phys Chem Ref Data 29 (2000) 1361–1433. https://doi.org/10.1063/1.1349047.

[24] J.W. Leachman, R.T. Jacobsen, S.G. Penoncello, E.W. Lemmon, Fundamental Equations of State for Parahydrogen, Normal Hydrogen, and Orthohydrogen, J Phys Chem Ref Data 38 (2009) 721–748. https://doi.org/10.1063/1.3160306.

[25] D. V. Petrov, I.I. Matrosov, D.O. Sedinkin, A.R. Zaripov, Raman Spectra of Nitrogen, Carbon Dioxide, and Hydrogen in a Methane Environment, Opt Spectrosc 124 (2018) 8–12. https://doi.org/10.1134/S0030400X18010137.

[26] H.E. Howard-Lock, B.P. Stoicheff, Raman intensity measurements of the Fermi diad ν1, 2ν2 in 12CO2 and 13CO2, J Mol Spectrosc 37 (1971) 321–326. https://doi.org/10.1016/0022-2852(71)90302-X.

[27] L. Li, Z. Du, X. Zhang, S. Xi, B. Wang, Z. Luan, C. Lian, J. Yan, In Situ Raman Spectral Characteristics of Carbon Dioxide in a Deep-Sea Simulator of Extreme Environments Reaching 300 °C and 30 MPa, Appl Spectrosc 72 (2018) 48–59. https://doi.org/10.1177/0003702817722820.

[28] K.M. Rosso, R.J. Bodnar, Microthermometric and Raman spectroscopic detection limits of C02 in fluid inclusions and the Raman spectroscopic characterization of C02, Geochim Cosmochim Acta 59 (1995) 3961–3975. https://doi.org/10.1016/0016-7037(95)94441-H.

[29] Y. Ikushima, K. Hatakeda, N. Saito, M. Arai, An *in situ* Raman spectroscopy study of subcritical and supercritical water: The peculiarity of hydrogen bonding near the critical point, J Chem Phys 108 (1998) 5855–5860. https://doi.org/10.1063/1.475996.

[30] S. Qiang, Z. Hai-Fei, D. Ti-Yu, Effects of Temperature on D_2O Water Structure Investigated by Raman Spectroscopy, Chinese Physics Letters 22 (2005) 661–663. https://doi.org/10.1088/0256-307X/22/3/039.

[31] L. De Marco, W. Carpenter, H. Liu, R. Biswas, J.M. Bowman, A. Tokmakoff, Differences in the Vibrational Dynamics of H_2O and D_2O: Observation of Symmetric and Antisymmetric Stretching Vibrations in Heavy Water, J Phys Chem Lett 7 (2016) 1769–1774. https://doi.org/10.1021/acs.jpclett.6b00668.

[32] Q. Hu, S. Ouyang, J. Li, Z. Cao, Raman spectroscopic investigation on pure D_2O/H_2O from 303 to 573 K: interpretation and implications for water structure, Journal of Raman Spectroscopy 48 (2017) 610–617. https://doi.org/10.1002/jrs.5088.

[33] I. Tsivintzelis, S. Ali, G.M. Kontogeorgis, Modeling Phase Equilibria for Acid Gas Mixtures using the Cubic-Plus-Association Equation of State. 3. Applications Relevant to Liquid or Supercritical CO_2 Transport, J Chem Eng Data 59 (2014) 2955–2972. https://doi.org/10.1021/je500090q.

[34] R. Oparin, T. Tassaing, Y. Danten, M. Besnard, A vibrational spectroscopic study of structure evolution of water dissolved in supercritical carbon dioxide under isobaric heating, J Chem Phys 120 (2004) 10691–10698. https://doi.org/10.1063/1.1739214.

[35] J.R. Scherer, M.K. Go, S. Kint, Raman spectra and structure of water from -10 to 90.deg., J Phys Chem 78 (1974) 1304–1313. https://doi.org/10.1021/j100606a013.

[36] Y. Sanchez-Vicente, J.P.M. Trusler, Measurements and Modelling of Vapour–Liquid Equilibrium for (H2O + N2) and (CO2 + H2O + N2) Systems at Temperatures between 323 and 473 K and Pressures up to 20 MPa, Energies (Basel) 15 (2022) 3936. https://doi.org/10.3390/en15113936.

[37] V.Y. Maslennikova, N.A. Vdovina, D.S. Tsiklis, Solubility of Water in Compressed Nitrogen, Russian Journal of Physical Chemistry 45 (1971).

[38] P. Gillespie, G. Wilson, Vapor-liquid equilibrium data on water-substitute gas components: N/sub 2/-H/sub 2/O, H/sub 2/-H/sub 2/O, CO-H/sub 2/O, H/sub 2/-CO-H/sub 2/O, and H/sub 2/S-H/sub 2/O, 1980. https://doi.org/10.2172/6782591.

6 Conclusions and recommendations for future studies

6.1 Conclusions

The carbon capture, utilisation, and storage (CCUS) value chain has been identified as a key pathway for the abatement of anthropogenic CO_2 emissions. Earlier chapters established that due to the substantial amount of CO_2 emitted from hard-to-abate sectors, large-scale infrastructure deployment in the CCUS value chain is required. This thesis was centered on improving the performance of the CO_2 conditioning process. Therefore, the focus of the thesis was on the optimisation of the CO_2 conditioning process and improving the thermodynamic modelling and the measurement of impurities relevant to the CCUS value chain.

Using the 3D Dunkirk Carbon Capture project as a case study, a systematic and fair optimisation of CO_2 pressurisation routes was conducted. Here, a holistic approach was taken, where the design and evaluation of CO_2 pressurisation routes were considered against the extent of pipeline sharing with other CO_2 point sources. This study compared various permutations of these two pressurisation pathways: (1) conventional multistage compression, and (2) subcritical liquefaction and pumping. These processes were evaluated based on their power requirements, and flexibilities in varying the final pressure of the CO_2-rich stream. It was found that the key opportunities for reducing energy consumption and capital investment requirements in the CO_2 conditioning process and pipeline infrastructure, lay in the optimisation of interstage compression ratios and the acquisition of a low-temperature cooling utility, such as seawater. Specifically, the utilisation of a low-temperature cooling water yields a substantial decrease in total power demand, and the number of optimal compressors. Moreover, it is pivotal in enhancing process flexibility, as pathways require less additional power with rising pressure requirements, in cases where flowrate of the shared pipeline is variable. This thesis thus has highlighted the trade-offs involved in the sizing of pipeline infrastructure, and how the selection and design of CO_2 pressurisation routes could enable pipeline sharing in contexts where there is uncertainty in future transportation demand.

This study further focused on modelling the phase equilibria of a common class of CO_2 impurities – sulphur-containing compounds (SO_2, H_2S, COS). This work identified potential association schemes for these compounds within the CPA framework. This approach was validated with phase equilibria data of mixtures containing these

sulphur-containing compounds and self-associating or non-associating compounds. It was found that the allocation of association sites for SO_2 and H_2S enhanced the predictive capabilities of CPA when modelling phase equilibria of mixtures with these compounds. However, COS was an exception to this, as it required a binary interaction parameter fitted from the phase equilibria data to improve the performance of the model. Overall, this work has provided an approach for the accurate modelling of the phase equilibria of systems containing sulphur-containing compounds, especially since limited experimental data is available.

Furthermore, this study investigated the use of in-situ Raman spectroscopy to determine the water content of compressed fluids – CO_2, N_2, and H_2. For this purpose, a Raman experimental apparatus was developed to enable the equilibrium measurements at pressures ranging from 5 to 15 MPa. The study found that while the widely used ratio method could be employed to determine the water content of the H_2-water system, it has limited applicability for the CO_2-water and N_2-water systems. This is largely due to significant changes in the apparent relative scattering cross-section which have been demonstrated to vary with temperature and pressure. Additionally, it was found in this study, that the position of the water symmetric stretch Raman feature is not just sensitive to temperature, as other studies have concluded, but also varies with the water content of a binary mixture's vapour phase. From this, this work has proposed a framework for the determination of gas water content based solely on this water-only Raman feature, which was validated and demonstrated to be successful across the investigated systems. The advancement of this work provides the foundation for the development of on-line Raman sensors, which could be employed for the real-time monitoring of dehydration processes and the measurement of the water content of CO_2-rich streams in pipelines.

6.2 Key contributions

The key contributions of this work are therefore:

- Providing a new perspective for the design of CO_2 conditioning process schemes, by emphasising the consideration of energy minimisation and process flexibility for pipeline sharing.
- Providing a framework for the predictive modelling of the phase equilibria of mixtures with sulphur-containing compounds.
- Developing the appropriate CPA parameters for the accurate modelling of the phase equilibria of mixtures with sulphur-containing compounds.

- Demonstrating that water at low mole fractions could be detected across various compressed gases using in-situ Raman spectroscopy.
- Demonstrating the limitations of the widely employed Raman spectroscopy ratio method in evaluating gas water content from Raman spectra.
- Developing a novel quantitative approach for determining the water content of compressed fluids using water-only Raman features.

Combined this study provides the framework for the design of flexible CO_2 conditioning processes, an approach for the modelling of common impurities and their measurement.

6.3 Recommendations for future studies

Process modelling and optimisation

- Stress test the conditioning process against other uncertainties in the CCUS value chain, such as variability in impurity compositions for the captured CO_2 stream, and impact of policy choices, such as carbon pricing mechanisms.
- Determine the CAPEX and OPEX implications of designing flexible conditioning facilities.

Modelling the phase equilibria of mixtures with impurities relevant to CCUS

- Evaluate the extent to which the various association schemes of the sulphur-containing compounds influence the prediction of thermophysical properties. Thermophysical properties of interest in the CCUS value chain are isobaric heat capacity, speed of sound, density, and viscosity of mixtures containing CO_2.
- Filling the gap of experimental data to describe the phase equilibria of mixtures with sulphur-containing compounds (SO_2, H_2S, COS). This is especially necessary for multi-component systems with compositions similar to those of captured CO_2-rich streams.
- Integrating the CPA model and the appropriate parameters to ASPEN HYSYS or other process simulation software, to model the conditioning processes of streams with sulphur-containing compounds.

Raman spectroscopy experiments

- Validate the proposed water content methodology at wide temperature and pressure conditions. This exploration can entail first determining the Raman

features of pure water at various temperature and pressure conditions, and then conducting similar binary experiments at those conditions. This will assess the limitations of the proposed water content determination approach.

- Validate the application of the proposed water content measurements approach to multicomponent systems such as CO_2+H_2+D_2O, CO_2+N_2+D_2O, and N_2+H_2+D_2O.
- Investigate whether, for the liquid phase of the CO_2+D_2O, the peak positions of the CO_2 fermi diad components can be employed to predict CO_2 content. The current work has already demonstrated that the fermi diad components of CO_2 can be employed successfully as a proxy for phase density in CO_2-rich streams.
- Connect the Raman spectroscopy apparatus to a gas chromatographer. The current Raman spectroscopy apparatus was designed for static equilibrium experiments. A similar setup can be developed to enable sampling of the gas and the liquid phase. Analysis of these phases through gas chromatography will reduce the reliance on thermodynamic models when calibrating the Raman spectroscopy apparatus.
- Improve the prediction of vapour phase density considering the evolution of the bulk gases' Raman features.
- Improve the sensitivity of the spectrometer. The current Raman spectroscopy apparatus had an upper detection limit of 3,000 cm^{-1}, which is below the wavenumber where the symmetric H_2O O-H stretch could be observed. Extending this limit could be done in one of two ways: (1) by changing the incident wavelength of the laser; (2) Extending the sensitivity of the spectrometer's CCD to detect a wider range of wavelengths.

Appendices

Appendix A – in-situ Raman spectroscopy setup: thermosetting cell window

This section outlines the procedure employed for the thermosetting of the Raman setup cell's sapphire window to the cell's metal frame.

The sapphire window was thermoset onto the metal frame using a polyimide film (Du Pont Kapton, FN Model 200FN919). This polyimide film has an FEP layer on either side which melts and ensures that the sapphire window is fixed to the metal frame. This film was cut to an annular ring, with an outer diameter of 19.9 mm, and an inner diameter of 16.1 mm, and it was placed on the shoulder of the metal frame, as shown in Figure 15 (a).

The sapphire window was then placed on the shoulder of the metal frame. It was then transferred to a clamping device. To ensure effective contact between the clamp and the window, an aluminium coin (d_o=15 mm) was placed between the two, as illustrated in Figure 15 (b). Without the aluminium coin, the thermosetting of the polyimide film was unsuccessful.

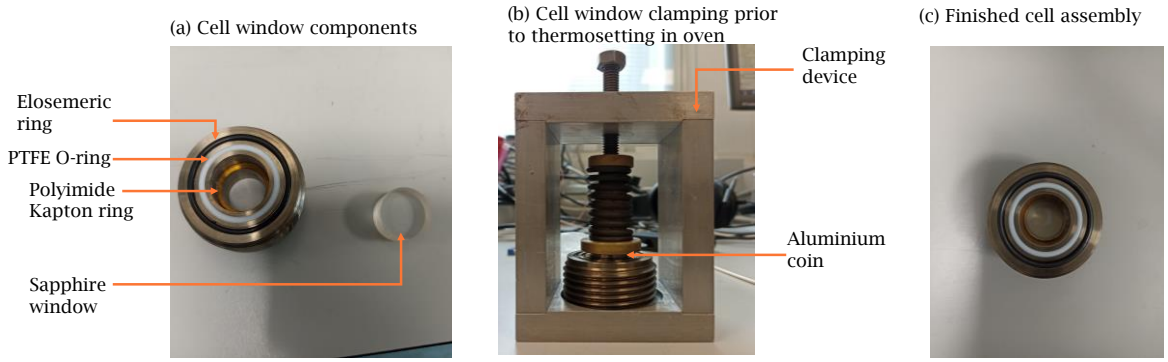

Figure 15: Assembly of the cell window.

The thermal setting procedure was as follows:

1. The vacuum oven was heated to 373.15 K.
2. The clamped window, shown in Figure 15 (b), was then placed in the oven.
3. Evacuate the oven, and increase the temperature to 653.15 K, and remain at this temperature for 190 mins. The thermosetting occurs at this temperature, under a vacuum.

4. Following this, the temperature is reduced to 313.15 K to allow the oven to cool down. The clamped structure is then removed, with the vacuum of the oven being relieved.

The finished assembly is shown in Figure 15 (c). To validate the success of the thermosetting process, the cell is pressure tested. It is evaluated as to whether the cell can hold a vacuum for 1 hour. Next, Helium is introduced to the cell at 160 bar, to establish whether it can maintain the pressure, while a Helium leak detector is used to check for leaks in the cell.

Appendix B – in-situ Raman spectroscopy setup: Determining the distance between the telescope and cell window

The introduction of the sapphire window and the bulk gas in the cell leads to refraction of the incident light, culminating in a shift in the Raman setup's laser focal distance. To ensure maximum interaction of the laser with the contents of the cell, it is desired that the focal point is located at the centre of the cell.

The objective of this appendix is to demonstrate how the suitable distance between the Raman spectroscopy lens and the cell's window was determined, as shown in Figure 16. The laser source telescope has a focal length of 65 mm, measured in air. The dotted object in the cell is the hypothetical focal point, consistent with the focal length measured in air. The red object is the real focal point, as a result of refraction from the cell window and the bulk gas.

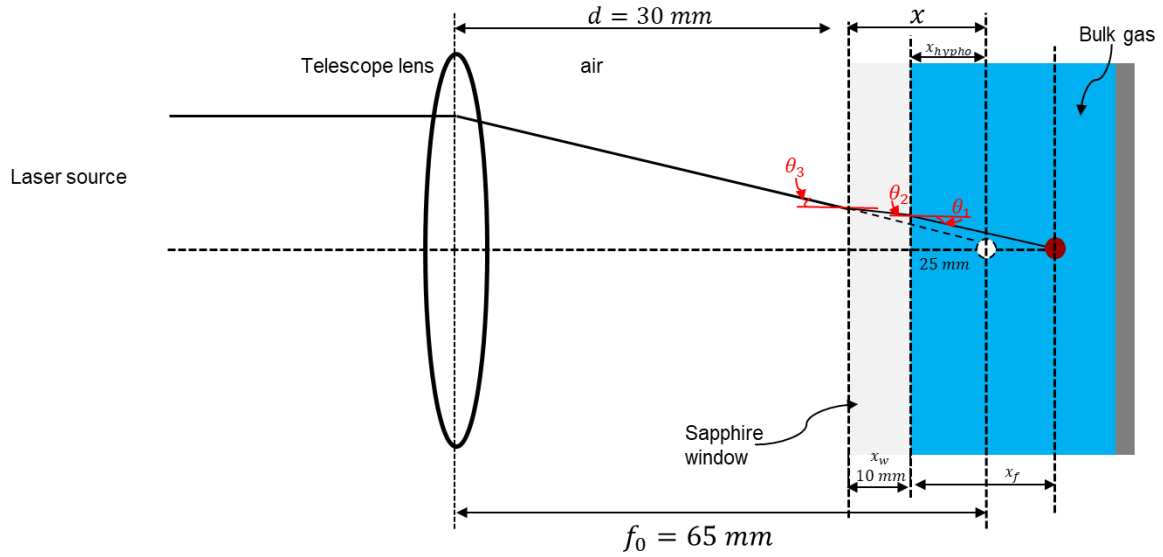

Figure 16: Geometric description of the Raman spectroscopy setup.

The approach from Pan and Trusler [1] can be modified, such that the working equations from Figure 16 are the following:

From Snell's law, the angles of incidence and refraction can be simplified to:

$$n_w sin\theta_2 = n_a sin\theta_3 \quad (8)$$

$$n_w sin\theta_2 = n_g \sin\theta_1 \quad (9)$$

In equations 8and 9, n_w is the refractive index of the sapphire window, and it has the value of 1.75. n_g is the refractive index of the gas phase in the cell. This is estimated from Lorentz-Lorenz equation, as follows:

$$\frac{n_g^2 - 1}{n_g^2 + 2} = \frac{4\pi N_A \alpha}{3V_m} \quad 10$$

From equation 10, N_A, α, V_m, are respectively, Avogadro's constant, molecular polarizability, and the molar volume. It should be noted that the molar volume is a function of both temperature and pressure, and was determined from relevant equations of state, as discussed in the main section. By determining n_g at the experimental temperature and pressure conditions, the angles of refraction, θ_1 and θ_2, can be determined from equations8 and 9, assuming a low angle of incidence, θ_3.

From Figure 16, geometrically, the vertical distance between the point where the incident ray intersects the window and its intersection with optical. axis, the following can be shown to be:

$$xtan\theta_3 = x_w tan\theta_2 + x_f tan\theta_1 \quad 11$$

Therefore, the distance from the inner edge of the sapphire window and the real focal point, x_f can be determined. Figure 17 presents x_f for all the bulk gas at the experimental pressure and temperature conditions for a distance $d = 40\,mm$. Figure 17 illustrates that at this fixed distance, the focal point of the laser remains within 3mm of the centre of the cell. This is reasonable as the total length of the cell is 39.30 mm.

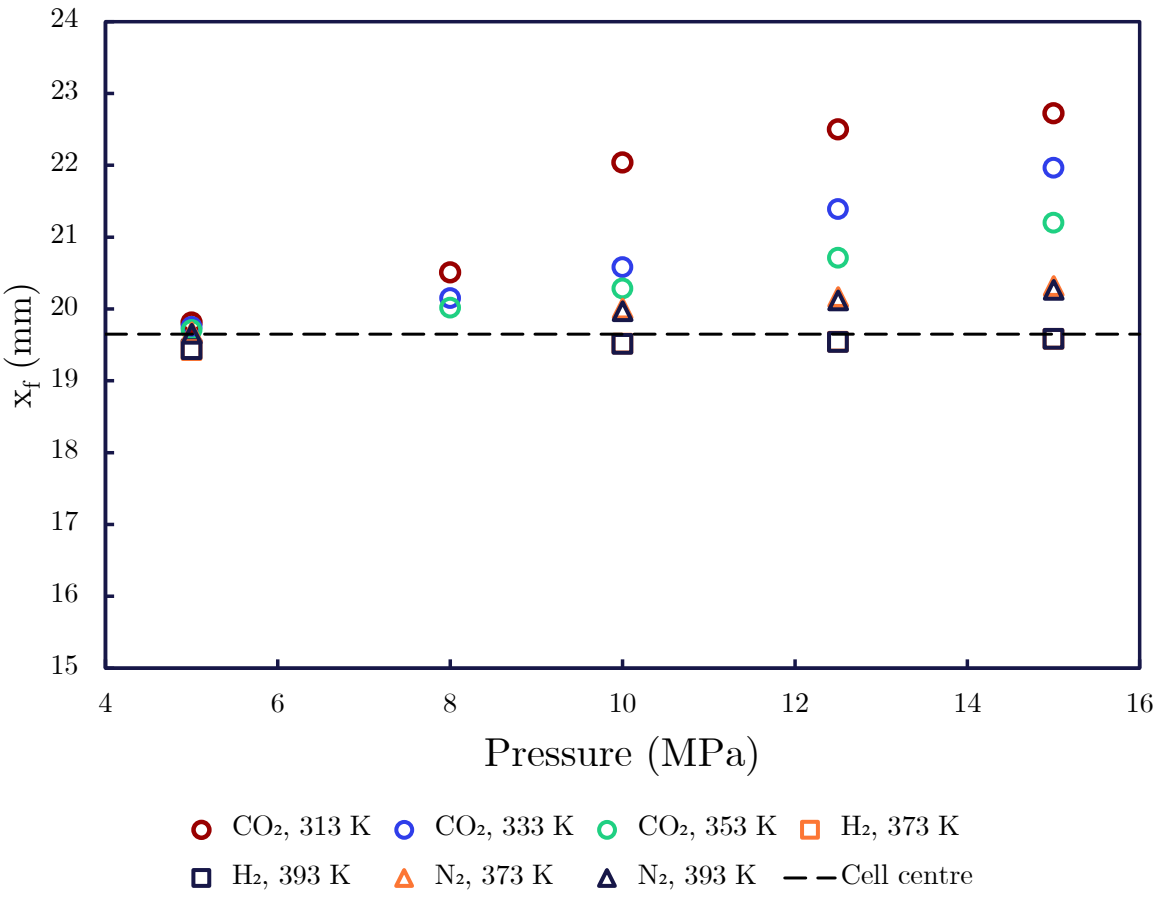

Figure 17: Resulting focal distance from the different experimental conditions. The distance is presented relative to the inside edge of the cell's sapphire window.

References

[1] Z. Pan, J.P.M. Trusler, Refractive Index Effects in Pendant Drop Tensiometry, Int J Thermophys 43 (2022) 65. https://doi.org/10.1007/s10765-022-02997-z.

[2] Y. Ikushima, K. Hatakeda, N. Saito, M. Arai, An *in situ* Raman spectroscopy study of subcritical and supercritical water: The peculiarity of hydrogen bonding near the critical point, J Chem Phys 108 (1998) 5855–5860. https://doi.org/10.1063/1.475996.

[3] S. Qiang, Z. Hai-Fei, D. Ti-Yu, Effects of Temperature on D_2O Water Structure Investigated by Raman Spectroscopy, Chinese Physics Letters 22 (2005) 661–663. https://doi.org/10.1088/0256-307X/22/3/039.

[4] L. De Marco, W. Carpenter, H. Liu, R. Biswas, J.M. Bowman, A. Tokmakoff, Differences in the Vibrational Dynamics of H_2O and D_2O: Observation of Symmetric and Antisymmetric Stretching Vibrations in Heavy Water, J Phys Chem Lett 7 (2016) 1769–1774. https://doi.org/10.1021/acs.jpclett.6b00668.

[5] Q. Hu, S. Ouyang, J. Li, Z. Cao, Raman spectroscopic investigation on pure D_2O/H_2O from 303 to 573 K: interpretation and implications for water structure, Journal of Raman Spectroscopy 48 (2017) 610–617. https://doi.org/10.1002/jrs.5088.